Politecnico di Milano
DAER - Dipartimento di Scienze e Tecnologie Aerospaziali

Development of an effective reusable crash absorber based on an improved Negative Stiffness Honeycomb approach

Final Thesis - M.Sc. in Aeronautical Engineering

Supervisor:
Prof. Marco Anghileri

Co-Supervisor:
Dott. Ivan Colamartino

Author:
Alessandro Giustina
968227

Academic Year 2021–2022

Abstract

Crash absorbers are structural devices used in automotive with the aim of reducing the severity of impacts. Conventional crash absorbers dissipate the kinetic energy of the collision by irreversible deformation, and need to be replaced afterwards to restore safety of the structure, highly increasing cost and inconvenience of the system. The aim of this experimental thesis was to design and manufacture a reusable crash absorber , able to regain functionality after compression. The work was based on the concept of Negative Stiffness Honeycomb, with the objective of improving the performance, reliability and cost effectiveness with respect to previously published studies in the literature based on a similar concept. The multi-step experimental process led to the realization of three different prototypes, in series as a result of critical evaluation of their performance. The first and second iteration model were made in Nylon PA 6/66 3D printed by FDM, while the last one was laser cut by Stainless Steel AISI 304. The first iteration model was characterized by a simple bidimensional configuration, while the second and third iteration models featured a novel three-dimensional modular design , through which an increased stability in dynamic compressions as well as less complex manufacturing and assemble process were obtained The second and third models were tested under dynamic compression, reaching performance results higher in terms of absolute value of peak force and energy dissipation with respect to previous literature studies. If confirmed in further larger studies, this thesis work could represent a relevant advancement in the field of crashworthiness. In fact, negative stiffness honeycomb could become a viable alternative in those contexts where conventional crash absorbers are not convenient for practical applications involving repeated impacts or when substitution of the device is made complex by environmental and economic factors, with the final result of reducing cost, time and work associated to the replacement of the deformed safety device after the collision.

Contents

List of Figures

List of Tables

List of Symbols

c	Speed of propagation of sound wave across a medium, [mm/s]
Δ	downward vertical displacement of the middle point of the curved beams normalized on the initial apex height, [-]
d	downward vertical displacement of the middle point of the cured beams, [mm]
E	Young modulus of the material, [J]
E_{in}	Initial Total Energy of the system before the impact, [J]
E_{fin}	Total Energy of the System after the impact, [J]
E_{kin_0}	Kinetic Energy of the colliding body before the impact, [J]
E_{kin_1}	Kinetic energy transmitted during the impact, [J]
E_{therm}	Thermal energy dissipated during the impact, [J]
$E_{elastic}$	Energy associated to the elastic response of the material to a crash event, [J]
$E_{plastic}$	Energy associated to the plastic response of the material to a crash event, [J]
$E_{potential}$	Energy dissipated during an impact as potential energy, [J]
$\boldsymbol{\epsilon}$	vector of components of deformation tensor
f	Transversal Force, [N]
F	Transversal force normalized on moment of inertia, [-]
h	apex height of pre-shaped curved beams, [mm]
h_h	second base dimension of hexagonal honeycomb cell, [mm]
I_{yy}	Moment of inertia oriented in transversal direction during bending deformation, [mm^4]
λ	wavelength of hexagonal honeycomb folds during out-of-plane compression [mm],from fig. 1.6
L	Horizontal length of the beams in Negative stiffness honeycomb cells [mm]
l_h	length of hexagonal honeycomb cells [mm], ref fig. 1.6
ν	Poission's ratio of the material, [-]
N	Normalized axial load, [-]
N_j	Normalized critical axial load for j-th buckling load, [-]
p	Axial Load, [N]
Q	Bistability ratio, [-]
ρ	Density of the material, [$\frac{ton}{mm^3}$]
s	change of length of the beams during deformation, [mm]
s	Generalized displacements vector

σ_{pl_h}	critical stress for the collapse of hexagonal honeycomb cells, [Mpa]
σ_y	Yield stress of the material, [Mpa]
$\mathbf{s}^t$	Vector of generlized displacement at time t
t	thickness of the beams in Negative Stiffness honeycombs, [mm]
t_h	thickness of hexagonal honeycomb face sheets, [mm], ref. fig. 1.6
Δt	timestep of the numerical simulation, [s]
$u_{/x,/y,/z}$	displacement in x-direction derived with respect to x,y,z coordinate
$v_{/x,/y,/z}$	displacement in y-direction derived with respect to x,y,z coordinate
w_0	Initial shape of the curved beam in first buckling mode in negative stiffness honeycomb cells, [mm]
w	vertical displacement of generic point of the beam, [mm]
$w_{/x,/y,/z}$	displacement in z-direction derived with respect to x,y,z coordinate
x	Longitudinal coordinate of a generic point along the beam, [mm]
Δx	Characteristic size of the mesh, [mm]
$\mathbf{x}^t$	Vector of generalized geometric position in space at time t
$\dot{\boldsymbol{x}}$	Time derivative of vector x

Chapter 1

Introduction

1.1 The concept of energy absorption

According to the WHO (World Health Organization) every year 1.3 million people die as a result of road traffic crashes [1]. Moreover, the majority of these fatal crashes (93%) happens in low and middle-income countries, even though a much lower percentage of road vehicles (60%) is registered in these states.

For these reasons, there has been an arising interest in the engineering world in designing cars and roadside structures to reduce the severity of the crashes and improve the chance of survival, and also in reducing the cost of the safety and testing equipment in lower socioeconomic background countries. The United Nations General Assembly has set an ambitious target of halving the global number of deaths and injuries from road traffic crashes by 2030 [1].

Crashworthiness, defined as the ability of a structure to protect its occupants during a crash, is evaluated using several criteria. In particular, one critical role of passive safety is reducing the deceleration of the human body during impact.

The first scientific activities to discover the effects of severe deceleration on human bodies were carried out after World War II by John Paul Stapp, an American U.S. Air Force Colonel. The tests were conducted on a horizontal sledge with voluntary soldiers. By June 8, 1951, a total of 74 human runs had been made on the decelerator, 19 with the subjects in the backward position, and 55 in the forward position; many of the experiments were regarding Stapp himself, who proved to walk out from 46.2 g deceleration without damages [2].

Thanks to the data collected by Stapp, the first critical values of deceleration were set by drawing the so called Eiband curves [3], reported in fig.1.1, which show that individuals voluntarily tolerate vertical accelerations up to approximately 18 G without injury, and spinal injury does not occur below longitudinal accelerations of approximately 20-25 G [4]. The current criteria regarding the measure of severity of the accelerations during a crash (ASI, Acceleration Severity Index) are still measured with those critical values.

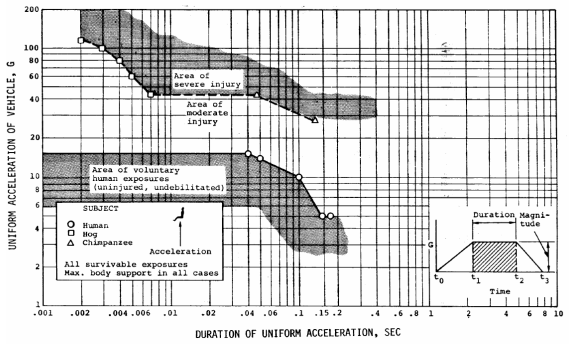

(a) Eiband curves for vertical accelerations

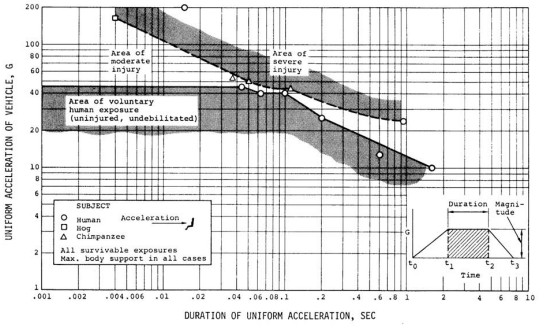

(b) Eiband curves for horizontal decelerations

Figure 1.1: Eiband curves, with limits of survivability [3]

Crash absorbers are structural devices with the aim of reducing the severity of an impact. Through the partial storage of the initial kinetic energy of the moving colliding body, they decease the deceleration that an object or a body experiences during a crash. An example of acceleration injury are the rupture of the aorta in a high sink rate crash or contracoup brain injuries [4]. By storing and redirecting the energy of the impact energy absorbers also reduce the possibility of injury by impact with internal components of the vehicle, which is the other main fatality cause in vehicle impacts.

Moreover, energy absorbers are a valuable item in crash test laboratories, facilities where impact protection devices, occupant harnesses and vehicles are tested for ensuring their crashworthiness. In particular, energy absorbers, in this environment have the role of providing a safe and efficient stop to crash test subject vehicles and horizontal sleds, producing a reliable deceleration profile to evaluate the safety of the passenger, embodied by dummies equipped with acceleration and force sensors.

From a physical perspective, the impact scenario can be analyzed through an energy balance. For the First Law of Thermodynamics the total initial energy before the impact, which consists generally in the kinetic energy of the impacting body, would remain constant and be transmitted to the components involved in the crash and converted into different types of energy, summarized in eq.(1.1).

$$\begin{gathered} E_{in} = E_{fin} \\ E_{kin_0} = E_{Kin_1} + E_{therm} + E_{elastic} + E_{plastic} + E_{potential} + ... \end{gathered} \tag{1.1}$$

Typical absorbers use plastic deformation to dissipate energy during crash. This method has the advantage of being very effective and safe, however it causes irreversible damage to the device, that cannot absorb any more impact safely until its complete substitution.

The aim of this thesis is to explore a novel type of energy absorber able to recover the original configuration after impact with the principle of *Negative Stiffness Honeycomb*.

However, these type of energy absorbers are not likely to completely overcome the conventional technology based on plastic deformation, due to their lower efficiency.

This study lays the foundation for the use of a two-stage device, in which a typical energy absorber is assisted by a negative stiffness structure. The first one will absorb and dissipate most of the energy, however the second stage will be able to recover its deformation restoring partial safety of the structure until the replacement of the plastic stage. This novel feature will allow to substantially reduce the downtime of the vehicles or safety barriers involved in crashes.

1.2 Conventional techniques for energy absorption

There exist many types of energy harvesting devices on the market, mainly depending on the following factors:

- Energy Absorption performance
- Working Environment
- Size

The focus of this thesis research is on the context of absorbers of simple and inexpensive production, constitued by elementary units, with the possibility of scaling up in dimensions and numbers to be used in a wide range of application, from facilities to vehicles and roadside devices.

1.2.1 Tubes

The most common type of absorbers consists of linear tubes of different shapes and materials loaded on the axial direction, due to their easy manufacturability and predictability. Despite the simple design, this type of absorbers allows to dissipate a large amount of force thanks to their high stiffness in the desired direction.

The failure mechanism depends on the nature of the material.

Metal tubes collapse by progressive plastic buckling that results in the formation of three-dimensional folds along the length of the tube, usually concentrated at one of the two extremities. This results in an oscillatory pattern of the Force-displacement curve over a mean value, after the first linear elastic portion.

The length of the tube affected by plastic wrinkling is a qualitative measure of the efficiency of the tube, the most efficient use of the material occurs when as much as possible of tube length is crushed [5].

This type of absorbers was among the first one designed and studied for energy absorption purposes, with extensive literature by *Abramowicz* [6] and *Pugsley* [7].

In contrast, a composite tube experiences brittle fracture due to the limited range of allowable deformation of the material. Composite materials allow to decrease the weight with respect to metallic tubes due to their much lower relative density.

Moreover, the failure mechanism of the composite material create a relatively flat response in the Force-Displacement graph of the absorber under compression loading. This type of response increase the efficiency of the energy absorption mechanism measured as the ratio of the energy absorbed over the mean energy absorbed by the structure.

The differences in deformation modes and force response are evident in fig. 1.2 and 1.3 [8].

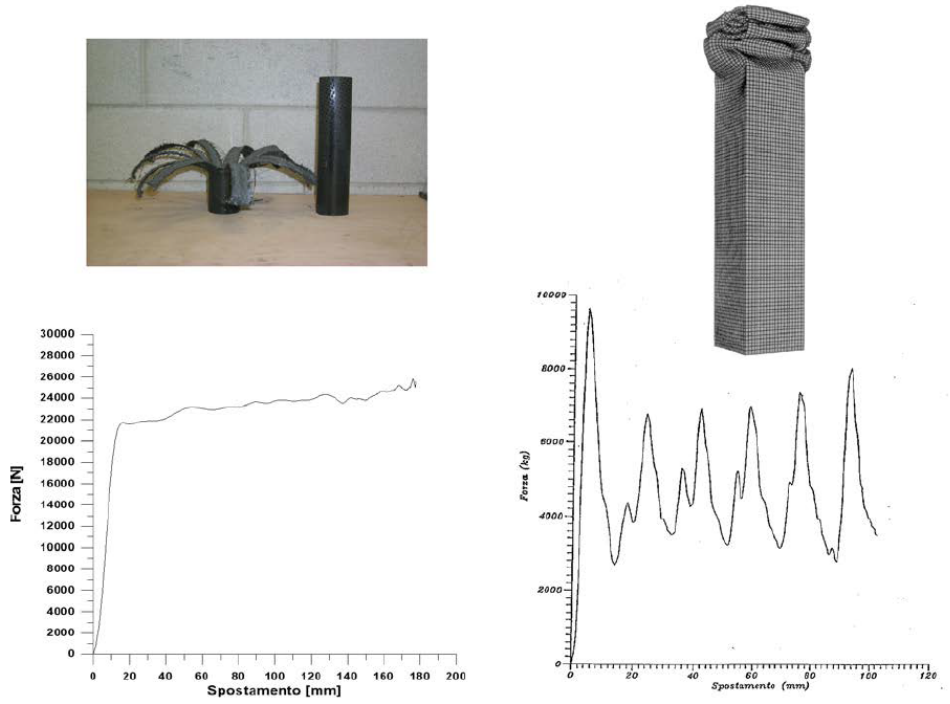

Figure 1.2: Comparison between crushing of composite tubes (on the left) and metal tubes (on the right) [8]

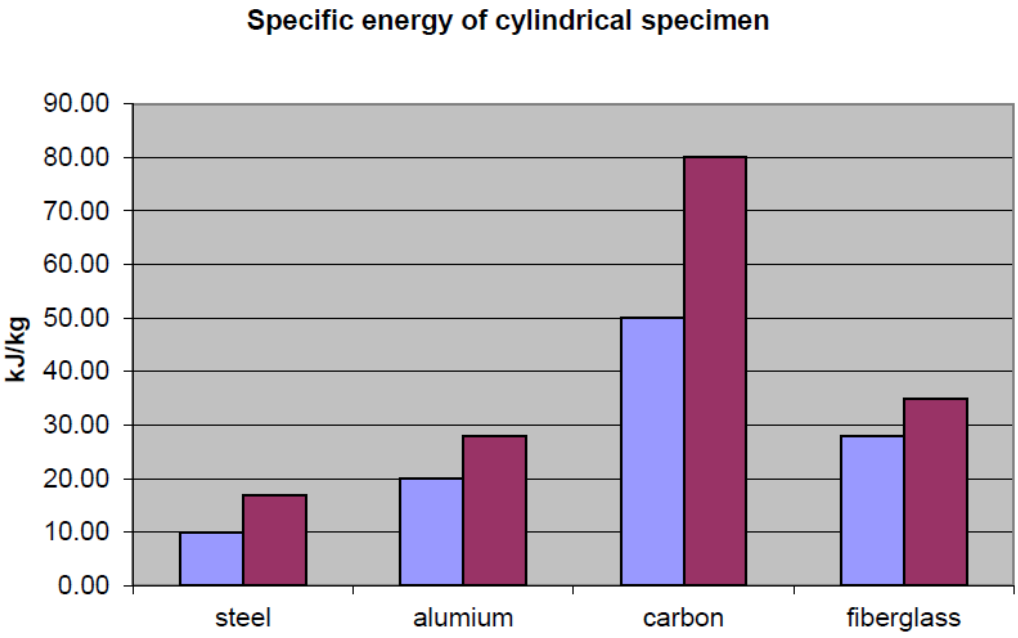

Figure 1.3: Specific energy of tubes of different materials [8]

1.2.2 Honeycombs

Honeycomb structures are metamaterials with a periodic arrangement of unit cell of different shapes [9]. They are often used as a core in composite sandwich panels, as well as stand-alone crash-absorbing structures, particularly efficient for their lightness and hollowness.

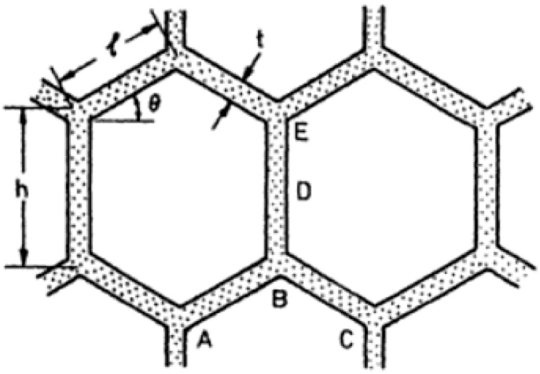

Figure 1.4: Hexagonal shape honeycomb characteristic dimensions, [10]

The behaviour of these types of structures depends on the material composition and loading condition. It's possible to separate the force-displacement response of a typical honeycomb structure shown in fig. 1.5 in three different regions.

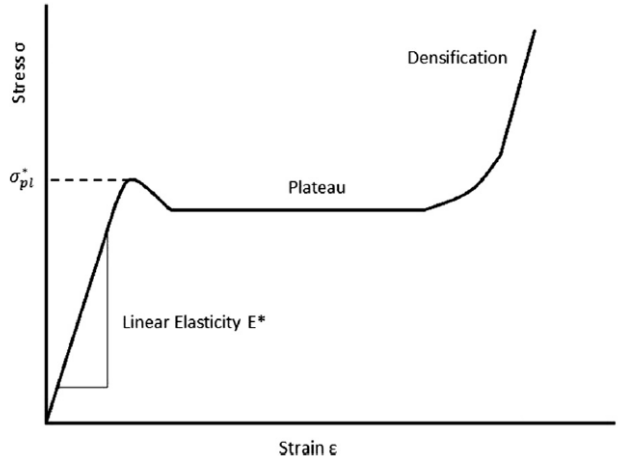

Figure 1.5: Conventional Honeycomb Force-Displacement response [11][10] [12]

Any type of these structure exhibit a linear elastic region of bending and compression of the walls of the cells; beyond a critical strain level, if the material is characterized by a plastic yield point, the cell walls collapse via plastic buckling. The region of plastic deformation is the most effective for absorbing energy because it creates a relatively flat, extended region of plateau stress in the stress-strain graph of the response [11]. After the collapse of each cell, the material experiences a high peak of force called densification.

Wierzbicki [13] modeled the axial collapse of honeycombs loaded with out-of-plane compression by plastic buckling, considering that the cells fold progressively in a periodic shape with a wavelength λ (roughly equal to the cell size length l [10]) showed in fig. 1.6 and predicted the critical stress for the collapse as following in (1.2) with a quadratic relationship with respect to the relative density of cells ($\rho^* = \frac{2}{\sqrt{3}}\frac{t_h}{l_h}$ [10]) :

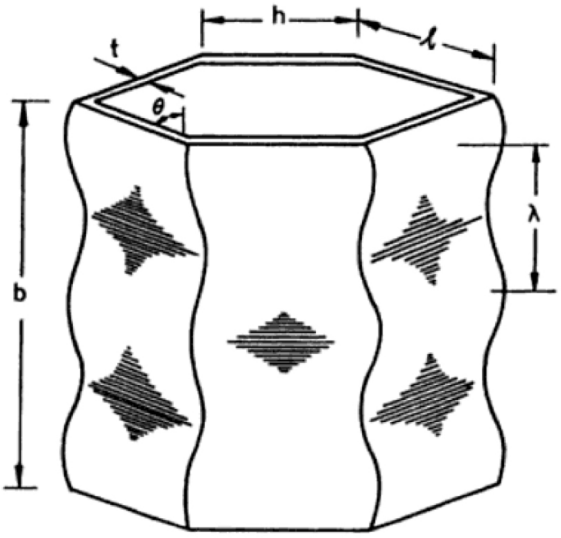

(a) Axial buckling deformation of a hexagonal cell

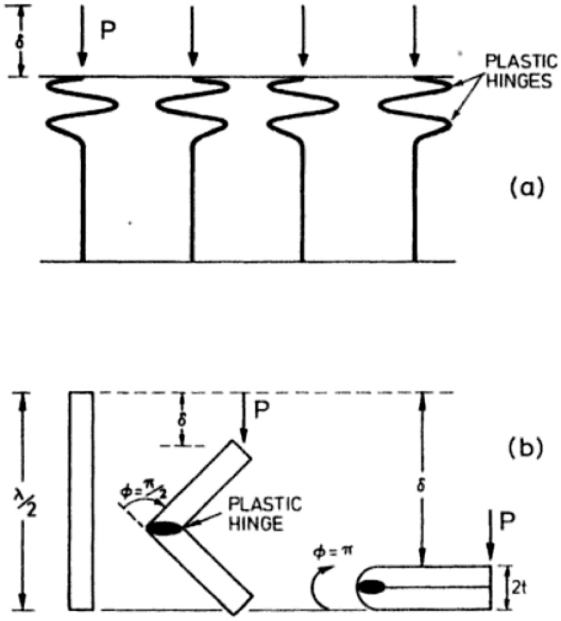

(b) Schematic of the plastic buckling of a honeycomb folding periodically

Figure 1.6: Hexagonal Honeycomb out-of-plane deformation scheme [13]

$$\frac{\sigma_{pl_h}}{\sigma_y} = 6.6 \left(\frac{t_h}{l_h}\right)^{\frac{5}{3}} \tag{1.2}$$

The most common use of honeycomb structure usually exploit its out-of-plane properties, in fact in this direction both the compression module and the plastic collapse strength are much higher [10], however it is useful to consider also the in-plane deformation, because of the similarities with the behaviour of Negative Stiffness Honeycombs.

Papka et al.[14] have investigated the response of metal honeycomb under in-plane compression, with results shown in fig. 1.7.

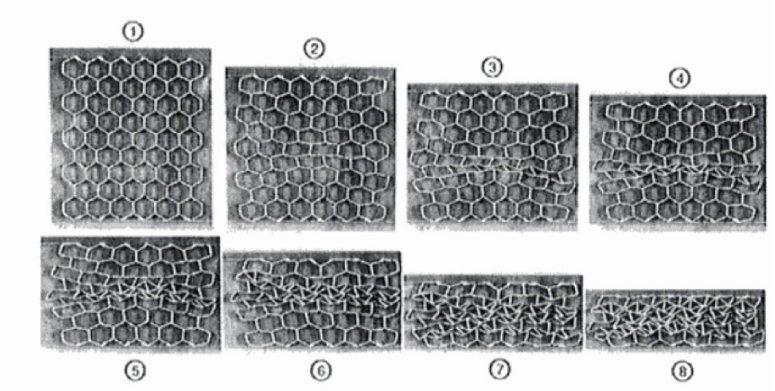

Figure 1.7: Hexagonal honeycomb deformation under in-plane compressive loading [14]

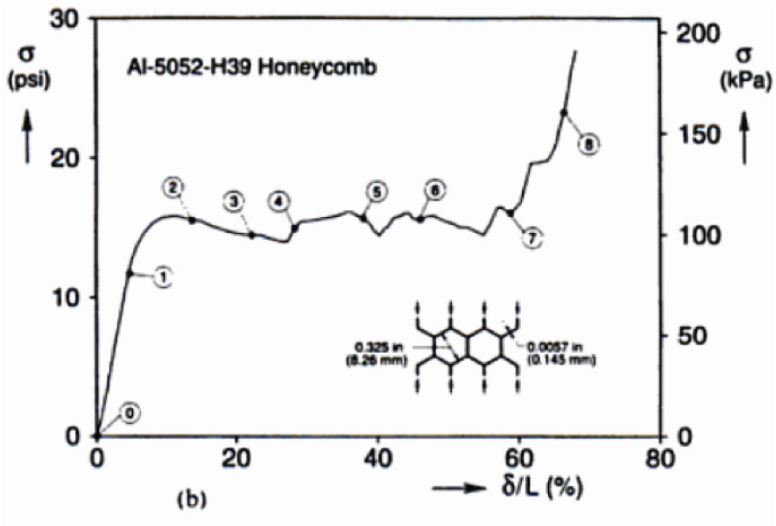

Figure 1.8: Honeycomb response on Force-Displacement graph corresponding to 1.7 [14]

During the deformation corresponding to the plastic plateau in fig. 1.8, if the material is characterized by a plastic yield point, the cell walls collapse via plastic buckling with the formation of plastic hinges at the section of maximum bending moment[10], which are underlined in fig. 1.9.

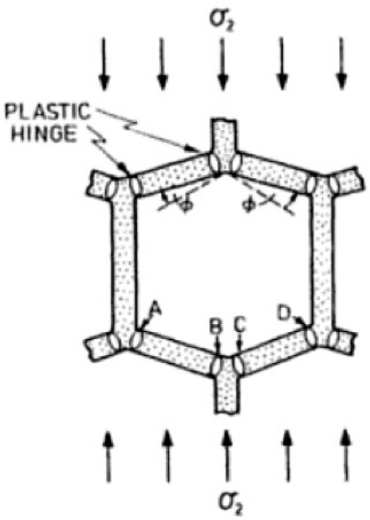

Figure 1.9: Points of nucleation of plastic hinges in hexagonal honeycomb cells [10]

The critical stress for plastic bending has been analytically computed to be equal to (1.3)[10], using reference dimensions of 1.4:

$$\frac{\sigma_{pl_h}}{\sigma_y} = \left(\frac{t_h}{l_h}\right)^2 \frac{1}{2(\frac{h_h}{l_h} + sin\theta_h)sin\theta_h} \tag{1.3}$$

In particular, for the case of regular hexagonal honeycombs $l_h = h_h$ and $\theta_h = 30°$, leading to formula (1.4):

$$\frac{\sigma_{pl_h}}{\sigma_y} = \frac{2}{3}\left(\frac{t_h}{l_h}\right)^2 \tag{1.4}$$

1.2.3 Advantages

On one hand, energy absorbers exploiting conventional methods are considered reliable and safe.

The behaviour of conventional energy absorber summarized in this chapter has been deeply analyzed in literature and the production method is very simple and consolidated

Moreover, the plastic failure mechanism dissipate efficiently the kinetic energy of the impacting object without potential harming to the environment.

1.2.4 Limitations

The main drawback of conventional crash absorbers is the capability to use them only for one impact. The deformation occurred during the impact is irreversible and the object, if subjected to an other impact is not able to perform anymore as it should. The kinetic energy cannot be anymore converted into plastic and , as a result, the acceleration and severity of the impact increase drastically. After the collision these types of absorbers need to be substantially serviced, with the substitution of some key components and, in some cases, of the entire device, with a considerable loss in terms of downtime and refurbishment costs, which could become similar to the initial installation cost.

For this reason, crash absorbers based on plastic deformation, are not suitable for applications involving repeated impacts or when the intervention to replace the device is made very difficult from environmental factors.

1.3 Novel energy absorption techniques

In order to avoid the necessity of replacing absorbers after impacts, in the last years interest towards reusable devices has grown exponentially. For the preparation of this thesis work, with the goal of researching a reusable energy absorber, three design were initially proposed.

1. *Shape memory polymers and alloys* are a class of materials able to recover high levels of deformation through heating and cooling cycles, which allow to change reversibly between two crystalline states. This phase transformation is accompanied by an hysteresis cycle, which is desirable for a crash absorbing device, since it is able to dissipate the initial kinetic energy of the colliding body. *Bodaghi et al.* [15] investigated the use of these materials in a bidimensional auxetic 3d printed prototype. A summary of their work is reported in fig. 1.10

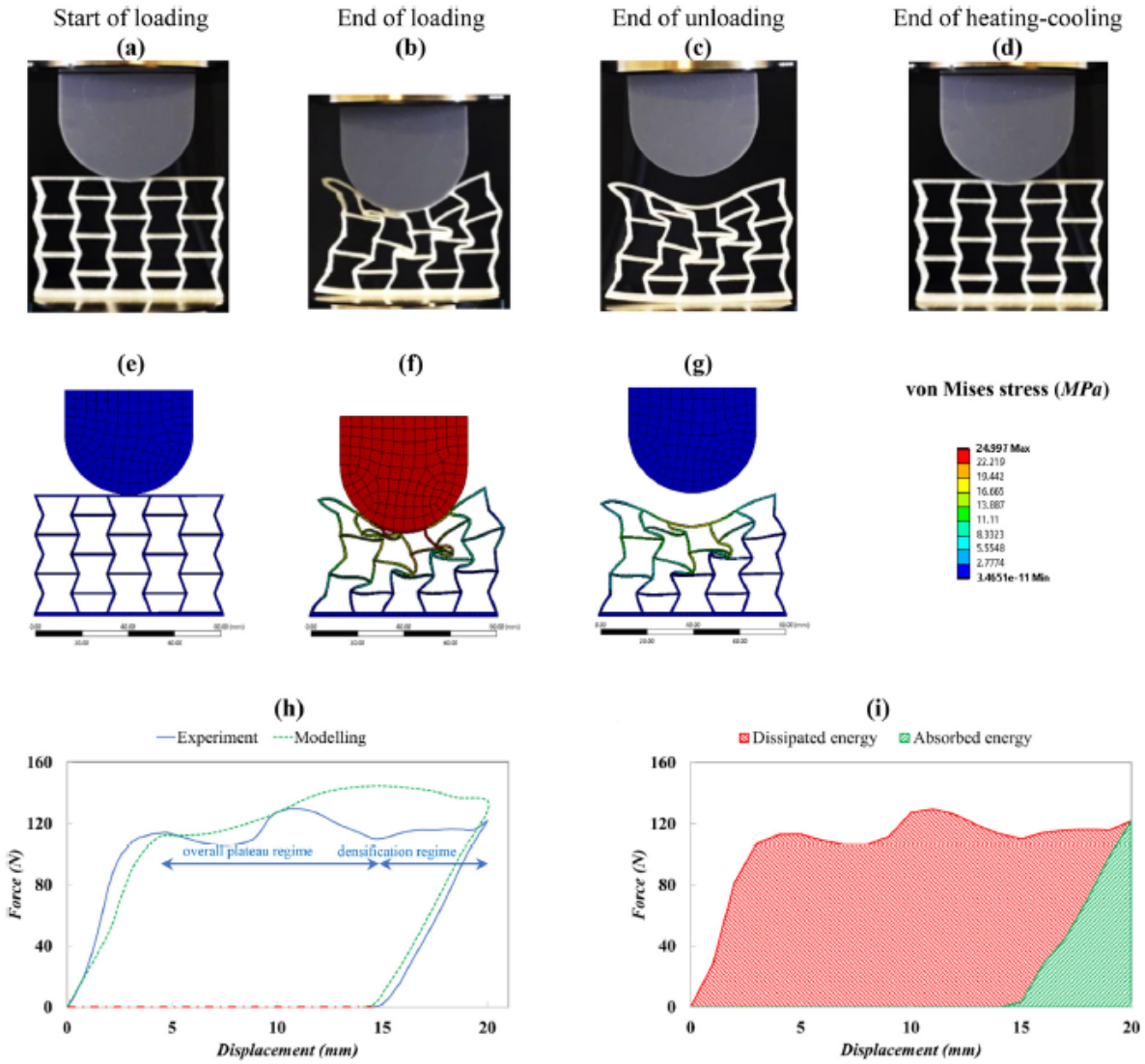

Figure 1.10: Shape Memory Polymers, Experimental compression test (a-d) and Numerical Computation (e-g) conducted by *Bodaghi et al.*, Force-Displacement graph (h) and dissipated energy (i) [15]

2. An axially loaded, slender beam with weakening boundary conditions was researched by *Heo et al.* [16] from Buffalo University. As can be seen in fig.1.11, during the loading, the constraints of the beam snap abruptly, at a precise deformation level, from clamped-clamped to pin-pin, allowing to absorb the energy of the compression, by exhibiting a different path in the loading and unloading curves.

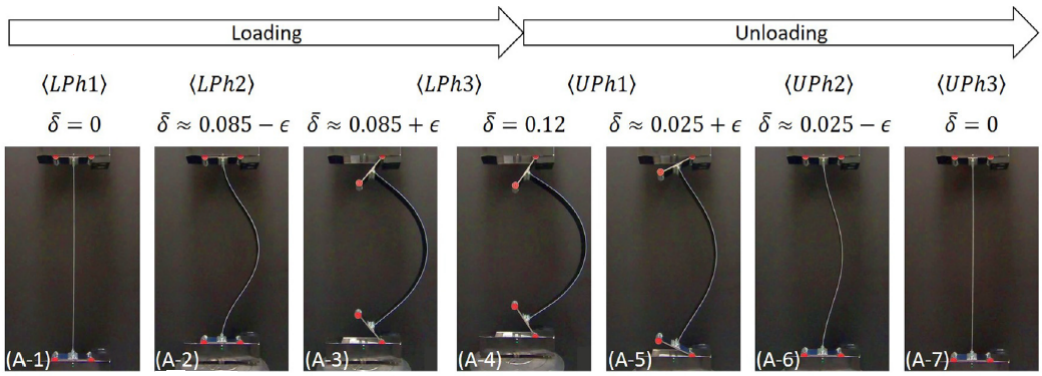

(a) Experimental compression test

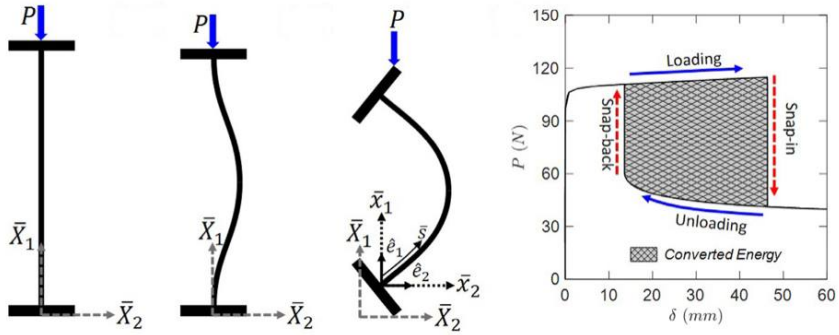

(b) Load-displacement curve with highlight of the hysteresis cycle

Figure 1.11: Weakening-induced snap instability, summary of the work conducted by *Heo et al.* [16]

3. Negative stiffness honeycomb was a concept patented in 2016 by *Seepersad et al.* [17], using a cellular structure made of slender curved beams, which, upon transversal compression loading, are configured to snap to a second equilibrium position upon experiencing a force threshold. This deformation is accompanied by a negative slope portion in the load-displacement curve, which gives the characteristic name to the structure.

Among these concepts, the last one was selected as the most promising for the following reasons:

- Computationally it was the easiest and most immediate to analyze, without need to characterize the material thermically, as in the first case, and with relatively fast simulation times, without accounting for the heating and cooling cycles, necessary for the activation of Shape Memory effect;
- As for the second concept, it exploits a similar deformation through buckling of a straight beam, however the weakening boundary conditions are considered not reliable with respect to the snap-through behaviour of the Negative stiffness curved beams, which do not have moving parts, with a much simpler design and less likely to fail;
- The negative stiffness honeycomb was reported to be the most effective method in terms of amount of energy absorbed, especially exploiting the possibility of using high performance metals [18]

1.4 Negative stiffness Honeycomb

1.4.1 General behaviour

The cells of negative stiffness honeycomb, depicted in fig. 1.12 are composed of several curved beams which undergo compressive loading in the middle that causes a transition from one stable buckling mode clamped-clamped beam to another curved in the opposite direction.

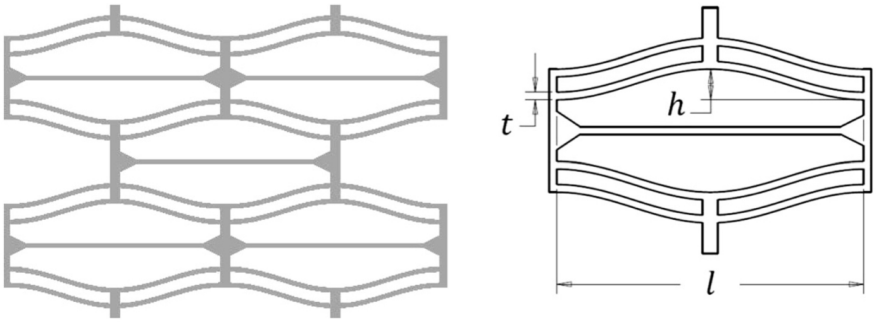

Figure 1.12: Characteristic dimensions of the negative stiffness cell [11]

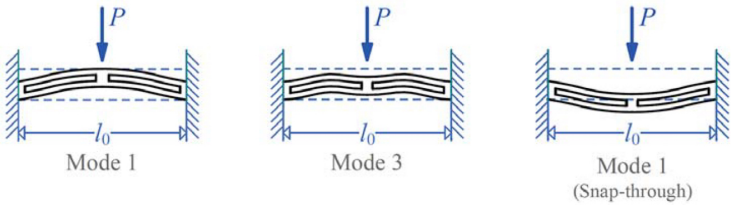

Figure 1.13: Deformation mode of negative-stiffness beam with snap-through behaviour[19]

This type of deformation, represented in fig. 1.13 is called *snap-thorugh behaviour* and results in a region of negative slope in the force-displacement plot 1.14 [9], creating an oscillating response similar to the one of metal tubes presented previously in chapter 1.2.1 (fig. 1.2).

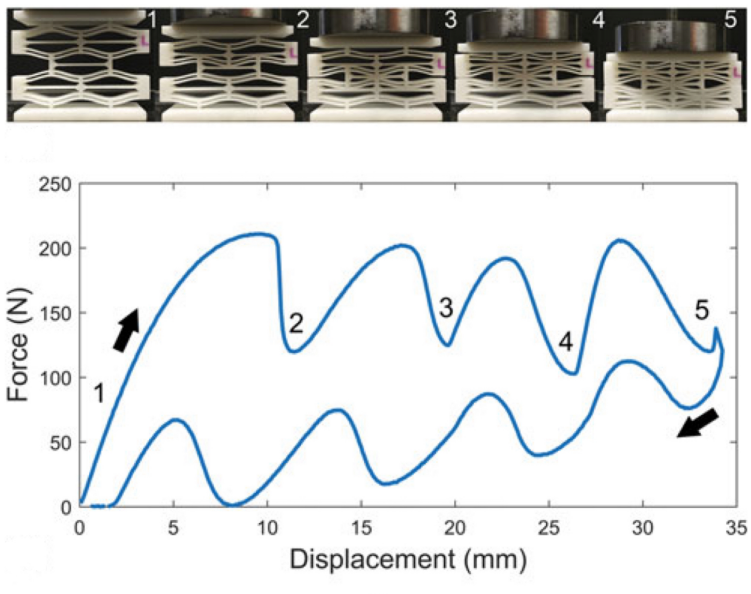

Figure 1.14: Force-displacement plot of negative stiffness honeycomb with associated deformation phases [9]

The base mechanism of recoverable buckling curved beam has been researched by early 2000s by *Qiu* [20], who suggested the possibility to use it in MEMS (Microelectromechanical systems) for their bistability properties. In fact, if the geometrical parameters are designed correctly, the beam is able to block itself in the deformed configuration after transversal actuation and be easily reversible with the application of small load in the opposite direction. The transition of the buckled beam from one stable position to another is accompanied by the reduction of force which results in the release of the absorbed energy [19]. Looking at the response in the Force-displacement graph, the bistability phenomenon happens if the Force becomes negative, during the *snap-through* event.

In this decade the concept was exploited in a honeycomb configuration, creating a structure able to absorb energy elastically to provide impact resistance [19].

The sequence of negative stiffness behaviour cell can be tailored to achieve a plateau, like the one of regular honeycomb structure, with high energy absorption capabilities at an almost constant force threshold; however in this case the deformation is achieved through elastic or partially elastic buckling, and therefore could be recovered several times before failure.

The peculiarity of this metamaterial is the innovative way to store energy elastically. Every type of absorber, when loaded, experiences an elastic response, however, in most of the cases the time duration and the displacement is so little to be neglected. For example, considering an aluminum circular tube crushed in the axial direction, the elastic response consists only of the first fractions of millimeters, while in a negative stiffness honeycomb the elastic displacement of the structure under impact is in the range of tens or hundred of millimeters.

As can be observed in fig. 1.14 the experiments conducted by *Debau et al.* [9], show the presence of an hysteresis loop in the force-displacement curve: when the unit cell is unloaded in a displacement controlled way after being compressed, the recovery deformation follows a different path with respect to the loading curve [21]. The result proved the potential use of this types of structures as energy absorbers [22]: the total energy dissipated by the structure is equivalent to the difference between the integral of the loading and unloading curves over time.

1.4.2 Advantages

The capability of Negative stiffness honeycomb to recover the deformation after impact is of great interest for shock absorbing devices.

In fact it would reduce drastically the maintenance costs and requirements associated to energy absorbing devices: after an impact the reusable energy absorber does not need any substitution, only minor inspection to assess the possible damage of the structure.

The capability to withstand continued compression cycles and impacts could be particularly useful for making durable personal protection devices, for sports or for work. Furthermore, the recoverability of the honeycomb can be exploited to develop re-usable packaging able to protect the content from several impacts [22].

Most importantly, negative stiffness honeycomb are extremely interesting because of their versatility.

In general, they can be made of any sort of material: the characteristic dimension of the cell can be customized to have the desired force threshold an energy absorption capability. The reusability of the structure is determined by the special geometrical shape of the cell, not by the material specific properties. In fact, the maximum value of deformation during the deflection of the beam has been analitically calculated by *Qiu* [20] to be equal to eq. (1.5), and it only depends on geometrical parameters of the cell referring to fig.1.12.

$$\epsilon_{max} = 2\pi^2 \frac{th}{l^2} \tag{1.5}$$

In order to have a total elastic recoverable material this maximum strain should be within the yield strain of the base material.

Studies conducted by *Debau* [9] and *Correa* [22] experimented the possibility of producing bidimensional absorbers with negative stiffness honeycomb shape with additive manufacturing using SLS technology (Selective Laser Sintering) and Nylon 11 as a material, for its high toughness and wide range of elasticity.

Debau [9] has also proven the concept feasible for aluminum construction produced by waterjet, in order to increase the mechanical characteristics and the amount of energy absorbed. In this case, the yield strain of the metal is much lower with respect to the plastic, hence the length of the beam has been increased and the height of the middle section has been decreased, in order to decrease the maximum deformation, following eq. (1.5); the difference in the characteristic dimensions of the honeycombs in the two materials in the research by *Debau* is underlined by the comparison in fig. 1.15.

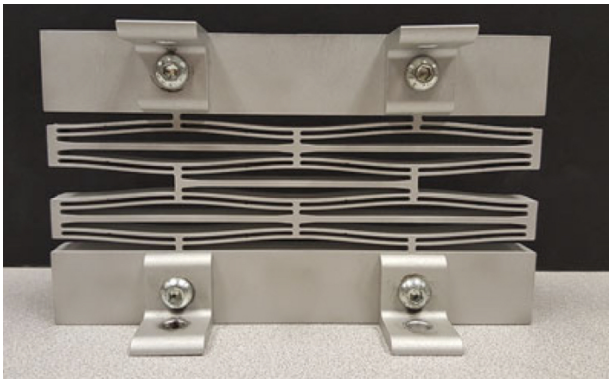

(a) Negative Stiffness honeycomb in aluminum by Waterjet

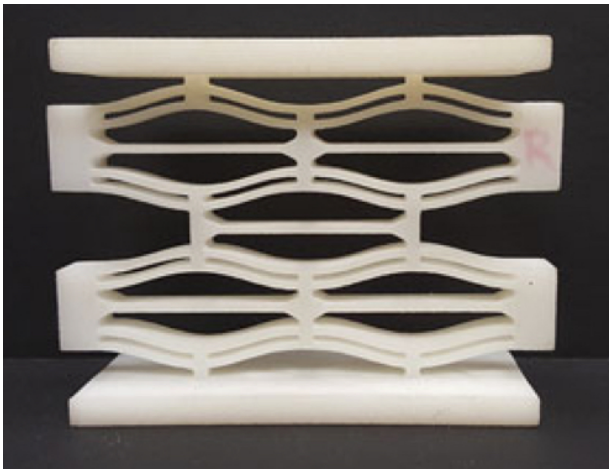

(b) Negative Stiffness honeycomb in Nylon by SLS

Figure 1.15: Visual comparison of Negative Stiffness honeycombs experimented by *Debau* [9] in two different materials

Differently, *Tan et al.* have abandoned the concept of elastic recovery proposing a steel negative stiffness structure which dissipates energy through plastic deformation [18]. In this case, the deformation is reversible applying a force in the opposite direction with respect to the impact and the possibility to recover the deformation can be exploited only a few times. However, the amount of energy absorbed substantially increases during the impact.

Regardless of the possibility of plastic deformation, the negative stiffness honeycomb is an ingenious way to absorb energy via elastic instability. A limited elastic response is expected in any type of absorber, however it is typically limited to the first micrometers of displacements and small fractions of milliseconds during the impact. Negative stiffness honeycomb manage to improve massively the usable displacement during elastic response.

1.4.3 Current limitations

The amount of energy absorbed through elastic deformation in Negative stiffness honeycombs reported in literature is generally much smaller with respect to plastic deformation in conventional absorbers.

In fact, *Correa* in his article [22] compared the performance of a negative stiffness honeycomb with the one of a conventional hexagonal honeycomb under in-plane compression, analyzed in paragraph 2.2.1. His Negative Stiffness honeycomb was characterized by a specific energy absorbed of 65 $\frac{mJ}{g}$ with an efficiency of 65 %, while the hexagonal honeycomb showed a better performance at 162 $\frac{mJ}{g}$ of specific energy absorbed and an efficiency of 86 %.

However, unlike hexagonal honeycomb, which configuration cannot be modified, except for the adjusting of relative density, performance of negative stiffness honeycomb can be improved modifying the thickness, apex height and length of the beam [22]. So *Correa* suggested, but did not proved the possibility of optimizing the dimensions of the cell to maximize the energy absorbed, managing to achieve in simulations a very similar value of specific energy with respect to positive stiffness hexagonal honeycomb.

Moreover, in contrast with hexagonal honeycombs, which are characterized by an energy absorbed quadratically proportional to the relative density of the cells (expressed by the ratio $\frac{t}{l}$), as pointed out in eq. (1.4), the compression energy of Negative stiffness Honeycombs tends to increase with decreasing relative density, and the effect is more pronounced increasing the force threshold by calibrating geometrical parameters [11]. This trend is shown clearly in fig. 1.16.

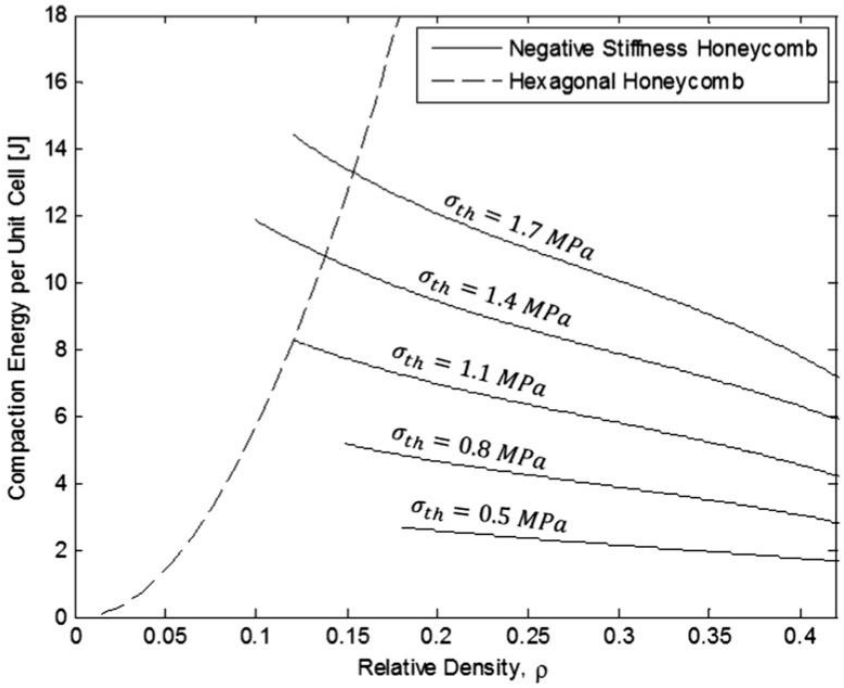

Figure 1.16: Comparison between Energy absorbed by hexagonal and negative stiffness honeycomb varying the relative density of the cells [11]

An other crucial aspect of energy absorption is managing the safety of the crash event. In fact it is essential that during the impact the energy is absorbed in a controlled way, without harming the surrounding environment. The use of a totally elastic absorber could be dangerous in a high velocity impact because the object could bounce back still with significant energy. However, if used in combination with a plastic deformation energy absorber, like suggested in the first paragraph, the negative stiffness honeycomb could ensure partial recoverability of energy absorption properties after an impact and create longer-lasting impact-protection devices [22].

1.5 Aim of the study

The aim of this thesis was to design and manufacture a functional reusable crash absorber, able to recover deformation after compression, based on the concept of Negative Stiffness Honeycomb, introducing some key features to improve the functionality of the device with respect to previously published studies in terms of performance, reliability and cost effectiveness.

Particularly, the focus of the work consisted in developing and experimenting the reusability of the absorber not only in static compression tests, like already researched by *Correa et al.*[22] and Tan et al.[18] , but also in dynamic compression tests at higher velocity, specifically for an effective and safe use in crash events.

Chapter 2

Design workflow

The negative stiffness honeycomb allows great flexibility in design, the deformation behaviour depends greatly on the geometry. The characteristic parameters can be tuned to have a desired response. Hence, in this thesis, the design of the prototypes followed a precise design workflow from the theory to the testing of prototypes, following these steps:

1. Theoretical Computations
2. Numerical Simulations
3. Production of prototypes by Additive Manufacturing
4. Testing

2.1 Theoretical computations

2.1.1 Governing equations

The deformation of the pre-shaped curved beam, constitutive element of the negative stiffness honeycomb, has been mathematically analyzed by *Qiu et al.* [20] and *Mehreganian et al.* [19]. The description of the initial undeformed buckled shape can be derived from the beam differential equations following the Eulero-Bernoulli theory for a straight beam with uniform material and section properties, subjected to an axial load p [20], reported in eq. (2.1).

$$EI_{yy}\frac{d^4w}{dx^4} + p\frac{d^2w}{dx^2} = 0 \tag{2.1}$$

By applying the typical Dirichlet boundary conditions for a clamped-clamped beam reported in eq. (2.2), two non zero classes of solution are obtained, reported in eq. (2.3) for odd antisimmetric modes and in eq. (2.4) for even simmetric modes, as systems of eigenvectors and respective buckling loads N_j as eigenvalues.

$$w(0) = 0; w'(0) = 0; w(l) = 0; w'(l) = 0; \tag{2.2}$$

$$\begin{cases} w_j(x) = C\left[1 - 2\frac{x}{l} - cos\left(N_j\frac{x}{l} + \frac{2sin(N_j\frac{x}{l})}{N_j}\right)\right] \\ N_j = 2.86\pi, 4.92\pi... \end{cases} \quad ; j = 2, 4, 6, ... \tag{2.3}$$

$$\begin{cases} w_j(x) = C[1 - cos(N_j\frac{x}{l})] \\ N_j = (j+1)\pi \end{cases} \quad ; j = 1, 3, 5, ... \tag{2.4}$$

The resulting as-fabricated shape of the negative stiffness beam (fig. 2.1), is represented by the first buckling mode shape in eq.(2.5) [20]

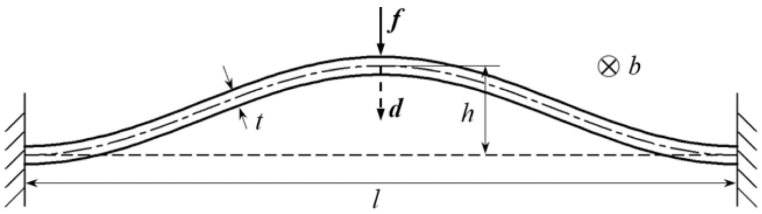

Figure 2.1: Initial shape of negative stiffness beam

$$w_0(x) = \frac{h}{2}[1 - cos(2\pi\frac{x}{l})] \tag{2.5}$$

The buckling modes for the straight clamped-clamped beam reported above in eq. (2.3) and (2.4) constitute an orthogonal set, that can be used as constitutive base for the description of the shape of the initially curved beam under transversal load f [20], following the principle of *modal condensation*, schematized in eq. (2.6). This concept allows to best capture the physics of the phenomenon, and obtain equilibrium solution for complex problems like this.

$$w(x) = h\sum_{j=1}^{\infty} A_j w_j(x) \tag{2.6}$$

During the application of the transversal load f the beam experiences a change of length corresponding to eq. (2.7), which arouses an axial force in the beam corresponding to eq. (2.8)

$$s = \int_0^{l_0} ds = \int_0^{l_0} \sqrt{1 + \left(\frac{dw}{dx}\right)^2} dx \approxeq \int_0^{l_0} 1 + \frac{1}{2}\left(\frac{dw}{dx}\right)^2 dx \tag{2.7}$$

$$p = Ebt(1 - \frac{s}{s_0}) \tag{2.8}$$

At this point, the evolution of the overall vertical displacement of the middle point of the beam d, defined in eq.(2.9) can be evaluated using an energy approach.

$$d = w_0\left(\frac{l}{2}\right) - w\left(\frac{l}{2}\right) \tag{2.9}$$

The main types of energy considered are summarized in eqs. (2.10):

- The membranal energy (E_{ax}) due to the onset of the axial stress from eq. (2.8)
- The bending energy (E_b) from the differential equation (2.1)
- The energy associated to the external transversal force (E_f)

$$\begin{aligned} E_b &= \int_0^{l_0} \left(\frac{\partial^2 w_0}{\partial x^2} - \frac{\partial^2 w}{\partial x^2}\right)^2 dx \\ E_{ax} &= -\int_0^{l_0} p ds \\ E_f &= -Fd \end{aligned} \tag{2.10}$$

A stable deformed configuration is reached through a minimization of the total energy of the system, which is the sum of the energy forms given in eqs. (2.10).

As a result, the coefficients associated to the basis (2.6) are reported in eq. (2.11).

$$\begin{aligned} A_1 &= -\frac{1}{2}\frac{N_1^2}{N^2 - N_1^2} + \frac{4F}{N_1^2(N^2 - N_1^2)} \\ A_j &= \frac{4F}{N_j^2(N^2 - N_j^2)};\ j = 5, 9, 13, ... \end{aligned} \tag{2.11}$$

Where F and N stand for the normalized transversal and axial load, defined in eq. (2.12)

$$F = \frac{fl^3}{EI_{yy}h};\ N^2 = \frac{pl^2}{EI_{yy}} \tag{2.12}$$

The remaining coefficients are either null if $N^2 < N_j^2$, or the corresponding mode must be constrained if $N^2 > N_j^2$; when $N^2 = N_j^2$ any value is accepted [20].

Neglecting the higher order terms in eq. (2.11) there are three solutions to this minimization problem, summarized in eq. (2.14) and fig. 2.2, which result in stable deformed configurations [20].

They are written in terms of evolution of transversal force with respect to Δ, defined in eq. (2.13) as the downward vertical displacement of the middle of the beam d, normalized on the initial apex height h.

$$\Delta = \frac{d}{h} \tag{2.13}$$

$$\begin{aligned} F_1(\Delta) &= \frac{3\pi^4 Q^2}{2}\Delta\left(\Delta - \frac{3}{2} + \sqrt{\frac{1}{4} - \frac{4}{3Q^2}}\right)\left(\Delta - \frac{3}{2} - \sqrt{\frac{1}{4} - \frac{4}{3Q^2}}\right) \\ F_2(\Delta) &= 4.18\pi^4 - 2.18\pi^4\Delta \\ F_3(\Delta) &= 8\pi^4 - 6\pi^4\Delta \end{aligned} \tag{2.14}$$

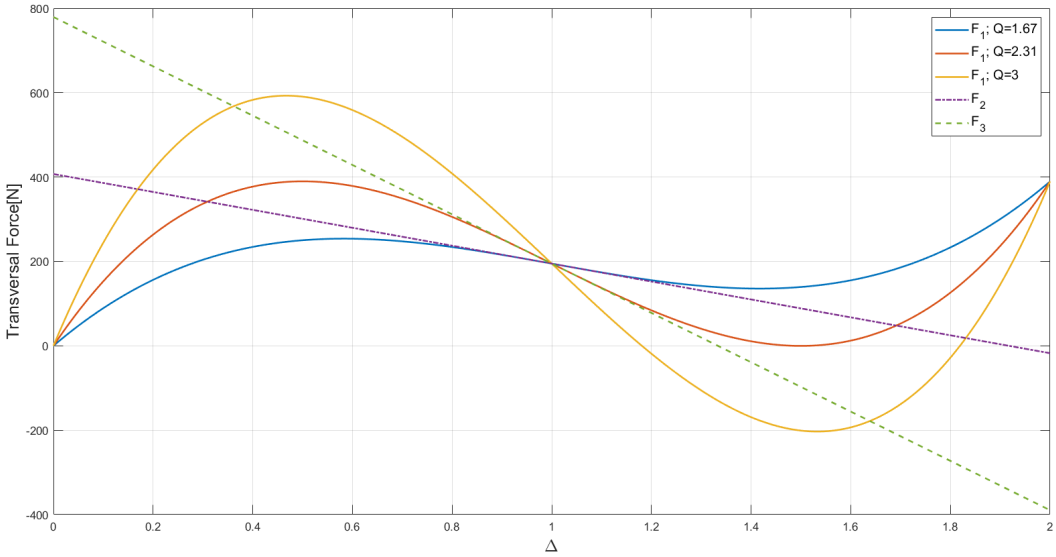

Figure 2.2: Solutions to the deformation problem of the curved beam on $F - \Delta$ graph

Only the first solution is a function of geometric parameters of the cell (specifically $Q = \frac{h}{t}$) while the second and the third solution are lines with constant slopes for each value of the characteristic dimensions of the cell, corresponding to the critical axial loads for the second and third buckling modes.

In particular, there are two critical values for F_1, depicted in fig. 2.2:

- for $Q = \frac{2N_2}{\sqrt{3}N_1} = 1.67$, F_1 becomes tangential to F_2
- for $Q = \frac{2N_3}{\sqrt{3}N_1} = 2.31$, F_1 becomes tangential to F_3

When Q becomes larger than 2.31 there are two more intersections with F_2 and F_3. In this case the force follows an hybrid path during the vertical displacement of the center of the beam as represented in full line style in fig. 2.3

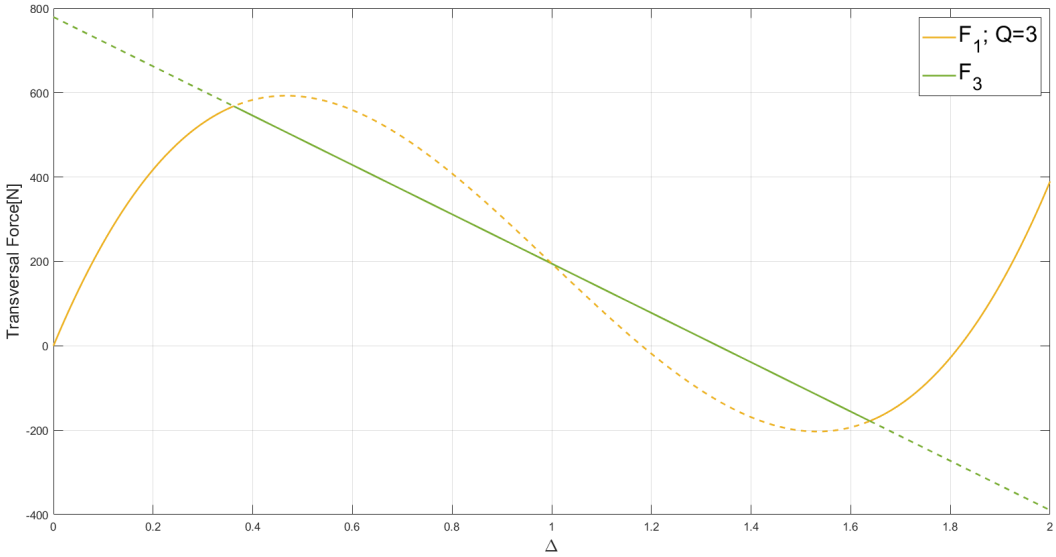

Figure 2.3: Hybrid Force-displacement curve during transition from first to third mode

The deformation path of the buckled beam can be separated in three different phases:

1. At the beginning of the deformation, until the axial force N, due to the change of length of the beam, is less than the second or third order buckling threshold, reported in eq.2.3 and 2.4, the transversal force follows the sinusoidal path of F_1
2. Increasing the displacement, the axial load reaches the critical buckling value at the intersection with F_2 line, if the second mode is not constrained, or F_3 line, if the second mode is constrained. This phase triggers the onset of the *snap-through* phenomenon [19], and the characteristic negative stiffness path is followed, with a progressively decreasing force until reaching a second stable position.
3. After the second intersection point with F_1 the force goes back to the initial sinusoidal path following a positive slope curve, with the beam blocked in the second deformed equilibrium position

As can be seen in fig.2.2 the second mode deformation (equivalent to F_2 shape), significantly reduces the force threshold of the beam and the magnitude of its negative stiffness properties

[11]. For this reason, the negative stiffness cell is designed so that there are two equal curved beams clamped at the middle with a vertical beam.

With this addition, as can be seen from fig. 2.4 the second mode is constrained, since the clamp in the middle forces a null slope of the beam; hence, the *snap-through* behaviour becomes a second stable solution to the deformation problem.

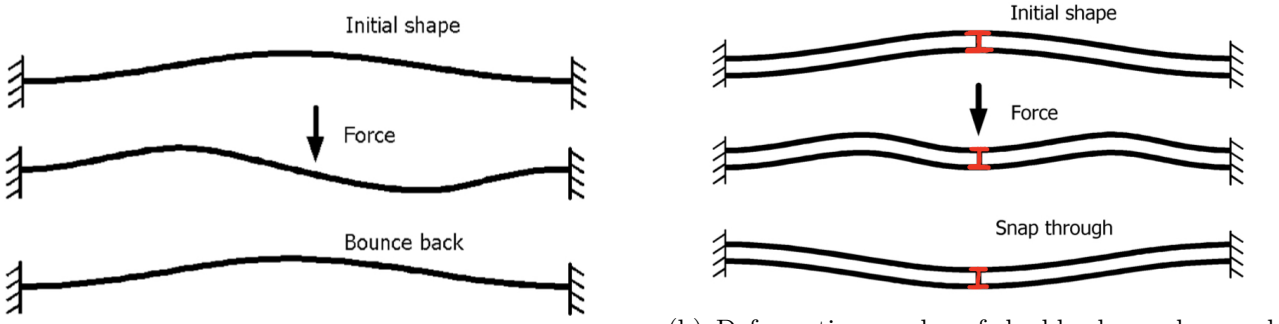

(a) Deformation modes of single curved beam

(b) Deformation modes of double-clamped curved beams

Figure 2.4: Comparison between deformation mode of curved beams [20]

2.1.2 Geometrical parameters of the cell

The first step in the design of NS honeycomb is the choice of characteristic geometric dimensions of the cell. The two main design parameters are the thickness of the beam t and the bistability ratio Q, which together define the apex height h.

Considering the analytical computations reported hereinabove in paragraph (2.14) a parametric analysis has been performed to investigate the influence of geometric parameters and material characteristics on the final performance of the negative stiffness pre-shaped curved beam.

In this context the material characteristics are considered as constraints to the design problem. The recoverability of the deformation is limited by the value of maximum deformation reached, with respect to the yield deformation ϵ_y of the chosen material.

During the deformation the beam is subjected to a combination of axial and bending stress; assuming a constitutive linear relation between the stress and strain the maximum value of deformation can be approximated in closed form with eq.(2.15) [20], depending only on geometrical parameters of the cell.

$$\epsilon_m = \frac{\pi^2 th}{l^2}\left(2 + \frac{4}{3Q}\right) \approxeq \frac{2\pi^2 th}{l^2} \tag{2.15}$$

Looking at the graph 2.6, it's clear that maintaining the same material (hence the same value of yield deformation ϵ_y) an increase of the thickness always constitutes an increase in the peak force, however, if the apex height is increased over a certain bistability ratio the force reaches a plateau. This is caused by the consequent increase in the length of the beam, as shown in eq. (2.15) and in fig. 2.5; this parameter does not enter in the adimensional formula for the computation of the force (2.14), but considering the real dimensional force of eq. (2.7) It is inversely proportional to the third power of the length of the beams: l.

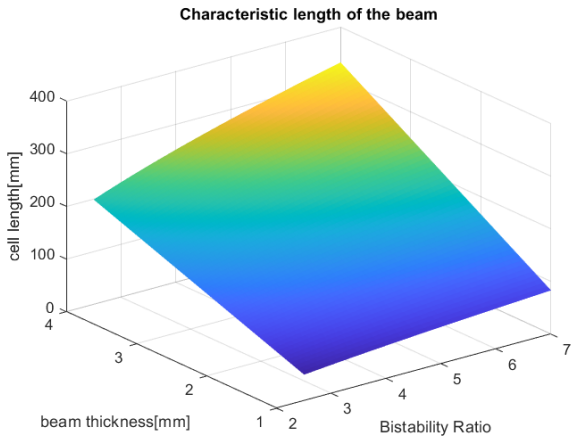

Figure 2.5: Length of the cell vs beam thickness vs bistability ratio

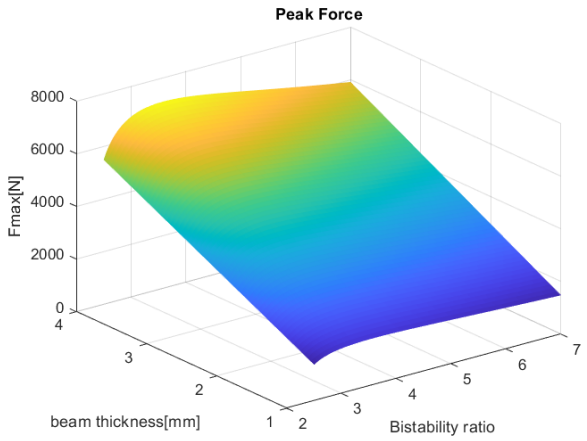

Figure 2.6: Peak Force vs beam thickness vs bistability ratio

Considering instead the energy absoprtion in fig. 2.7, we can notice that for low values of thickness the increase in bistability ratio does not influence greatly the performance; instead, increasing the thickness, a simultaneous increase in apex height brings to a higher energy. This behaviour is different from the one observed with the peak force, because the energy absorbed during the impact is the integral of the compression force over the total displacement of the middle point (from 0 to $2h$), hence It does not depend only on the peak force, which value is limited, but also on the duration of negative stiffness behaviour, which is proportional to the bistability ratio and, in the end, lead to an increase in the energy absorbed, as can be seen in fig. 2.8

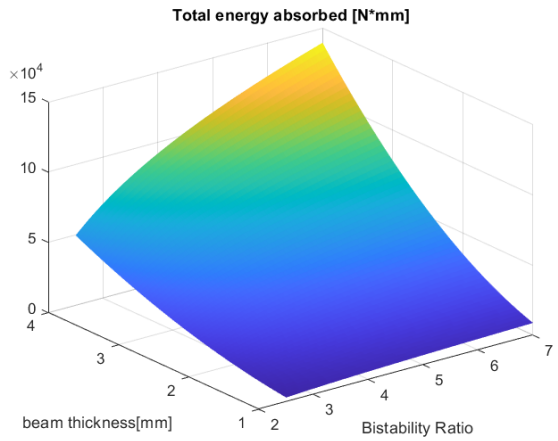

Figure 2.7: Energy absorbed vs beam thickness vs apex height

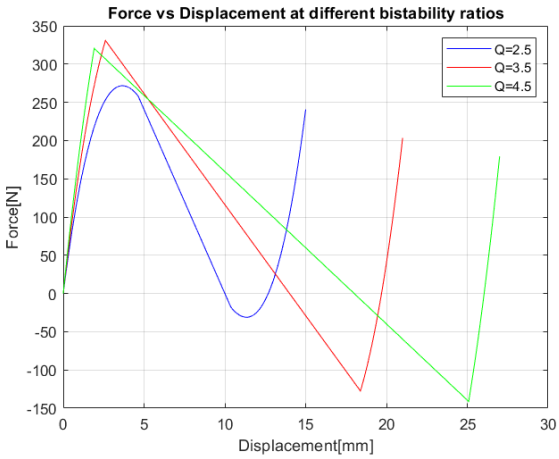

Figure 2.8: Force graphs of preshaped curved beam varying bistability ratio with constant beam thickness

Other important performance requirements to consider for this types of cellular lightweight energy absorbing devices are also the specific energies. As can be seen in fig .2.9 the specific energy per unit mass is influenced positively by an increase in both the beam thickness and apex height, the consequent increase of the length of the beam does not influence much the result. Differently, looking at the specific energy per unit of volume in fig. 2.10 , given the unique configuration of the pre-shaped curved beam, the space volume occupied is a rectangular box of dimensions$(h + t) * L$, which is much higher with respect to the pure thickness of the

beam; hence this performance is affected negatively by an increase of bistability ratio (which brings to a higher apex height and length of the beam).

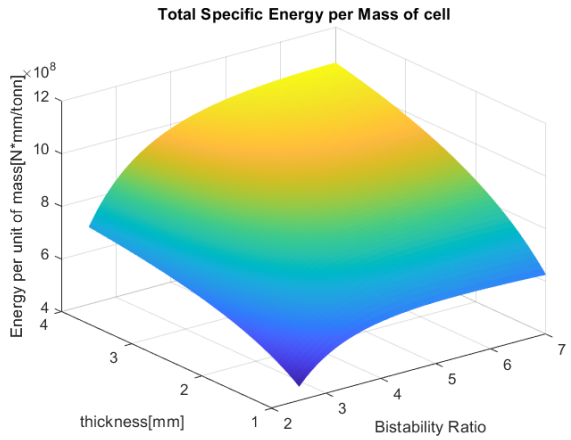

Figure 2.9: Specific energy per mass vs thickness vs bistability ratio

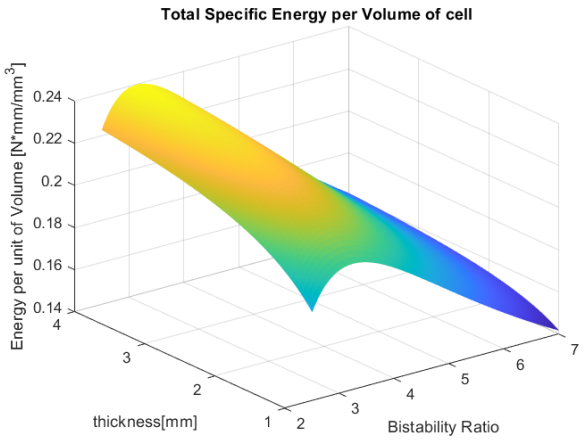

Figure 2.10: Specific energy per volume vs beam thickness vs bistability ratio

2.2 Numerical Simulations

Numerical simulations are very useful tools in structural design for several purposes:

- Predicting the results of experimental tests, computing the stress and deformations, in order to cut time and cost on manufacturing, producing a final functional and safe model without many iterations;
- Exploring the behaviour of different technical solutions fast and inexpensively, as well as performing structural and parameter optimizatios
- Extending the results of experiments to conditions difficult to achieve in normal experimental tests due to their complexity and cost.

The negative stiffness honeycomb prototypes have been designed using the finite elements software LS-Dyna ® by ANSYS . FEM (Finite Element modeling) is a numerical technique, which computes the displacement of a generic point in space by discretizing the geometry of the model in base constitutive partitions (elements), each delimited by extremities point (nodes), which become unknowns of structural problem. The simple formulation of the elements allows to establish analytic interpolation laws to compute the displacement of a generic point inside of it directly from its nodes.

This type of software is specialized in non linear explicit simulations. In fact, in the linear formulation of the structural problem stands the hypothesis of small displacements with respect to the characteristic length of the problem.

This assumptions brings to several restrictive consequences:

- The undeformed configuration, where the geometry has been discretized, can be approximated to be equal to the unknown deformed configuration, where the principle of virtual work should be solved and the deformation should be computed.
- The formulation of the structural problem is much simplified, as the interpolation laws are not modified during the deformation.

- It is only possible to consider a linear elastic behaviour of the material, assumption which can be considered valid in a wide range of problems, where it exists a direct proportionality law between stress and strain. Entering in the plastic field of the material the linear formulation cannot be applied anymore.
- Loads and boundary conditions are defined in fixed Eulerian reference system, applied statically, without considering an history or a dynamic variation in time
- Contacts between different parts of the structure are not considered

As a result of the previous considerations the behaviour of the Negative Stiffness Honeycomb cannot be considered a static linear problem. In fact, the whole mechanism is thought in order to have a negative slope change in the response of the structure, totally different from a normal linear behaviour, even if the base material of the structure is supposed to remain in the elastic state. For every snapping-through buckling instability of the honeycomb the stress are redistributed in the rest of the structure, captured only by dynamic simulations. Moreover, the shape of the curved beams is deeply affected during the deformation of the structure, with a maximum displacement of $2h$ in the middle point.

Non linear formulation of PVW

The constitutive relation of any finite element software for structural application is the Principle of Virtual Works, which states that necessary and sufficient condition for the equilibrium of a structure is that the sum of the virtual works, intended as scalar product of real set of forces, scalarly multiplied by a set of virtual displacements, is null.

Virtual displacement are intended to be arbitrary, infinitesimal and congruent to boundary conditions.

Typical dynamic formulation of the PVW is reported in equation (2.16)

$$\int_V \delta\boldsymbol{\epsilon}^T \boldsymbol{\sigma} dV = \int_V \delta \boldsymbol{s}^T \boldsymbol{F_{ext}} dV - \int_V \delta \ddot{\boldsymbol{s}}^T \rho \, dV \tag{2.16}$$

Where $\boldsymbol{\epsilon}$ is to be intended as a vector made by the six components of the Green-Lagrange deformation tensor, a generalized form of the strain tensor for large displacements, fully explained in [23]. In space coordinates, the vector is described by the following relations (2.17)

$$\boldsymbol{\epsilon} = \boldsymbol{\epsilon_L} + \boldsymbol{\epsilon_{NL}} = \begin{Bmatrix} u_{/x} \\ v_{/y} \\ w_{/z} \\ u_{/y} + v_{/x} \\ u_{/z} + w_{/x} \\ w_{/y} + v_{/z} \end{Bmatrix} + \begin{Bmatrix} \frac{1}{2}(u_{/x}^2 + v_x^2 + w_{/x}^2) \\ \frac{1}{2}(u_{/y}^2 + v_{/y}^2 + w_{/y}^2) \\ \frac{1}{2}(u_{/z}^2 + v_{/z}^2 + w_{/z}^2) \\ u_{/x}u_{/y} + v_{/x}v_{/y} + w_{/x}w_{/y} \\ u_{/x}u_{/z} + v_{/x}v_{/z} + w_{/x}w_{/z} \\ u_{/z}u_{/y} + v_{/z}v_{/y} + w_{/z}v_{/y} \end{Bmatrix} \tag{2.17}$$

In the case of a linear problem, with the assumption of small displacements and rotations, the deformation vector can be approximated with only the linear term $\boldsymbol{\epsilon_L}$. The quadratic term, which ($\boldsymbol{\epsilon_{NL}}$) become significative in non linear problems with large displacements and rotations, can be simplified with the following formulation, allowing for a representation in terms of nodal displacements.

$$\boldsymbol{\epsilon_{nl}} = \frac{1}{2}\begin{bmatrix} \theta_x^T & 0 & 0 \\ 0 & \theta_y^T & 0 \\ 0 & 0 & \theta_z^T \\ \theta_y^T & \theta_x^T & 0 \\ 0 & \theta_z^T & \theta_y^T \\ \theta_z^T & 0 & \theta_x^T \end{bmatrix} \begin{Bmatrix} \theta_x \\ \theta_y \\ \theta_z \end{Bmatrix} \tag{2.18}$$

where θ_x, θ_y and θ_z, are the spatial derivatives of the displacements (2.19).

$$\theta_x = \begin{Bmatrix} u_{/x} \\ v_{/x} \\ w_{/x} \end{Bmatrix};\ \theta_y = \begin{Bmatrix} u_{/y} \\ v_{/y} \\ w_{/y} \end{Bmatrix};\ \theta_z = \begin{Bmatrix} u_{/z} \\ v_{/z} \\ w_{/z} \end{Bmatrix}; \tag{2.19}$$

The equilibrium equation of the PVW (2.16) must be satisfied independently from the linearity or non linearity of the structural problem.

In general, non linear equations of dynamics can be solved only with numerical approximated methods; in order to be efficiently solved LS-Dyna uses an incremental formulation with an explicit central difference scheme [24], reported in eq. (2.20);

$$\begin{aligned} \dot{\boldsymbol{x}}^{t+\frac{1}{2}} &= \dot{\boldsymbol{x}}^{t-\frac{1}{2}} + \ddot{\boldsymbol{x}}^t \Delta t^t \\ \boldsymbol{s}^{t+1} &= \boldsymbol{s}^t + \dot{\boldsymbol{x}}^{t+\frac{1}{2}} \Delta t^{t+\frac{1}{2}} \end{aligned} \tag{2.20}$$

The reference system and geometry are updated at each time step by adding the displacement increments to the initial geometry, as in eq. (2.21), following a formulation called "Updated Lagrangian".

$$\boldsymbol{x}^{t+1} = \boldsymbol{x}^t + \boldsymbol{s}^{t+1} \tag{2.21}$$

For dynamic problems the velocities and accelerations are computed as following in eq. (2.22)

$$\begin{aligned} \dot{\boldsymbol{x}}^t &= \frac{\boldsymbol{x}^{t+1} - \boldsymbol{x}^{t-1}}{2\Delta t} \\ \ddot{\boldsymbol{x}}^t &= \frac{\boldsymbol{x}^{t+1} - 2\boldsymbol{x}^t + \boldsymbol{x}^{t-1}}{\Delta t^2} \end{aligned} \tag{2.22}$$

Mesh

The horizontal and curved beams have been discretized using shell elements, while the vertical linking beams are modeled with solid elements.

It has been chosen a full cross section integration method to avoid the phenomenon of Hourglassing. In fact, the internal deformation work inside each element is integrated numerically averaging the value in several points. If the number of points is too low the element is under-integrated. In this case It is possible that there are some deformation modes of the element that do not translate into a stress detected in the integration point.

For example, considering a rectangular planar shell element, if only one integration point in the middle is used, there will be five hourglassing shapes for which the total strain detected at the middle, in the integration point, will be zero. This type of deformation is not realistic; however, since It is not detected It propagates fast inside the simulation affecting whole model. There exist five different deformation modes for 4-nodes quadrilateral shell elements and 12 for

8-nodes hexahedral solid elements, which are depicted in fig. 2.11 (showing only the hourglass modes in the x-direction, the other directions are similar)

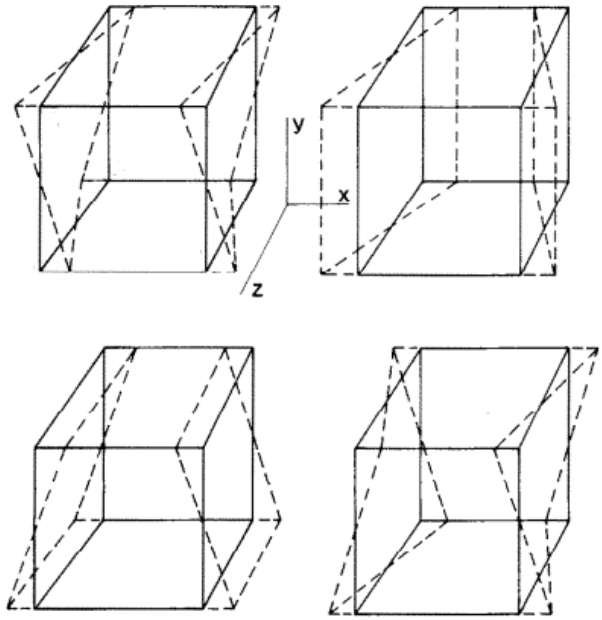

Figure 2.11: Hourglass deformation modes in the x-direction for a 8-nodes hexahedral solid element [25]

The incidence of hourglassing inside a model is usually determined by measuring the *Hourglass Energy*, the energy associated to hourglass modes. A general recommendation, which has been satisfied in the simulations conducted for this thesis work, is to keep It below 10 % of the initial total energy of the system. In fig. 2.12 it is possible to see a failed simulation for excessive hourglass, due to the use of underintegrated shell elements.

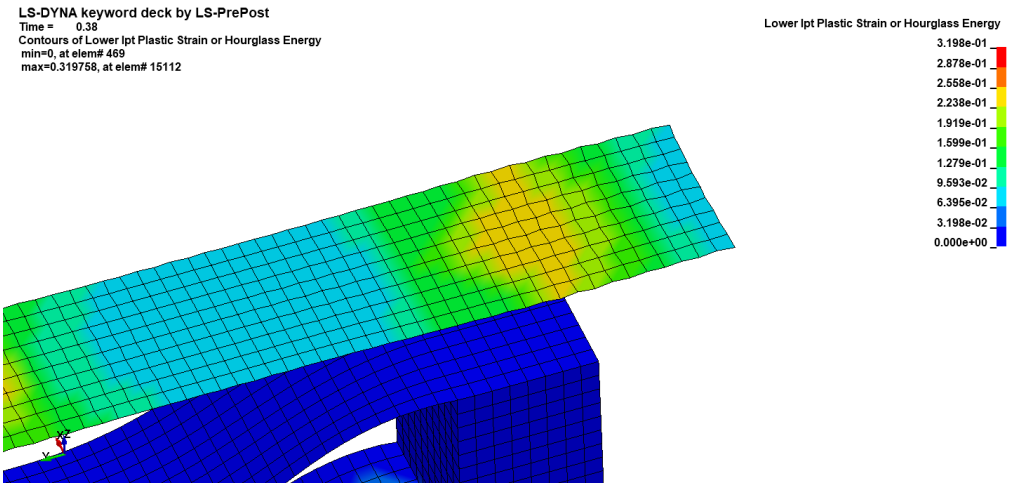

Figure 2.12: Example of propagation of hourglass modes in the simulations if underintegrated element types are used

Generally underintegration and hourglassing are relevant issues in every type of Finite element Simulations, however since the computational cost of Explicit Non linear simulations is generally higher, usually underintegration is used to reduce the simulation time.

Boundary conditions

The base nodes of the structure have been constrained in all six degrees of freedom, without considering any sliding of the base,to restrict the insurgence of lateral instability during the loading of the structure.

Moreover rotation constraints (Rx, Ry, Rz) where imposed at the nodes shared between shell and solid elements, which are represented as an example in fig. 2.13 with red triangular marks.

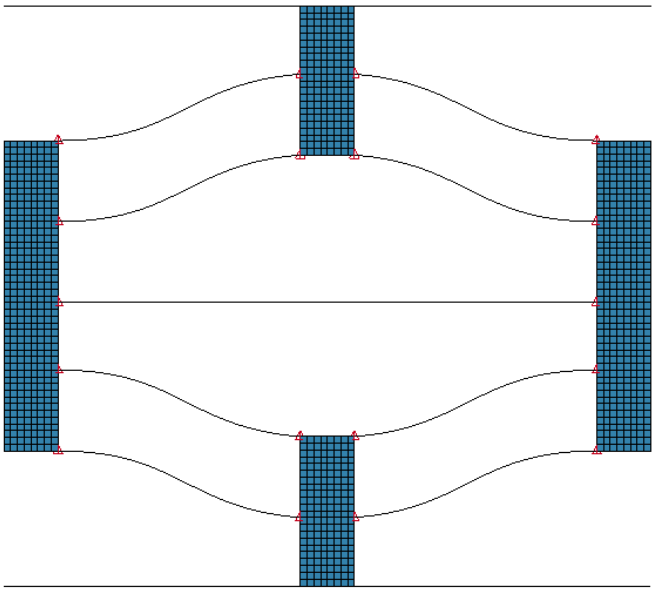

Figure 2.13: Highlight of constraints to the rotational degrees of freedom of nodes shared between shell and solid elements

In fact, the solid elements chosen for the analysis (Element Formulation: 2 [24]) are formulated with only the 3 translational degrees of freedom for each node, given the high torsional stiffness. Hence, if no other constraints were applied, solid elements would not provide a moment support, acting like a pin constraint during the deformation of the beam (fig.2.14c). However, in reality it exists a continuity of material in the proximity of the extremities of the curved beam and the beam keeps its shape at the extremities. As a result, the curved beams maintain always a 90 degrees angle with respect to vertical beams at extremities, if there are not any fractures (fig. 2.14a). As can be seen in fig 2.14, the application of rotation constraints (fig. 2.14d) establishes a correct connection between the vertical beam and the horizontal and curved beams.

This behaviour is observed also in a complete solid formulation of the single cell (fig. 2.14b). This more sophisticate model has been performed only for checking the conformity of the deformations and forces, but It was not selected to use in the actual design process, since each time the characteristic dimensions of the cell changed, a remeshing activity was needed with a pre-processor software. The use of Kirchoff thin shell elements can be considered as a correct approximation of the curved and horizontal beams, since their length is greater of an order of magnitude with respect to their thickness; moreover this simplification makes possible to study different thicknesses of the beams only by changing the section of the shell elements, without long remeshing.

(a) Deformation of 3D printed Nylon NS honeycomb cell, under compression

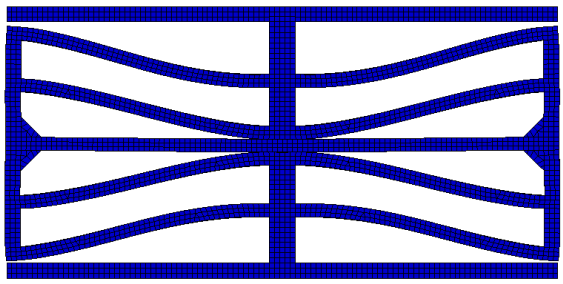

(b) Numerical simulation with shell elements and no constraints on shared nodes between solid and shell elements

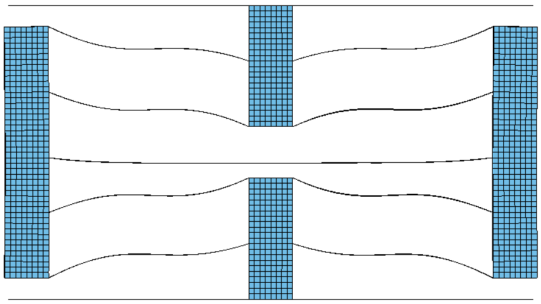

(c) Numerical simulation with shell elements and with rotation constraints con shared nodes between solid and shell elements

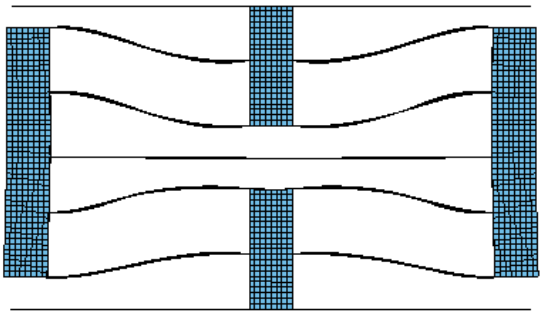

(d) Numerical simulation with shell elements and with rotation constraints con shared nodes between solid and shell elements

Figure 2.14: Comparison of the behaviour of NS honeycomb cell with different modeling techniques

Load Cases and Analysis

The prototypes have been evaluated with a compression test at constant velocity, in displacement-controlled simulations with a boundary motion applied to the nodes on the top surface of the absorber.

During the design phase it was used an explicit simulation at a higher velocity, not compatible with the real one, to keep the simulation time smaller and allow to experiment different characteristic dimensions.

Instead, for the validation of experimental data the compression speed was reduced to a level comparable to the static compression test performed thanks to the use of an implicit solver. In nonlinear implicit analysis, each step is solved iteratively until equilibrium is established within a predefined tolerance; instead in explicit analysis nodal acceleration are solved directly [24], as a result, in order to have a stable solution, the time step in explicit analysis must be less than the time it takes a sound wave to travel across an element, summarized by the formula (2.23)

$$\Delta t = \frac{\Delta x}{c} \tag{2.23}$$

Where Δx is the size of the mesh and c is the speed of propagation of a sound wave across the element, given by eq. (2.24)

$$c = \sqrt{\frac{E(1-\nu)}{(1+\nu)(1-2\nu)\rho}} \tag{2.24}$$

Implicit time-steps have no physical limits and hence, can be greater of several orders of magnitude with respect to explicit analysis, allowing for a higher simulation time. On the other hand implicit analysis requires a numerical solver to invert the stiffness matrix at each time-step; this operation can be computationally expensive for large models.

Moreover, also dynamic impact simulations have been performed on the prototypes of this thesis work, with a rigid mass impacting at an assigned initial velocity.

The accelerations are measured thanks to the outputs of a node of the impacting rigid body. The compression forces are measured by summing the reaction forces of the constraints applied to the boundary nodes on the base of the absorber.

2.2.1 Honeycomb configuration

The analytical computations by *Qiu et al.* [20], reported in the previous paragraph, are a very useful tool to design the geometry of the NS honeycomb. However, comparing them with numerical simulations (fig.2.15) It's possible to spot some differences.

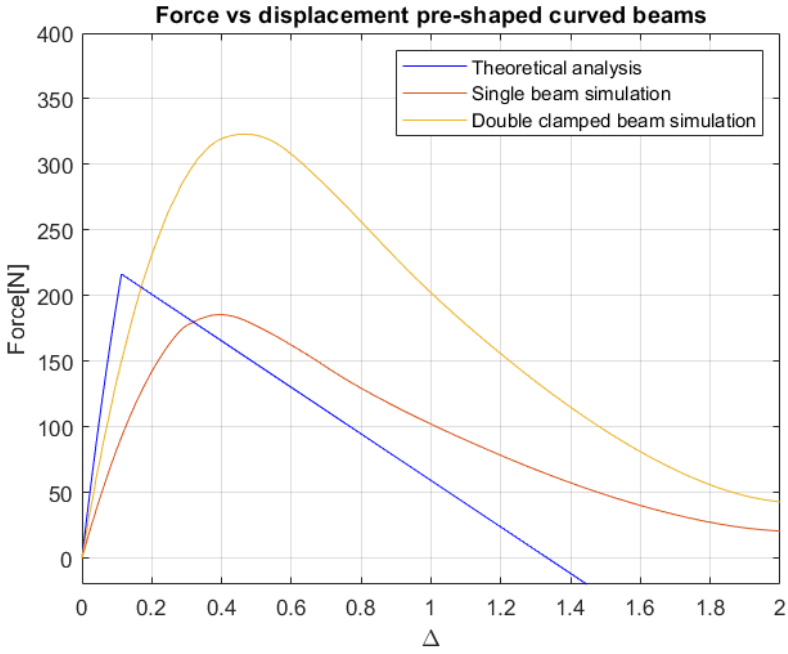

Figure 2.15: Comparison of Force vs Displacement with respect to theoretycal analysis in chap. 2.1.1

First of all, from the literature [20] is not clearly explicited whether these formulas are referred to a single or a double clamped curved beam, however the numerical simulations show that the peak Force value of the single beam is well approximated, with an over-estimation of 14%, while for the double-clamped beams maximum Force threshold is under-estimated by 67 %; as a result the loading curve of the double beam, as used in the honeycomb configuration, results roughly the double with respect to the simulations for the buckling of the single beam, as expected.

Moving to the negative stiffness honeycomb configuration, the negative stiffness double clamped beams are mirrored inside each cell. However, with respect to the analytic formulation of the double curved beam, in this real application the bistability is often restrained by the not ideal boundary conditions, as the vertical beams experience horizontal expansion, which is counteracted by straight horizontal beam in the middle of the cell.

In the simulations, two different behaviours are shown in fig. 2.16 : as also pointed out by *Correa* [22], if the vertical beams at the extremities are free to expand horizontally and rotate, the negative stiffness behaviour and the magnitude of forces are reduced with respect to the previsions, however, if the vertical beams are constrained, the maximum force during the compression is similar to the value for the double curved beam. In both cases, It's possible to notice two different peaks in the force-displacement graph, one for each *snap-through* phenomenon.

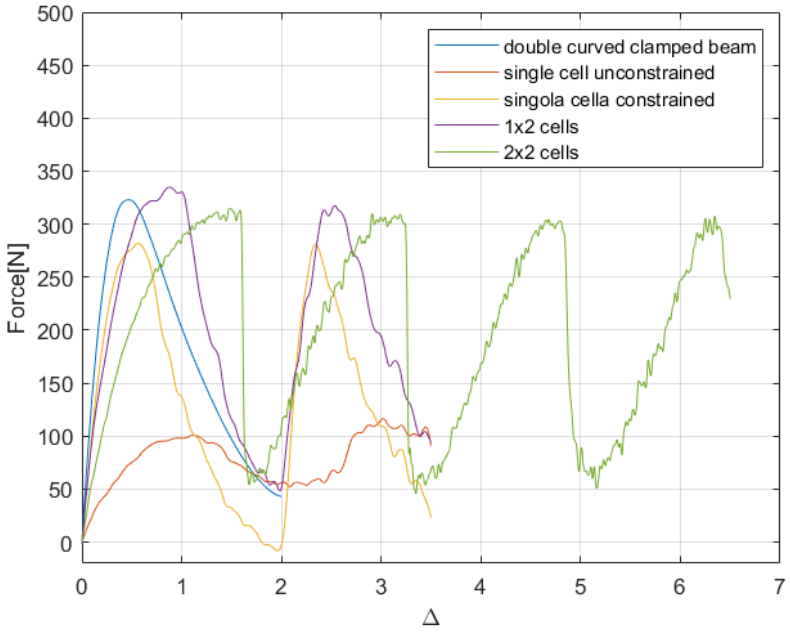

Figure 2.16: Comparison of Force vs displacement plots for different honeycomb configurations in numerical simulations

Applying a roller constraint to the vertical beams makes sense considering the case of a dynamic test, in which the rigid vertical translation behaviour is far more relevant with respect to the horizontal expansion, and plane-rotation; moreover, the phenomenon is exacerbated by the poor mechanical properties of the material considered, in a material with a higher modulus the distance between vertical beams is limited by the tensile modulus of the central horizontal beam.

Considering the parallel configuration, the central sheared beams are constrained, and it's possible to notice that the peak force is greater than both cases of single honeycomb cases: 200% more with respect to the unconstrained cell and 19% more with respect to the bounded honeycomb cell, thus reflecting a mixed situation. Adding more and more cells in parallel only the extremities of external cells will be free to move during compression while the central vertical beams would result subjected to equal expanding forces in opposite directions coming from adjacent cells.

Instead, By adding more rows of honeycomb cells one on top of the other the number of peaks are increased by two for each cell, increasing the stroke and the energy absorption capabilities of the absorber, mantaining a roughly similar force peak

2.3 Production of prototypes

The bidimensional design of the negative stiffness honeycomb cells, combined with their versatility, make them suitable for different choices of materials and production methods.

In this thesis work the first prorotypes were produced by 3D printing in order to experiment different geometries and configurations and prove the reusability of the design, while the final version was made in steel by laser cutting for increased performances.

2.3.1 Additive technologies

Additive technologies where born in the 1980s and where initially addressed as Rapid Prototyping, with the emphasis on creating something quickly, relatively inexpensively, with the output being a prototype, basis model for further developments of the final product [10], allowing to try different design solutions.

However, in the last decades there have been ground-braking improvements in the quality of the output of this machines, hence, this technologies are not used only for prototypes anymore, but also for functional, high-performance parts.

CNC machining, which is also a similarly highly automated, but subtractive technology could remove material in some cases much faster than additive technologies, however they require a significant setup,process and tooling planning, particularly as parts become more complex in geometry, while Additive Manufacturing allow to produce parts in single stage , without much preparation. Hence, the total time accounting tooling to manufacturing results much faster in the additive case [10].

Both technologies are also able to produce highly functional parts, even in metal, however in the case of additive manufacturing, the density of the end result is much lower and, hence also the robustness with respect to the raw material.

In the following table, the main differences and trade-offs between conventional subtractive and additive manufacturing are listed.

Conventional subtractive technologies	Additive manufacturing
High waste of material	Reduced waste of raw material
Best suited for manufacturing large parts	Limited by the size of the printing volume
Increased setup time	Faster and easier setup
High-volume production, where fixed tooling and setup costs can be amortized over a large number of units	Low-volume production of complex prototypes
A wide variety of materials can be used	Thermoplastics and lower performance metals

In this context, there exist several different technologies available. The market for Additive Manufacturing is rapidly growing. In fact, this type of technology has the advantages of reducing cost connected to materials by reducing the waste during manufacturing. Moreover, the increased diffusion during the last years among the general public, continue to reduce the cost for a 3D printer and increase the Return of Investment of this technology.

FDM - Fused Deposition Modeling

This technology is the most simple, affordable and spread type of additive manufacturing technique at the consumer level. FDM is mostly used for proof-of-concept models and low-cost prototyping, hence It has been chosen for the production of the first Negative Stiffness honeycomb prototypes of this thesis work, meaning to prove mainly the reusability of the concept.

It was developed in 1980s by Scott Crump, who registered the patent with the company *Stratasys* ® in 1992 [10]. During the printing process the material, originally in form of a filament, is inserted inside an heated nozzle (extruder), which deposites the fused material on the building plate, as outlined in fig. 2.17. Upon cooling, the layers of material bind with each other and solidify, creating a final product.

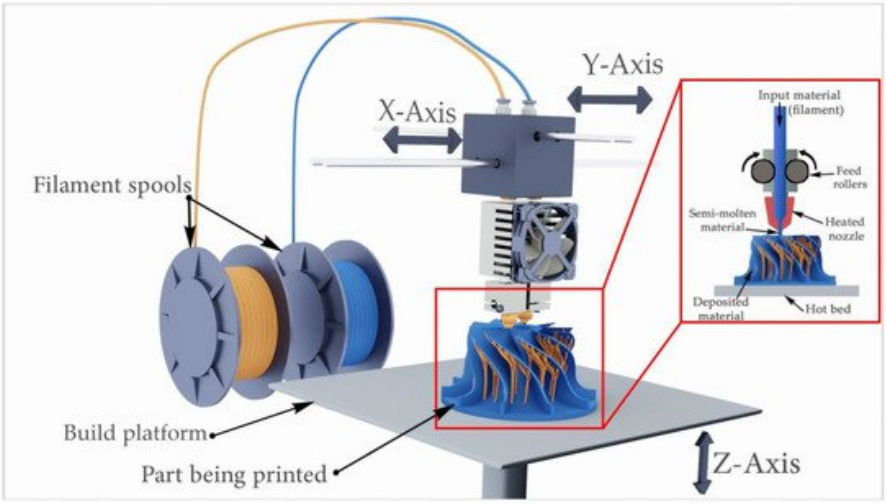

Figure 2.17: Drawing of the main components of a FDM 3D printer [26][27]

The layer-by-layer printing technique and the use of a filament produce a result model which is characterized by a pronounced anisotropy, low dimensional accuracy and rough surface.

Generally FDM printers use thermoplastics materials, which allow for great versatility and low cost, but are not suited for highly functional parts; however, recently, have been developed exceptional desktop 3d printers able to produce metal parts with high density and performance, using Bound Metal Deposition, extruding metal powder held together by polymer binder, which is then removed by heating.

Material

In particular, for the prototypes tested in this thesis work, Nylon has been selected as base material, due to its characteristic mechanical properties. In fact, It exhibits a high value of elongation to yield and a non-brittle failure mode, which bring to an high level of toughness, suitable for this type of application, which exploits greatly the elastic region of the material.

Specifically, It has been used a spool of *Novamid ® ID 1030 Nylon*, produced as a mixture between Polyamide 6 and 66, that allows for increased printability.

The material has been tested with tensile tests according to regulation ASTM D638-14 with specimen of type IV standard [28], showing an elastic modulus of 640 Mpa and a yield strain of 7.8 Mpa; the fracture level was not reached by the specimens, which showed an outstanding elongation up to 200%. The characterization tests were performed with a dogbone specimen, printed in the direction *XX-on edge*, referring to fig. 2.18; in order to have a full accurate description of the material behaviour it should be necessary to print specimens also in the other

directions as well as with 45° infill. More information about material properties and testing can be found in Appendix 6.1.

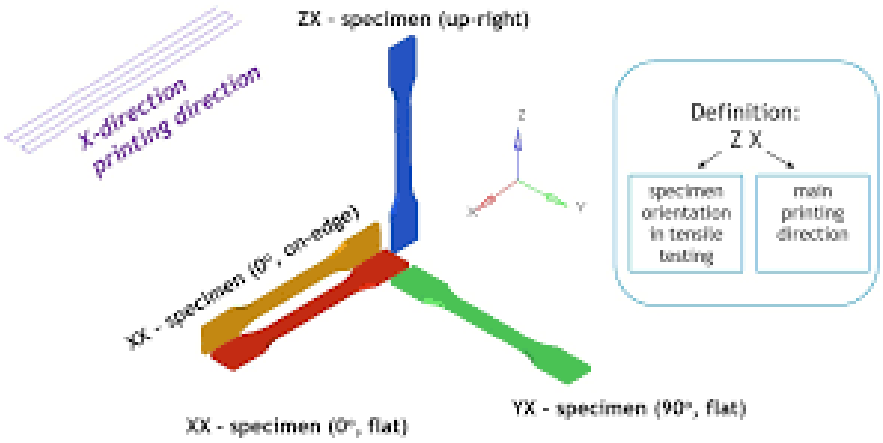

Figure 2.18: Different directions of tensile test specimens for 3D printing FDM materials, as specified in the Technical Datasheet of the material

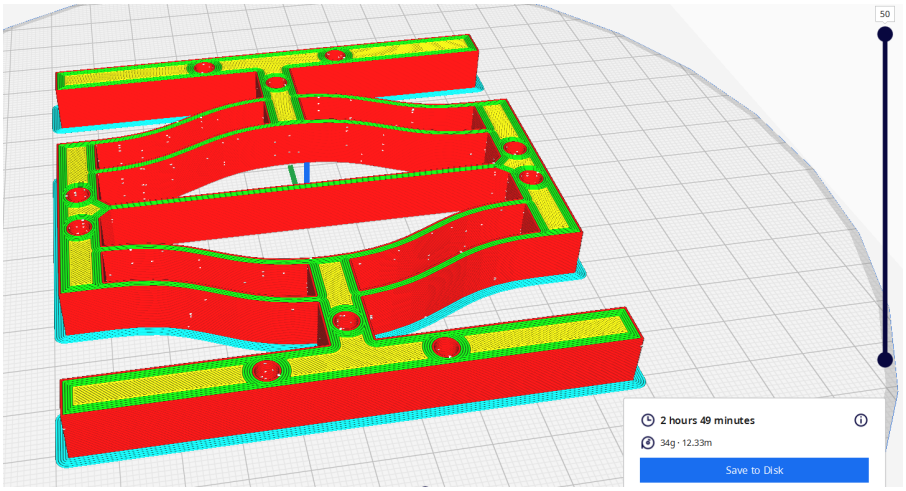

Figure 2.19: Contour of layers of 3D printed Negative stiffness honeycomb cells in the slicing software

However this was the exact printing method of the curved beams, printed on edges with parallel filaments, as can be seen from fig. 2.19 and it was considered sufficient to obtain a good response of the simulations.

The investigation on the numerical modeling of 3D printed FDM materials is still at its infancy, due to the low use for functional applications. For example, *M. Scapin et al.* [29] proposed to model both the wall and the infills with shell elements, however simulating the single filaments of the printing with large dimensions models like the one of this thesis work result in an unfeasible increase in the computational cost. Hence, it has been chosen to use a isotropic material model, consistent through the thickness, with full description of the plastic range obtained by the aforementioned tests.

Even if nylon had been preferred to other thermoplastics for its durability, appropriate to an application of a reusable energy absorber, which must be reliable and able to withstand several usages without damage, on the other hand, this material, in the form of filament for

fused deposition modeling, presents some unique challenges that have been encountered and overcome during the production of the prototypes.

One common flaw observed by Nylon models during printing is the warping. In fact, during the printing process, the difference in temperature between the material, the building plate and the atmosphere creates thermal stresses inside the materials which causes the detachment from the surface; usually this phenomenon appears at the extremities of the part, causing the warping of the final model.

Especially with nylon this problem is exaggerated by its high flexibility, which bring to high elastic tension forces developed during the printing of functional parts with a high percentage of infill, that tends to peel away the material from the building plate.

For this reason the early prototypes present a slight warping and variation of thickness over the length of the horizontal beam, however the phenomenon is not observed in correspondence of the curved beam, which represents the working mechanism of the energy absorption.

In the latter prototypes the warping has been solved with a lower temperature of the bed (Around $85\,°C$), and an enclosure around the spool and the print volume, also heated to $65\,°C$, in order to reduce as much as possible the thermal flow from the print bed to the model and to the surrounding volume.

Process Chain

As already said in the last paragraphs, additive manufacturing emphasizes the simplicity of manufacturing the products from the conceptualization. The design and production process makes extensive use of computer controlling, thus It can be described as a direct or streamlined Computer Aided Design (CAD) to Computer Aided Manufacturing (CAM), with the advantage that this technique requires little or no intervention between the two phases [10]

The process of production of the Negative Stiffness Honeycomb prototypes with 3D printing technology can be divided in the following steps:

1. Models are designed using NX by Siemens ® as CAD software

2. The output of CAD modeling needs to be converted to STL (STereoLitography), the standard format for 3D printing processing, by approximating the surfaces of the piece with a series of triangular facets [10] and removing any other non related data

3. Before starting to print the final product the 3D printer needs calibration of the printing parameters in order to produce parts without flaws and defects efficiently; the variability of the parameters depends on the specific material and on the machine itself. The two most important parameters when dealing with 3D printing are temperature and speed. The temperature of the extruder should be sufficiently above the melting point of the thermoplastics to obtain a flow of material that can be arranged in the desired shape. At the same time the speed should be low enough to capture the details of the models without defects efficiently with respect to the total printing time. Moreover, if the extruder is too slow and the temperature is too low the layers of material could not bind efficiently because the material has already solidified. For this reason, as preparation to the printing of the Negative Stiffness Honeycomb models, a test called *Temperature Tower* was performed. As can be seen in fig. 2.20 a complex design is repeatedly printed in a tower configuration, starting from the maximum declared temperature of the manufacturer, decreasing progressively the temperature. It was found that the temperature of $265°C$ was the sweet spot to have a good printing quality, while under $250°C$ the printing was unsuccessful.

Figure 2.20: Temperature tower used for the calibration of printing temperature

Regarding the speed, It was chosen to move the printer head at an average velocity of 50 $\frac{mm}{s}$ (relatively low to what can be found for other materials and applications) avoiding to introduce excessive stress, which could trigger the onset of the already discussed phenomenon of warping, but still producing prototypes in relative short time, never more than 5 hours. More information about the specific printing parameters can be found in Appendix 6.2

4. The STL file is sliced into parallel horizontal layers using software Cura by Ultimaker ®, representing the input motion to the extruder head during printing to obtain the final result.

5. The machine used to print the prototypes is the Delta 2040 Industrial X by *Wasp* ®.

2.3.2 Laser cutting

Although It is possible to use additive manufacturing technology for stepping up to more performing metal negative stiffness honeycombs parts, they are much more expensive with respect to subtractive technologies, even considering the cost of the waste material.

Hence, for the production of the final metal prototype It has been chosen Laser cutting as a method, which consists in using the redirected concentrated energy arising from the chemical excitation of a gas to heat and vaporize the metal. With respect to other types of subtractive technology It allows to have precise edges and surface finish without any post processing; moreover the machines usually use a motion control system which automatically cuts even complicated shapes, like the one of Negative Stiffness Honeycomb. A schematic of the laser cutting process is reported in fig. 2.21.

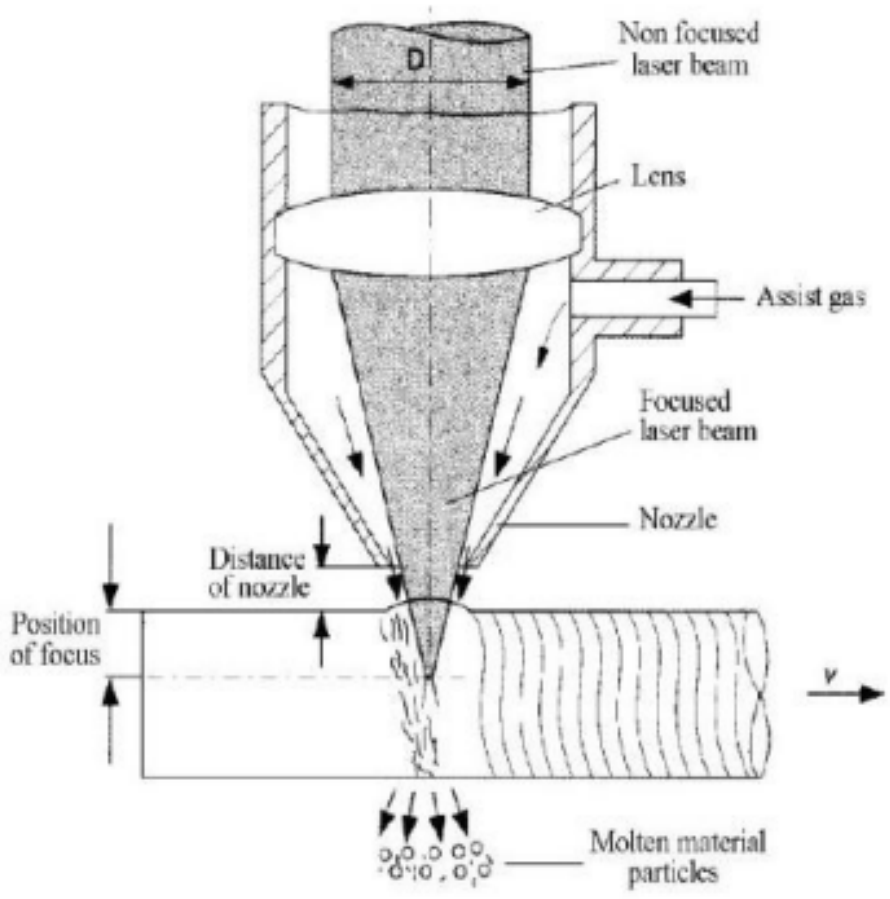

Figure 2.21: Schematic of the working principles and components of laser cutting [30][31]

However, due to the relatively small thickness of the beams(intended as the geometrical parameter t, referring to fig. 1.4) , it was necessary to cut the negative stiffness honeycomb modules from a thinner sheet of metal with respect to Nylon prototypes. In fact, the high level of heat generated by the cutting process creates a Heat Affected Zone (HAZ), a non-melted area of material that which undergone substantial changes in mechanical properties, summarized in fig. 2.22, due to the high temperature level reached. The dimensions of the beams were not sufficient to dissipate the heat produced by a cut on a thick metal plate, hence it was necessary to reduce the thickness of the sheets from 10 mm to 5 mm, thus reducing the heat generated in the process. The plates were then fixed together to reach satisfactory width to avoid instabilities during compression.

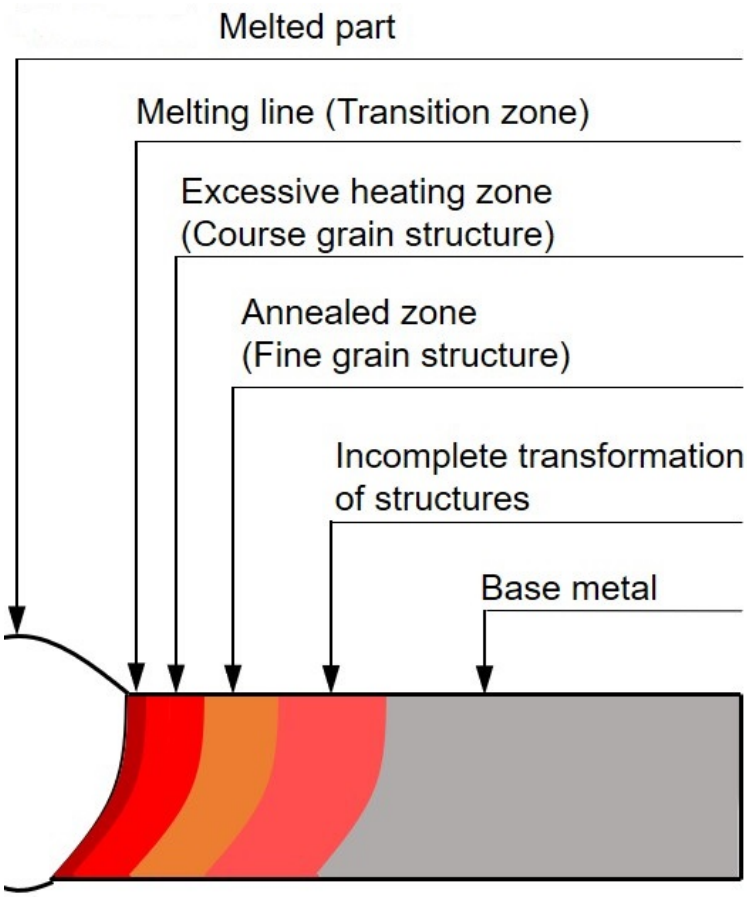

Figure 2.22: Scheme of the defects inside the Heat Affected Zone

2.4 Testing equipment

Two types of test were conducted on the model produced in this thesis work.

The first one was a repeated compression at low constant speed (typically 5 $\frac{mm}{s}$), performed to capture precisely the loading and unloading curves of the negative stiffness honeycomb cells. The test was conducted with the machine MTS ®370.10 with an available actuator rating of 100 KN and stroke of 250mm, equipped with Load Cell MTS® 661 with a sensitivity of 2 $\frac{mV}{V}$. The same machine was used to characterize the 3d printed Nylon material with tensile tests using MTS®634.12F-2X as estensometer for measuring the strain with a travel of 12.5 mm (+50%) on a gage length of 25 mm ($\pm 0.05mm$)

On the most promising models was performed a dynamic test on the vertical sled, showed in fig. 2.23 In this scenario a mass is released from a prescribed height in free fall on the energy absorbing device positioned underneath it. Two vertical cylindrical pillars are used as roller guides for the mass in order to avoid disalignement during the fall, which could bring to an uneven failure of the absorber and a not valid test. The acceleration data are measured with EGCS-S425-250 sensor by *Measurement Specialties* ®, with a range of 250 g a sensitivity of 0.503 $\frac{mV}{g}$ and an acquisition frequency of 10 kHz.

Figure 2.23: Vertical sled used to perform dynamic compression tests

The 3d printed nylon prototypes were mainly subjected to static compression, because of the high repeatability of the recovery and the need for high precision measurements to successfully capture the negative stiffness behaviour. Instead the final metal prototype was only tested with repeated dynamic compression, because of the limited reusability of the absorber.

2.5 Prototypes: structure and main features

The multi-step experimental process led to the realization of three different prototypes which represent the dynamic evolution of the work from the theoretical concept to a progressively more efficient concrete product. The three models presented in the following section were developed in series as a result of a critical evaluation of the performances of each prototype and with the goal to improve stepwise their functionality maximizing the prototype efficiency. For clarity reasons the structure and main features of three iteration models will be presented in separate section although representing a continuum in the experimental workflow.

2.5.1 First Iteration Model

The first step in the developing of a functional absorber exploiting negative stiffness was experimenting the recoverability of the design with a bidimensional concept, similar to the one proposed by *Correa et al.* [22], with cells arranged in a 2x2 pattern (two adjacent cells for two rows). One horizontal beam in the middle creates an additional constrain that avoid excessive horizontal expansion of the model during compression.

Two different geometries were tested, both had the same apex height and thickness, however there is a 10 mm difference in the length of the beams. The geometrical parameters of the cells are reported in the following drawings 2.24 and pictures 2.25; they are denominated *L65 2D* and *L55 2D* referring to their characteristic length

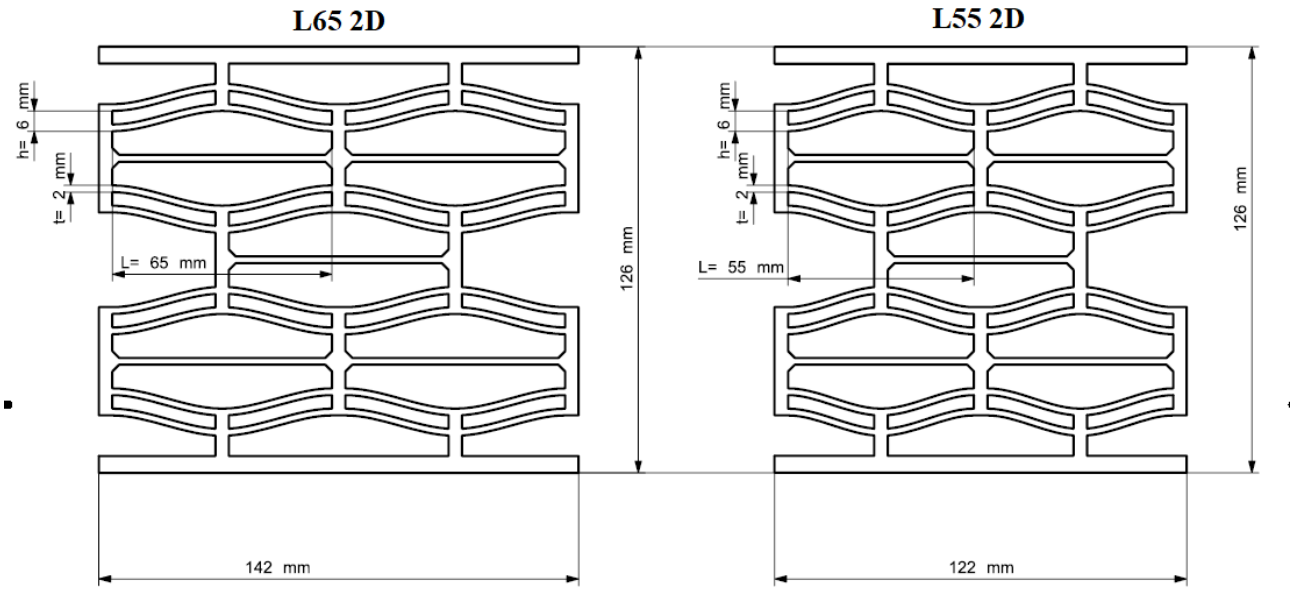

Figure 2.24: Drafts of the two iterations of the First model with characteristic dimensions

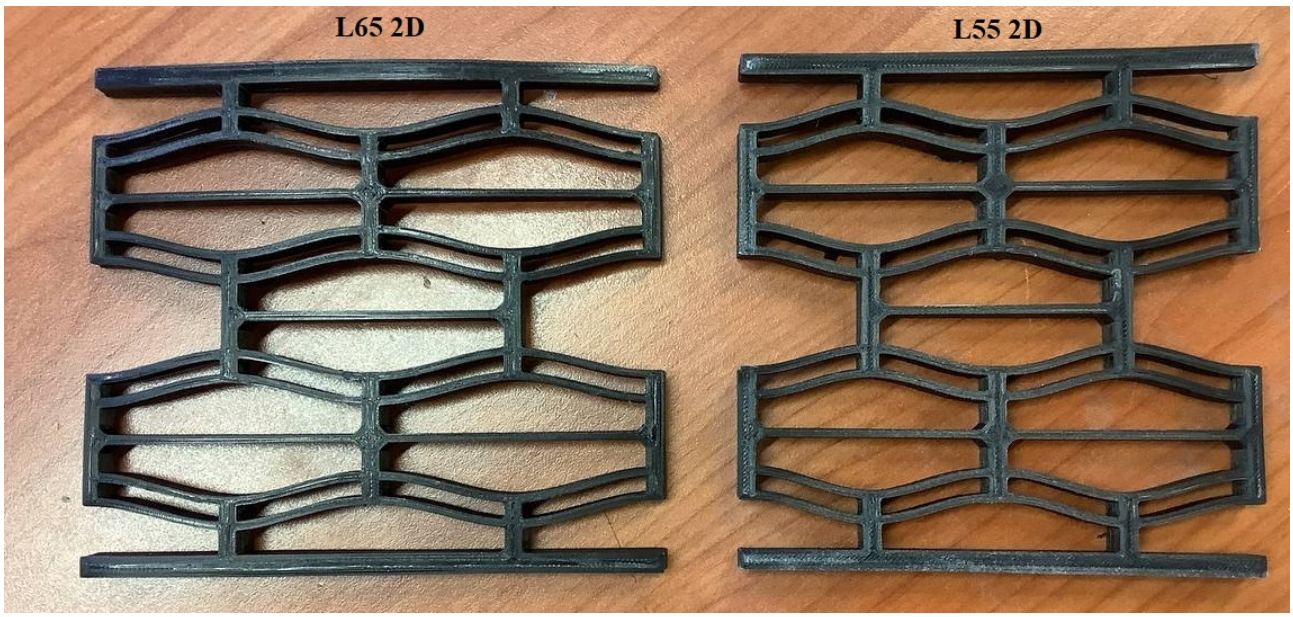

Figure 2.25: Comparison of the 3d printed iterations of the first model

The bistability ratio results to be equal to $Q = 3$; from the theory explained in chap. 2.1.1, it should have been sufficient to have a bistable behaviour during compression.

The model was tested only with static compression test because the bidimensional design was considered highly prone to instability and not reliable for a dynamic impact test; in fact in figure 2.26 it is possible to notice an out-of-plane deformation in some static compression test, verified also with numerical simulations, if the displacement goes beyond the maximum value given by the curvature of the curved beam and the structure reaches densification, with the beams in contact with each other.

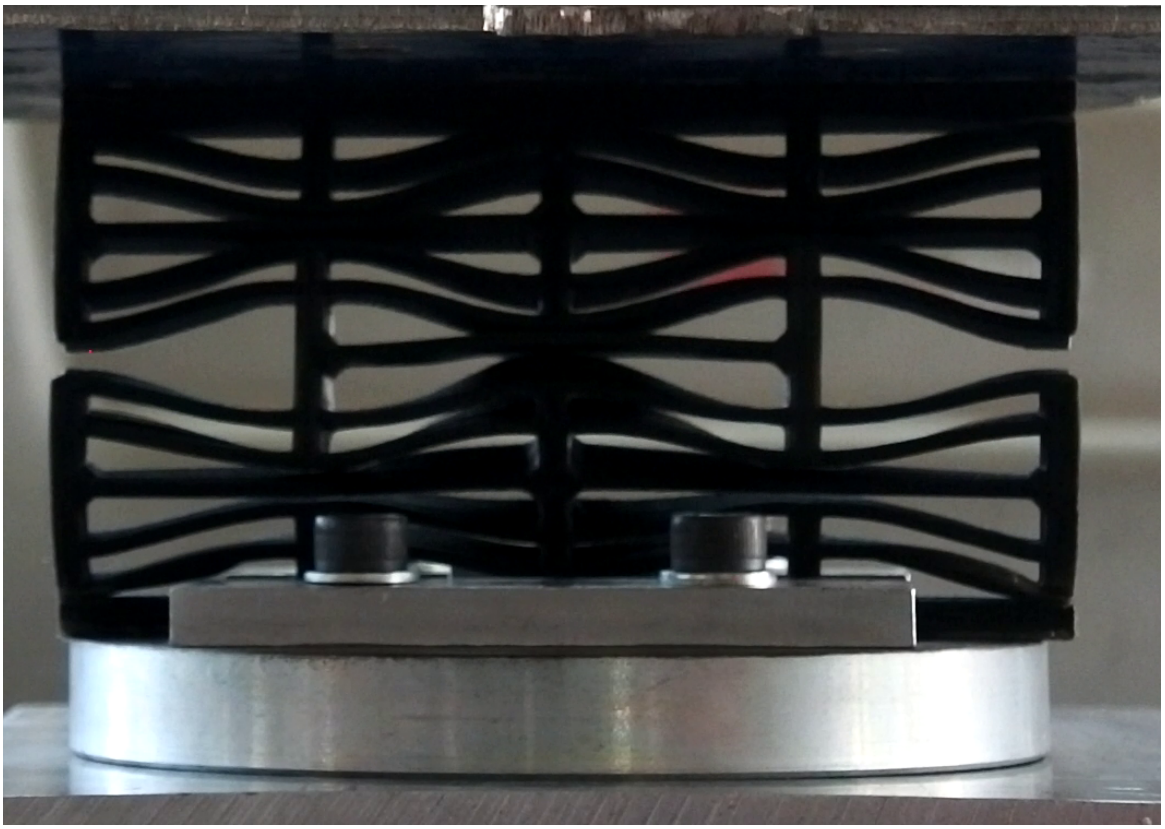

Figure 2.26: Highligth of out-of-plane instability phenomenon during static compression of bidimensional prototype

2.5.2 Second Iteration Model

The model was designed with the following performance and functional requirements:

- An increased energy asborbed and specific energy per unit of mass
- High bistability ratio: from the analytical computation a value of Q greater than 2.31 is sufficient to ensure a deformed equilibrium position of the double curved beam. However, as already been explained before (chap.2.2.1) inside an honeycomb configuration the behaviour results inhibited by the horizontal expansion of the extremities of the cell. For the purpose of energy absorption a bistable behaviour would be preferred with respect to a monostable behaviour, because the energy is not transmitted to the impacting body, which could become dangerous for the surrounding environment. Moreover, the mechanical properties of the 3D printed product are substantially different with respect to a solid model used in the analytical formulation, for the different homogeneity, the anisotropy and non linear behaviour of the material
- The technology and the material were maintained since they were considered simple, effective and with an high value of elasticity.
- The need to contrast the instability due to the low depth of the beams and the warping caused by inefficient printing of Nylon, in order to improve the usability in a dynamic crash event
- Include the possibility to expand the total dimension of the absorber in order to meet an higher performance goal

For these reasons the geometry is designed with a value of Q much higher with respect to the limit value for bistability and to the first model, with the aim of retarding the snap-back of the curved beam after the unloading and enhancing the negative stiffness behaviour. The value of the thickness of the beams was kept constant, with a lower boundary given by the extrusion width and a minimum number of walls of the curved beam (intended as parallel filament extruded inside the slender curved beams) and an upper boundary given by the constraint of build volume on the consequent increase of length (as shown before in graph. 2.5 Hence, the value of apex height was increased to $h = 10mm$, for a bistability ratio (Q) of 5.

The length of the beam was chosen starting from the desired maximum deformation of the material as given by formula (1.5). However, due to the complex failure behaviour of the 3D printed part a target deformation value was very difficult to be set, because it did not depend only on the yield point of the material during tensile test ($\epsilon_{yield} = 2\%$), but also on the interlayer and intralayer adhesion properties and shear stresses between the lamina.

With $\epsilon_m = 11\%$ (which corresponded to a length of 60 mm) the NS cells under compression presented a pronounced wall delamination along the curved beams, as showed in fig.2.27a. Increasing the length dimension to 70 mm (with a maximum deformation computed of 8%) produced honeycomb cells which exhibit slight fractures near the edges and an irregular deformation of the curved beams(fig.2.27b) Finally, a value of length of the beam of 80 mm (2.27c), for a resulting deformation value of 6.2%, allowed to obtain a reliable behaviour during deformation of the honeycomb cell, without defects even after several compression events. Hence, this last design has been chosen for the use in the prototype.

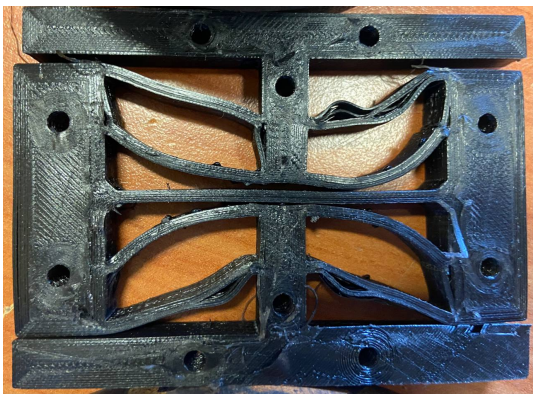

(a) Deformation of cell with L= 60 mm

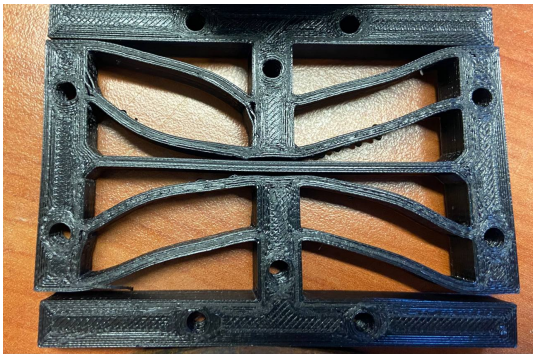

(b) Deformation of cell with L= 70 mm

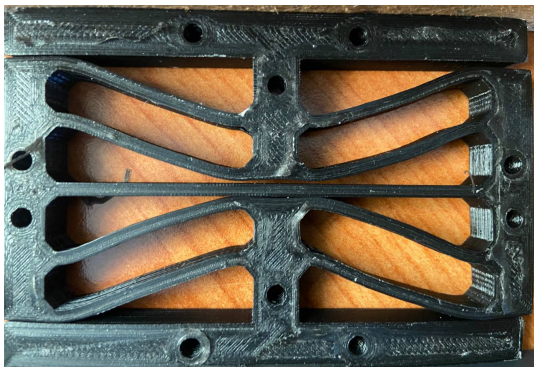

(c) Deformation of cell with L= 80 mm

Figure 2.27: Deformation of different attempts to Negative Stiffness honeycomb cells varying the characteristic length

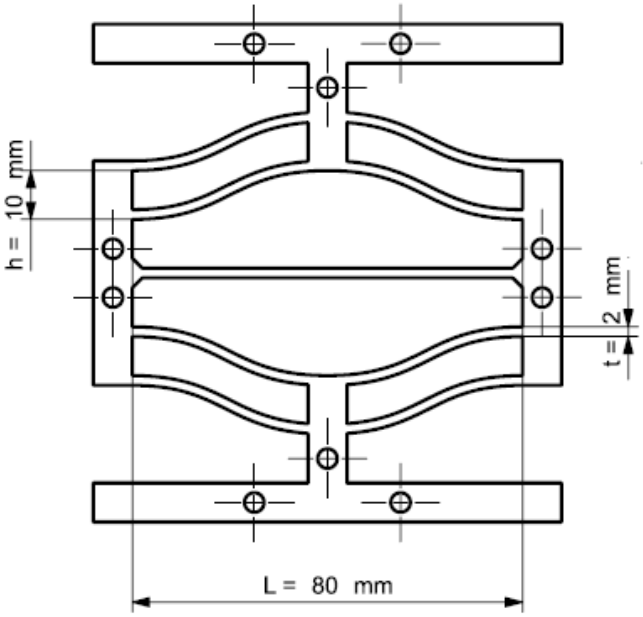

Figure 2.28: Characteristic Dimensions of the Negative stiffness honeycomb cell used in the second Model

One main feature of the second model was the *modular design*.

In fact, for the production of the protoptype the single cells were 3d printed and then assembled in a three dimensional configuration by crossing at the extremities of the cell in order to counteract the insurgence of transversal buckling and to stabilize the behaviour of the cell during deformation, as well as allowing the device to stand still with a solid base. The addition of holes on vertical, top and base beams, for a total of 10 for each cell in a symmetric design, combined with 8 planar inserts (fig2.29a) and 2 cross shaped links (fig2.29b) (also produced with 3d printing) makes possible to easily stack and interlock the NS honeycomb cells with bolts and nuts, as showed in exploded view in fig.2.30. The design opens the possibility to scale up the model adding more and more modules with connection parts making it viable for a broad range of applications with respect to the performance requirements.

As explained numerically in chap. 2.2.1 the stacking of cells one on top of the other in series configuration contributes to increase the stroke of the device and, thus the energy absorbing capabilities. On the other hand, the parallel configuration increases the total force threshold, as well as ensuring a stronger boundary condition for the central beam, shared by the two adjacent cells, bringing to an increased bistability behaviour.

In fig. 2.31 is pictured the prototype of the second iteration model, which would also be addressed as *Modular L80* due to its min feature and characteristic cell length.

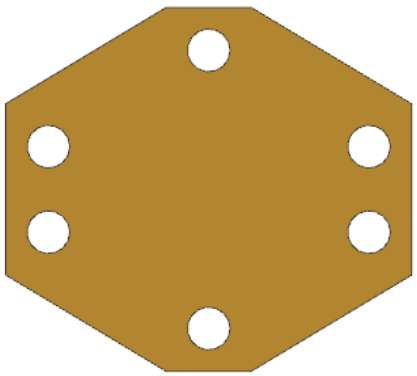

(a) Planar insert connecting cells in series

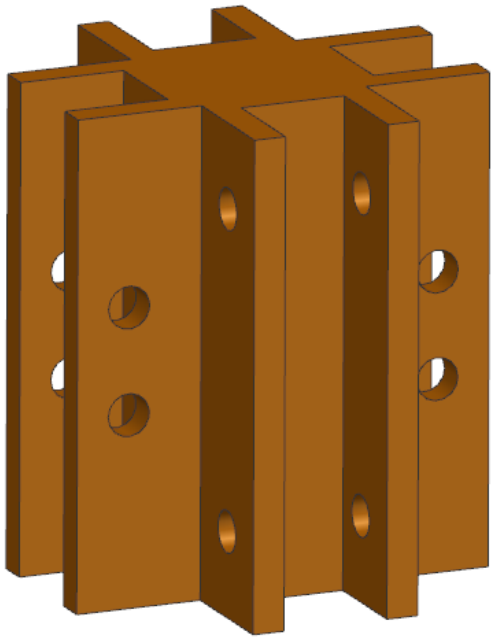

(b) Cross insert connecting cells in parallel angled by 90°

Figure 2.29: Inserts used to connect Negative Stiffness honeycomb modules in the second model

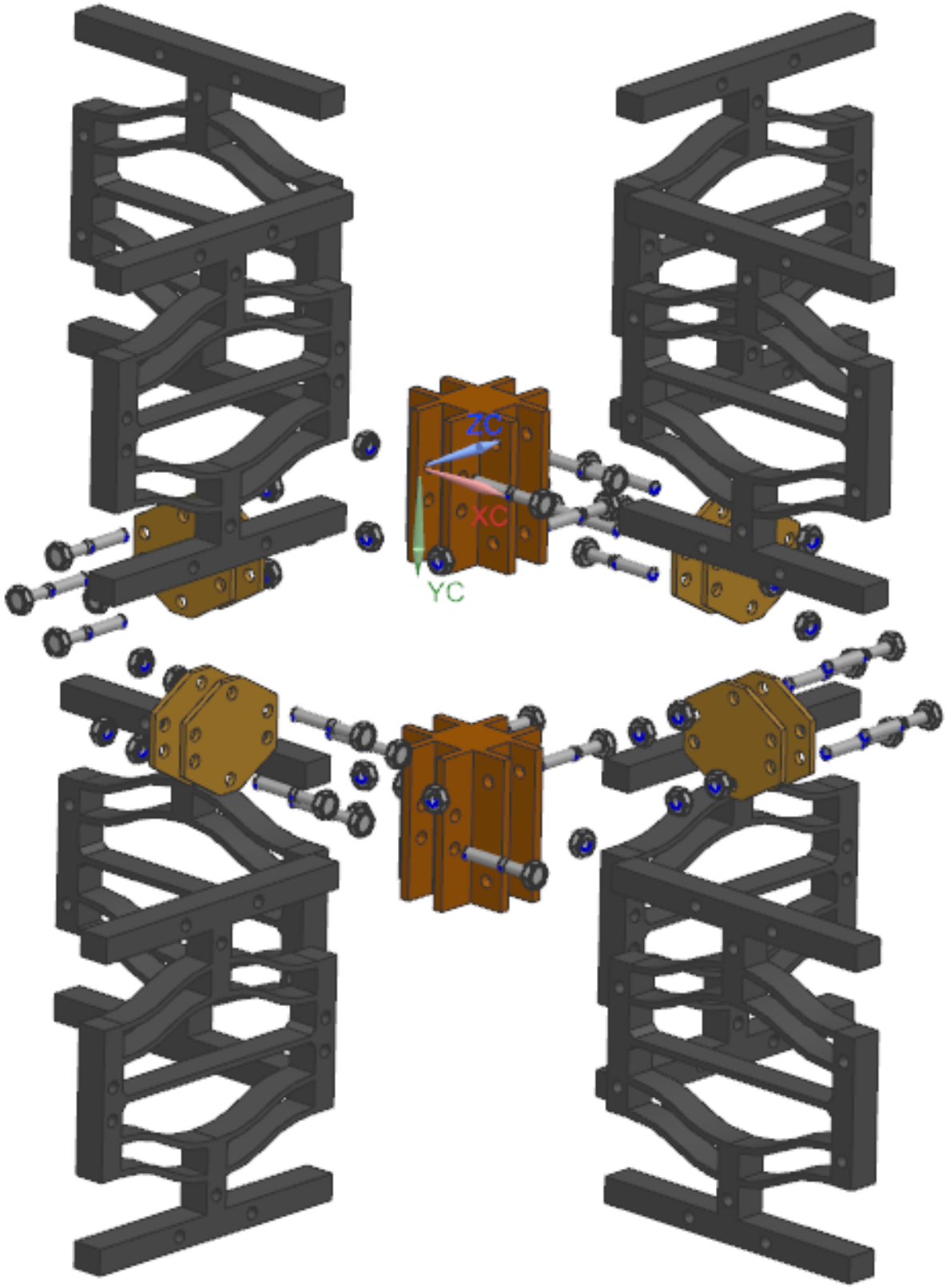

Figure 2.30: Exploded view of the second model assembly

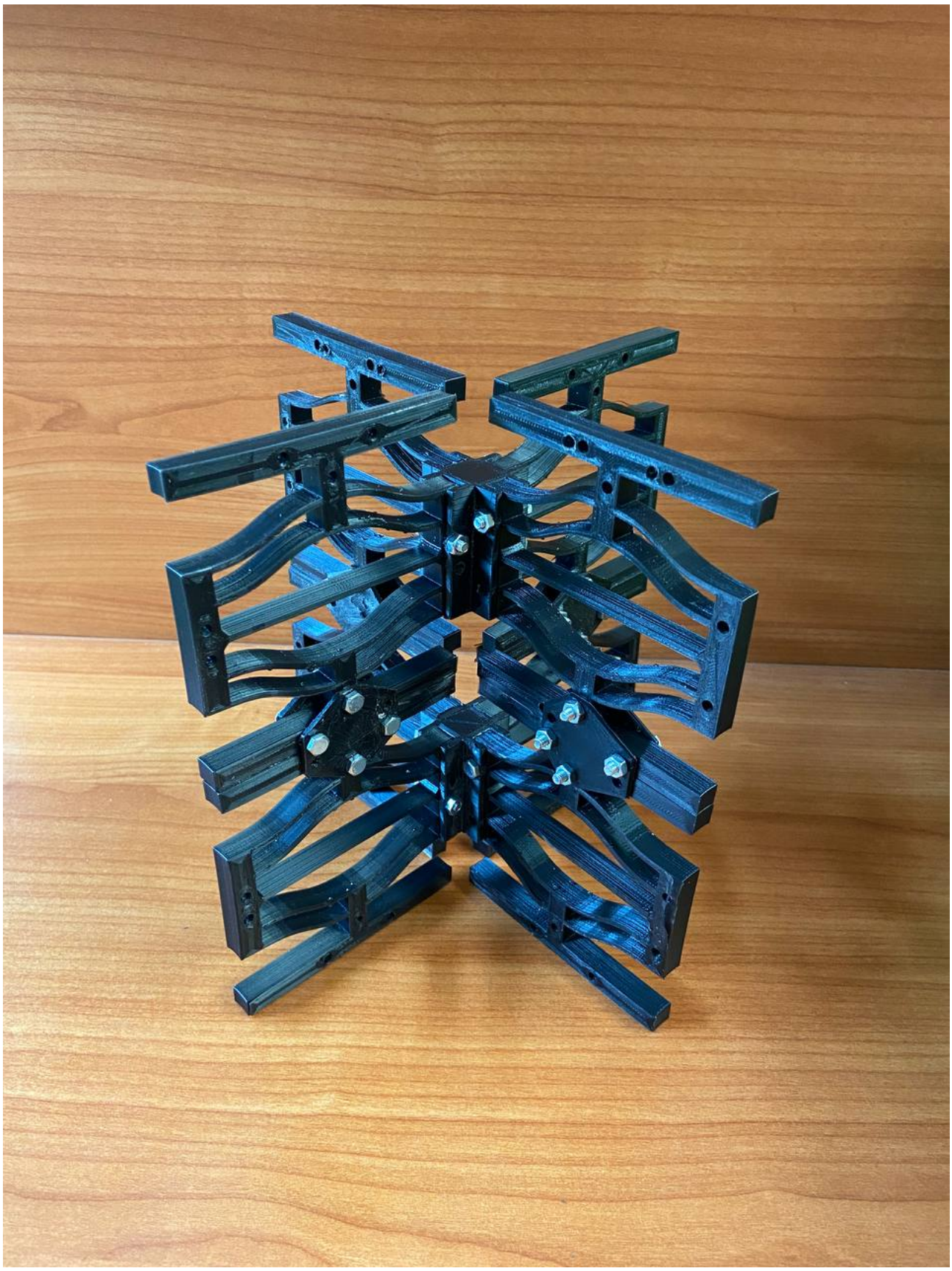

Figure 2.31: Picture of the assembled second iteration prototype

2.5.3 Third Iteration model

The third model was intended to explore the highest potentiality of the negative stiffness honeycomb in terms of performance by using the superior mechanical properties of Metal.

In fact it has been used as a base material Stainless Steel AISI 304, with an elastic modulus of 200000 Mpa and a yield stress of 210 Mpa, which are hundreds of times greater with respect to the thermoplastics used in 3d printing, referring to chap. 2.3.1

One limitation of metals consists in the low level of Yield deformation, which, for the steel is calculated to be equal to 0.2%, from the data above. Hence,except with extreme and not convenient cells geometries, the mechanism of energy absorption would not rely totally on elastic recovery, but there would be also an energy dissipation through plastic deformation.

On one hand this mechanism allows for a safer and more effective absorber: the energy of the impact would not be transmitted back to the impacting body and the negative stiffness beams remain deformed in *Snap-through* configuration after a collision.

However, this will need an active method to recovery the functionality of the absorber by traction after the compressive impact; with further developments the recoverability could also be incorporated into the devices thanks to hydraulic pistons or other methods.

Moreover the reusability of the absorber will be limited by the level of failure strain of the material with respect to the maximum deformation registered during the buckling transition of the cells. At each compression event the material undercomes an hardening process, its yielding point will increase and its range of deformation will decrease, until the rupture.

For these reasons, the cell geometry was designed following eq. (1.5) in order to have a maximum level of deofrmation of 2%.

Fig. 2.32 represents a drawing of the steel negative stiffness honeycomb modules (with associated characteristic dimensions) while in fig. 2.33 are shown the corresponding pieces separately before the assembly of the structure.

Each module is composed of 2 cells, instead of one, for a easier assembly, avoiding planar inserts of the second iteration model, used for stacking cells.

With respect to the cell dimensions of Nylon 3d printed prototype highlithed in fig. 2.28, the apex height has been decreased from 10 mm to 8 mm; considering a constant thickness of 2 mm, limited by manufacturing constraints already explained, these dimensions will bring to a bistability ratio of 4, that ensures a high level of energy absorption and a controlled behaviour during compression and recovery. Consequently, the length of the beam was increased from 80 mm to 130 mm, with an inevitable loss of performance, as reported in chap 2.1.1.

The bidimensional modules were interlocked using cross-shaped inserts like the second model, however in this case they were machined from iron to increase strength of the connection and precision of the fitting.

In fig. 2.34 is pictured the final assembled model, that will be denominated *L130 steel*, given its characteristic length and material.

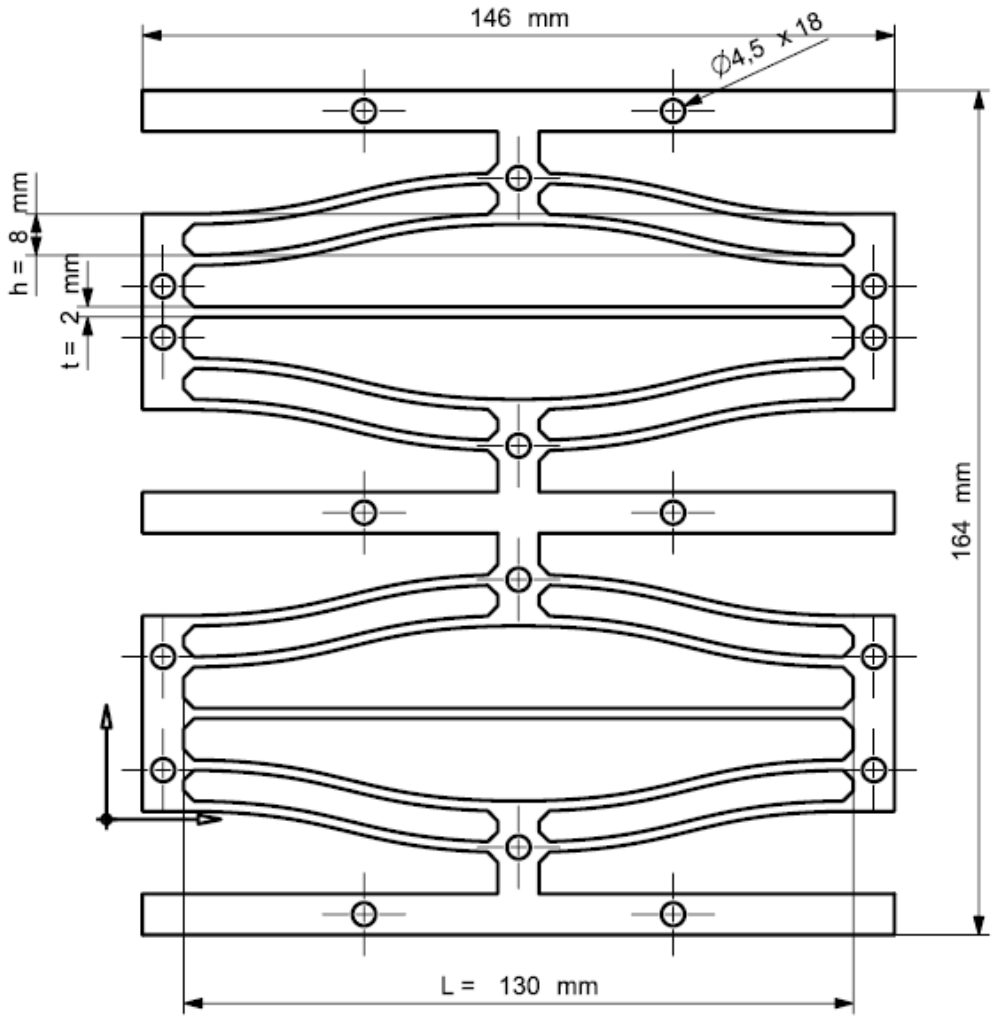

Figure 2.32: Drawing of third iteration Model Negative stiffness Honeycomb modules

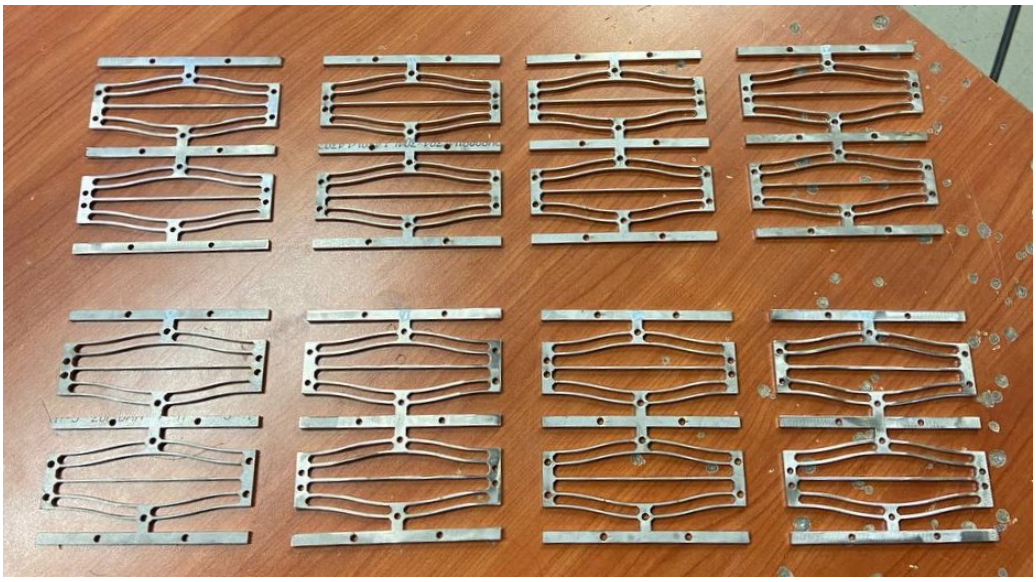

Figure 2.33: Picture of the Negative Stiffness Honeycomb third iteration modules before assembly

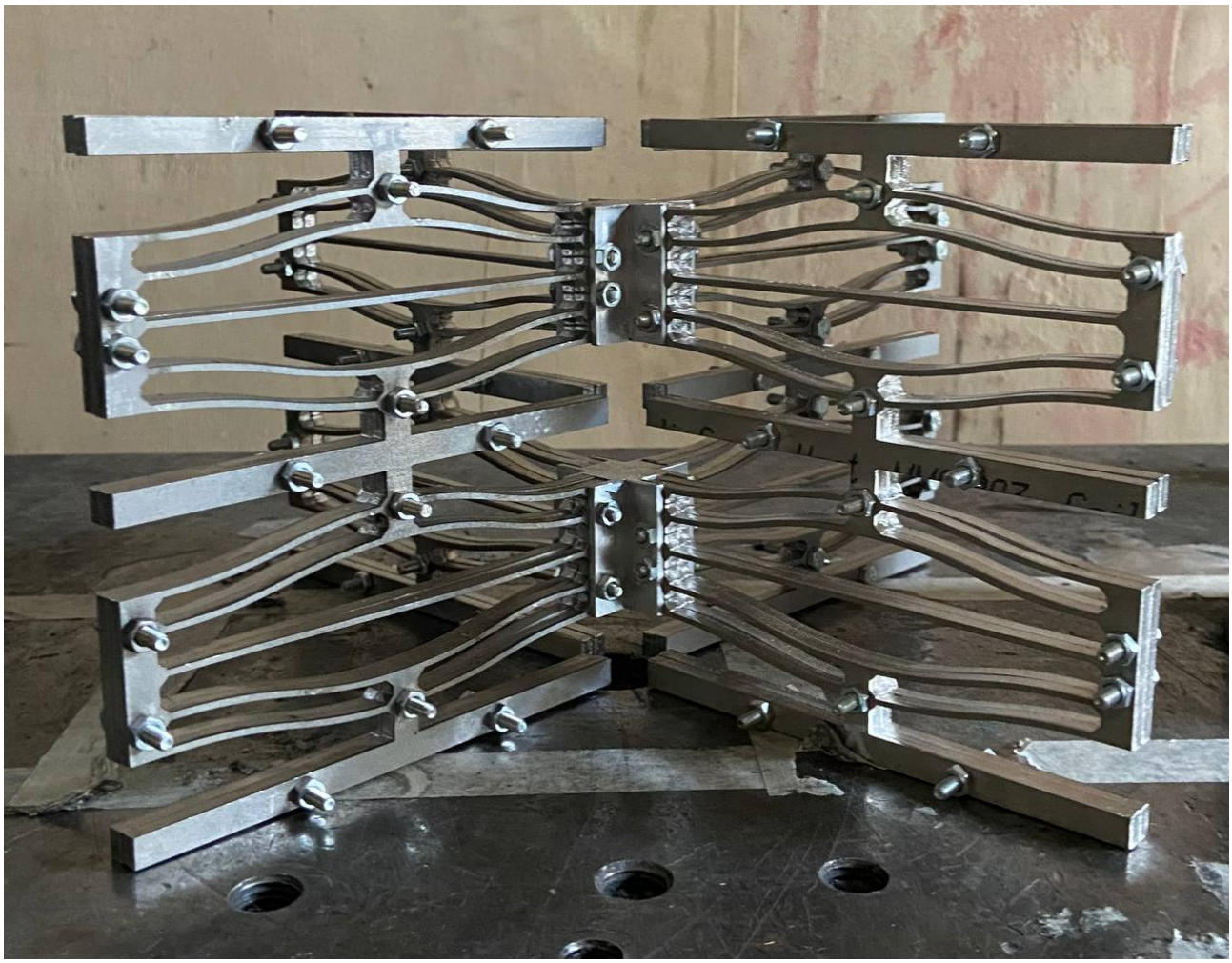

Figure 2.34: Picture of the assembled third iteration model

Chapter 3

Results

3.1 First Iteration Model

For each model two consequent static compression tests were performed on the same specimens. In fig. 3.1 are reported the corresponding load-displacement graphs (shades of blue for the tests on the model *L65 2D* and shades of red for the one on model *L55 2D*).

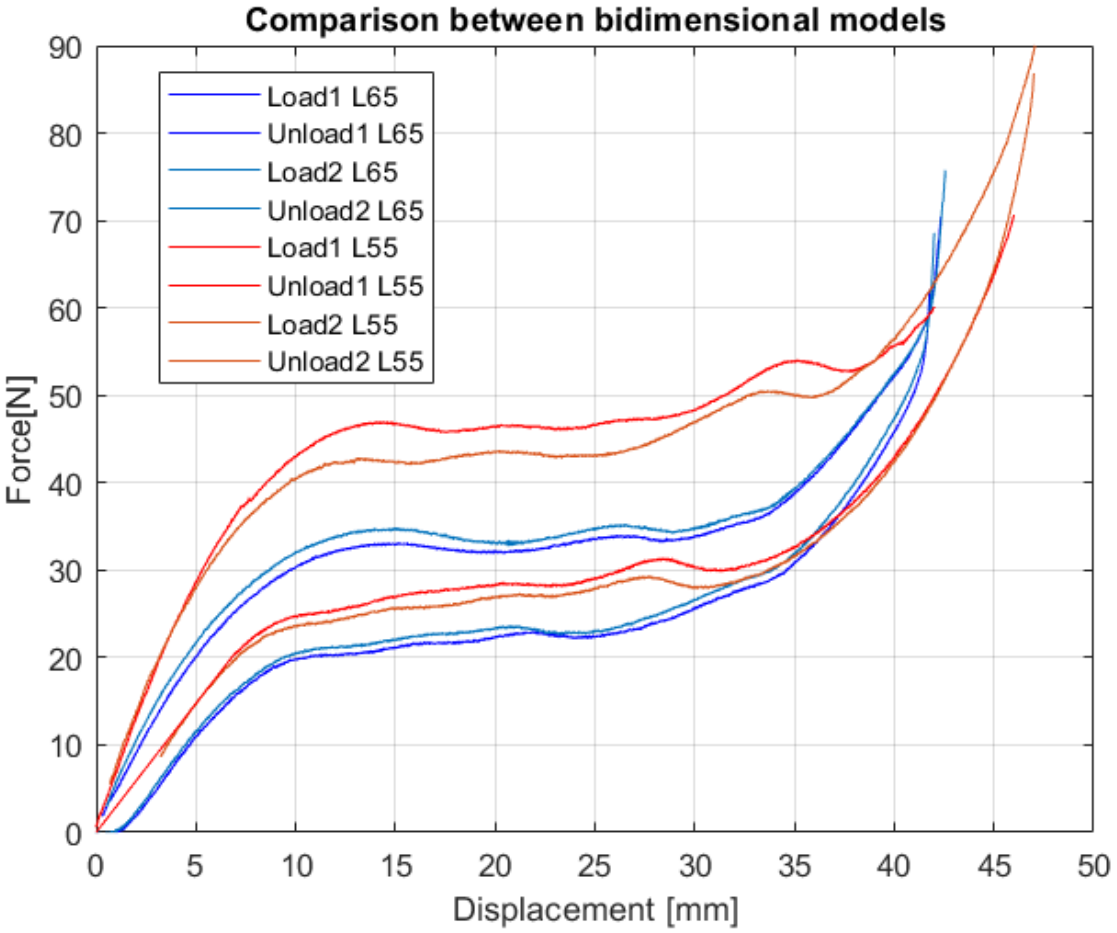

Figure 3.1: Experimental data of the two bidimensional models in consecutive tests

The bidimensional model prove the concept of Negative stiffness honeycomb for a recoverable energy absorber, infact, the curves of consequent tests result almost superimposable and in fig. 3.8 it is shown the complete recovery of the deformation after the compression.

Moreover, it is interesting to notice an hysteresis behaviour in the unloading curve with respect to the loading curve, (as already found in other literature studies [9] [18] and remarked in chap. 1.4.1) with a force threshold during unloading approximately 40 % lower than the plateau of the loading curve, as a prove that negative stiffness honeycomb can be used to dissipate compression energy, favouring the safety of an energy absorbing device in the event of a collision.

The two different results in loading curves of the two bidimensional 3d printed models show the importance of the geometrical parameters in the design of the cells. As shown by the analytical formula (2.14) the peak force of the bistable curved beams during buckling is inversely proportional to the third power of the length. In fact, there is a substantial difference in performance parameters between the two absorbers, which is summarized in the table 3.1. The registered magnitude of the force plateau for the model with characteristic dimension $L = 65\ mm$ is of 32 N, while the model with $L = 55\ mm$ reaches a force threshold of 44 N, with an increase in performance of 38 %. The effect of the change in dimensions results amplified in the measure of energy absorption, with an increase of 58 % in the performance of the two absorbers. In the table 3.1 the Energy absorbed is defined as the area subtended by the loading curve, while the Energy dissipated is the area included between loading and unloading curve.

Characteristic length [mm]	Peak force [N]	Energy absorbed [J]	Energy dissipated [J]
65	32	1.38	0.42
55	44	2.18	0.78

Table 3.1: Comparison of performance parameters of bidimensional models of different length based on experimental tests

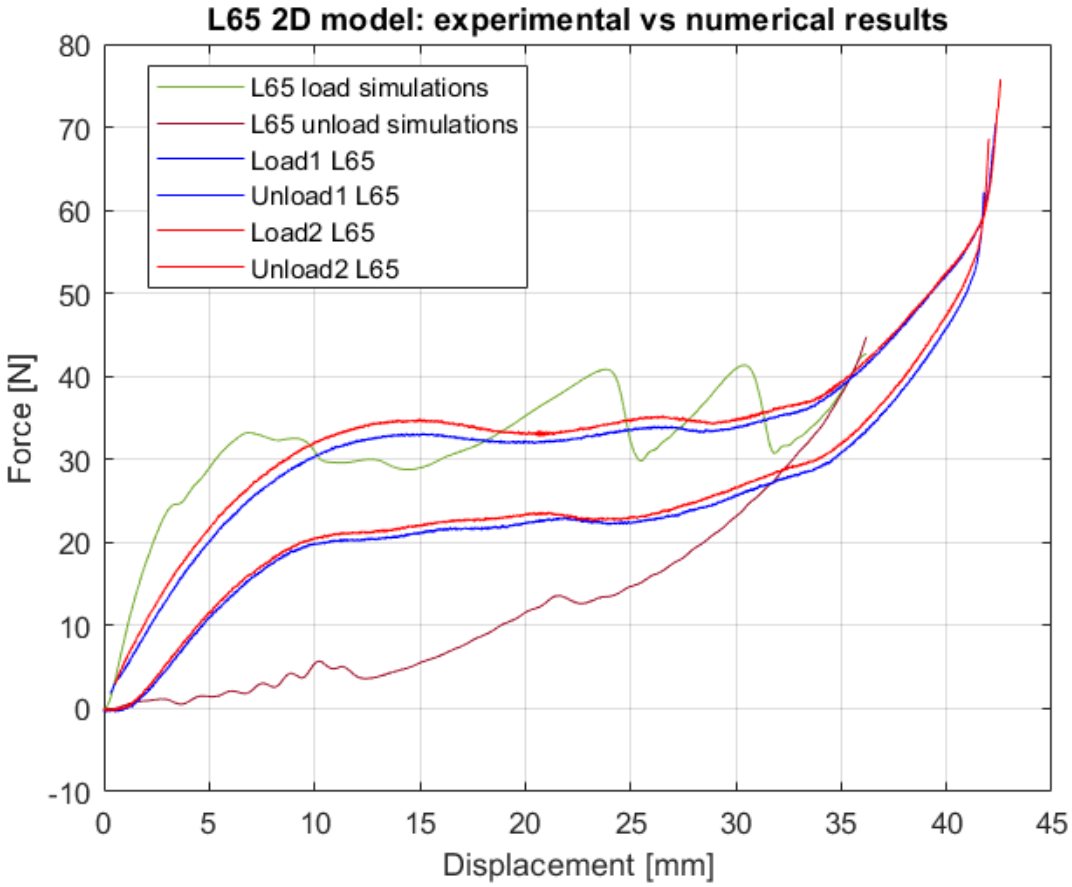

Figure 3.2: Comparison between experimental data and numerical simulations for $L65\ 2D$ model

In fig. 3.2 are reported the results of numerical simulations conducted on the *L65 2D* model.

The data of the numerical simulations resemble quite accurately the test data with a maximum deviation in the plateau region of 17%. The main difference, however, is observed in the first elastic region where the numerical model show a modulus of 6.58 $\frac{N}{mm}$, 58% more with respect to the test data. This difference can be attributed to the large variability of material characteristics and porosity among the real model given by the manufacturing method and the important warping occurred during production. Moreover, the material has been characterized only in tensile stress in the direction of the extruded fibers, which resemble the behaviour of the curved beams, but the rest of the structure has been produced with 45° infill at 30 % of density. Hence the prevision of the initial stiffness of the structure is affected negatively in comparison to the data; however this error does not impact negatively the measure of the compression energy absorbed by the structure, since the plateau region is the one which has a higher influence in terms of energy absorbed due to the high value of displacement at an almost constant force threshold, equivalent to the maximum one.

Furthermore, the numerical simulations reports an immediate recovery of the deformation upon unloading of the cells, like the experiments. However, the predicted force-displacement data during the unloading phase are not really representative of the real behaviour of the test, as can be seen in fig.3.2. This discrepancy is due to the simplified modeling of the material. In the simulation the unloading phase of the material is assumed to be linear following the same slope of the Young Modulus; however, some experimental studies in literature [32], [33], [34] show that thermoplastics are characterized by a complex non linear hysteresis behaviour in cyclic loading like fig.3.3 and that a most commonly used elasto-plastic model shows to highly underestimate the intensity of the recovery of the deformation during the unloading phase. A much more accurate material testing campaign must be carried on to have a plausible description of the unloading phase of the material, however this is beyond the purpose of this thesis work.

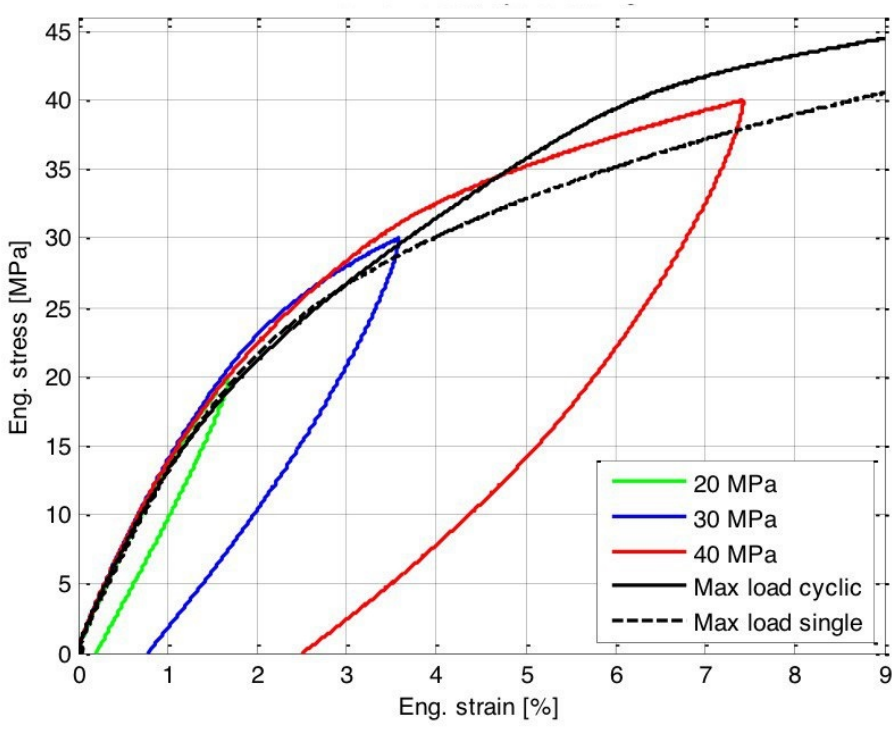

Figure 3.3: Cyclic stress-strain curves for non reinforced thermoplastics [32]

In fig. 3.8 is analyzed the deformation pattern of the model, with the sequence of snap-through and snap back phenomena. However, the intensity of this phenomena is much lower with respect to what expected from the theory on buckled curved beam presented in chap 2.1.1 and also compared to numerical simulations. In fact, the experimental data (fig. 3.1) do not underline a negative stiffness behaviour, intended as pronounced negative slope portions in the force-displacement curve, with only small oscillations.

One possible cause of the dampening of these oscillations is the lack of viscous properties in the numerical modeling of the material, favouring a quick description of the general behaviour of the structure mechanical response.

These data justify the affirmation previously reported in chap 2.2.1: the behaviour of the honeycomb configuration is much more complicated with respect to the bistable beams, which are still to be considered a viable design tool for parametric analysis. As a result the negative stiffness behaviour is influenced also by the rigidity of the boundaries of the curved beams, both in terms of horizontal expansion and material properties and a much higher bistability ratio is necessary to highlight the negative stiffness behaviour. This aspect is very important because a structure with reduced negative stiffness behaviour tends to act more like a spring transferring to the impacting body most of the energy of the collision, while an enhanced negative stiffness delays the recovery of the deformation, thus increasing the safety.

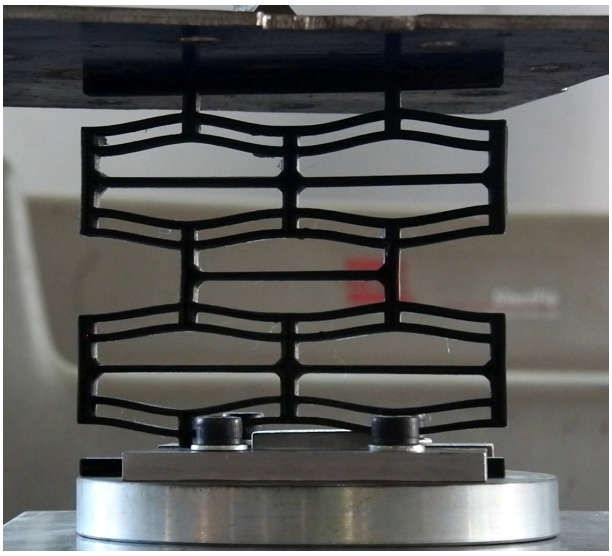

(a) Stage I - Compression start

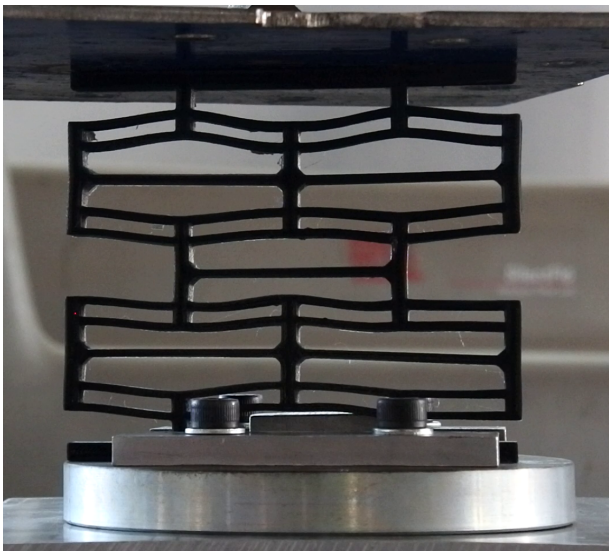

(b) Stage II - First Snap-through event

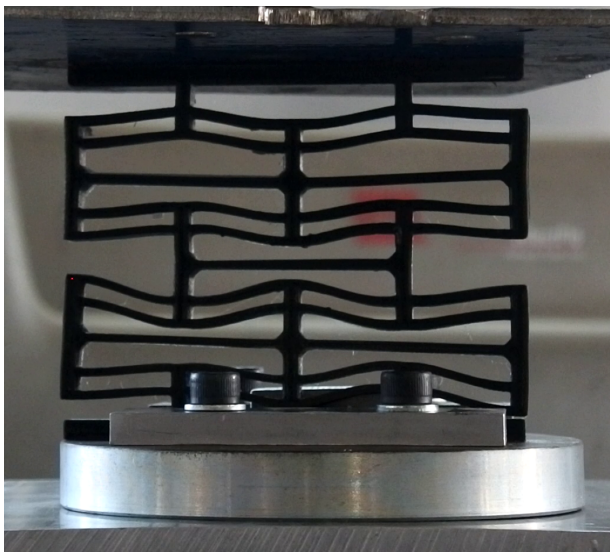

(c) Stage III - Second Snap-Through event

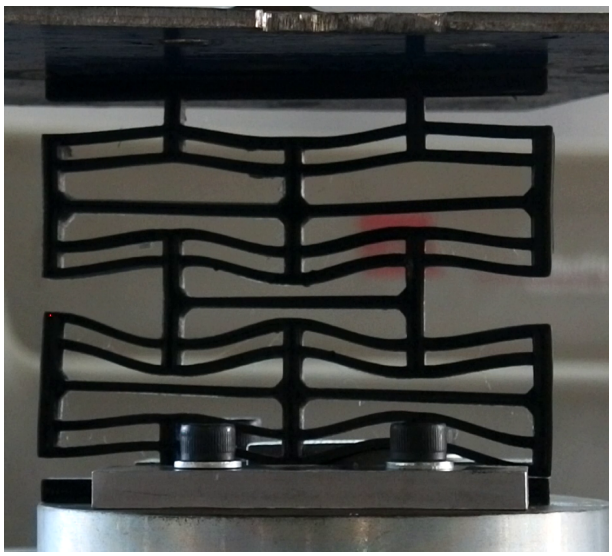

(d) Stage IV - Third Snap-Through event

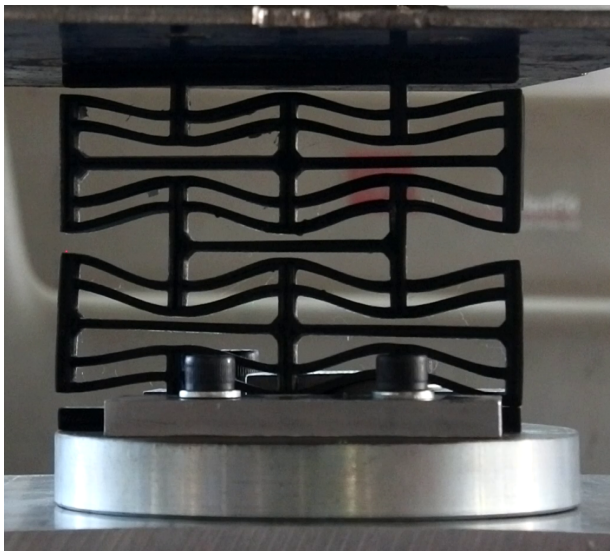

(e) Stage V - Full densification

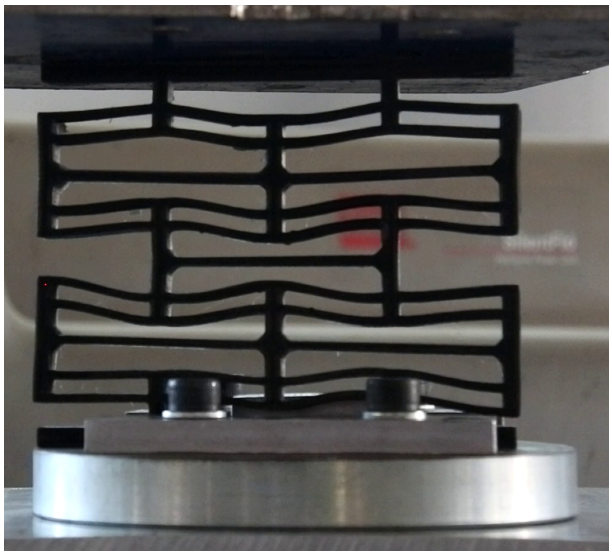

(f) Stage VI - Firs Snap-back event

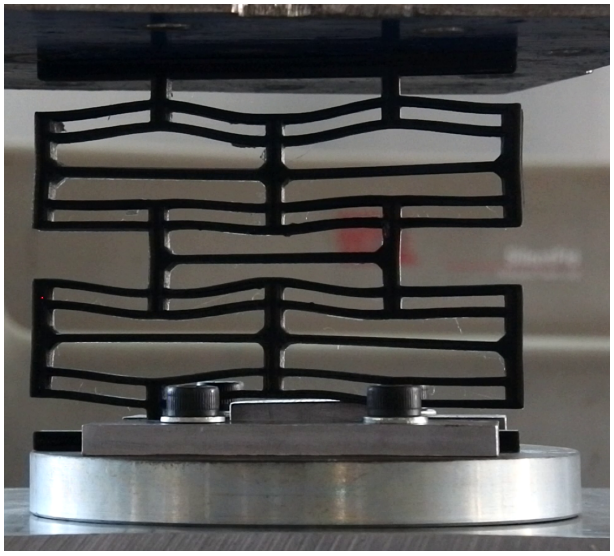

(g) Stage VII - Second Snap-back event

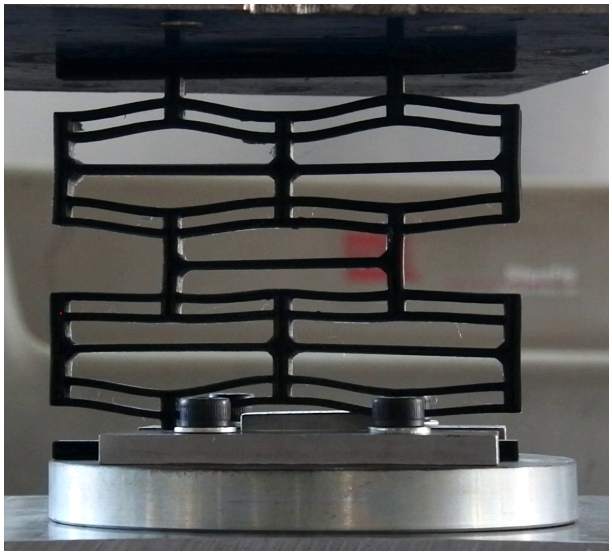

(h) Stage VIII - Third Snap-back event

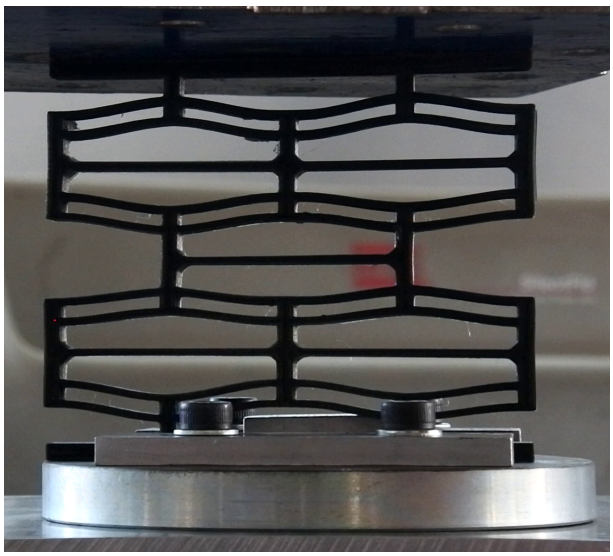

(i) Stage IX - Full recovery

Figure 3.8: Deformation stages of first model during static compression test

3.2 Second Iteration Model

3.2.1 Static compression

In fig 3.9 are shown the results of static compression test on the 3d printed prototype of the second iteration model. The test were performed on the same specimen subjected to dynamic testing.

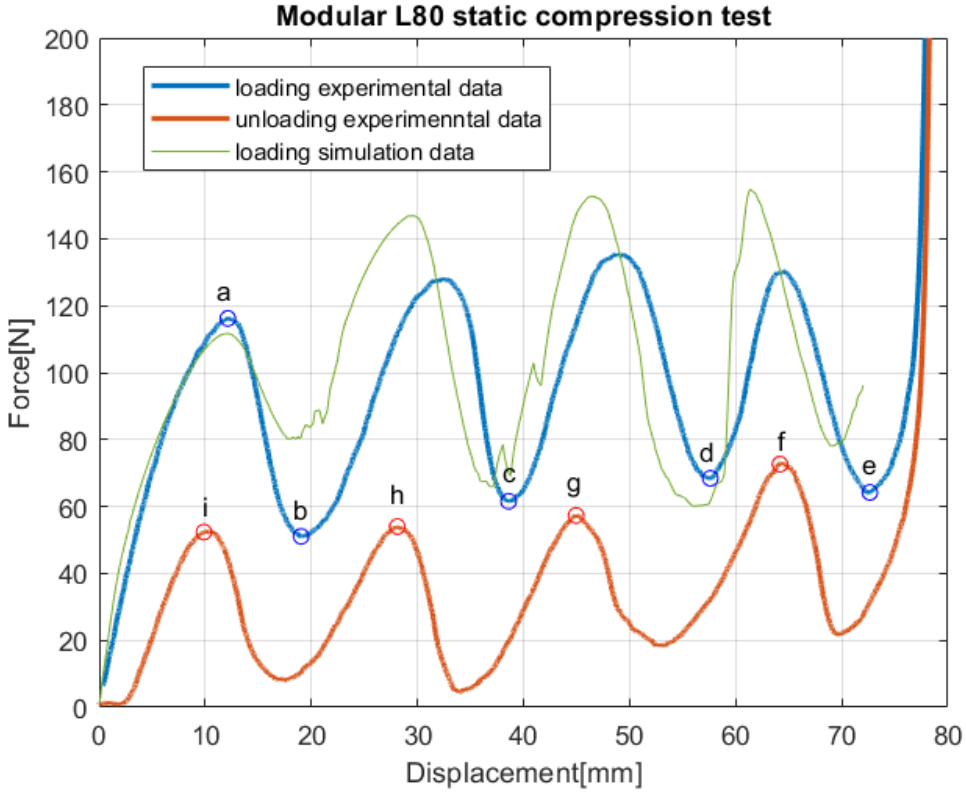

Figure 3.9: Numerical simulations and experimental data of static compression test conducted on Second iteration model

It's possible to notice clearly the presence of 4 distinct peaks in the loading curve, recording the *snap-through* events of the 4 rows of double curved beams. The reliability of the design and manufacturing is proved by the fact that all the peaks are registered at almost the same force threshold and amplitude. Moreover, the same pattern is repeated during the unloading curve occurring at similar displacement levels to the one of the loading phase.

The model showed substantial improvement in performance, summarized in tab. 3.2, given by the three-dimensional configuration, the increased bistability ratio and higher rigidity of the assembly.

Model	Peak Force [N]	Energy absorbed [J]	Energy dissipated [J]
First iteration-L55 2D	44	2.18	0.78
Second iteration-Modular L80	130	7.56	4.61
	+ 195 %	+247 %	+491 %

Table 3.2: Comparison of performance parameters of first and second iteration models

The loading curve is well approximated by numerical simulations with a maximum scatter of 15%. The first elastic part is captured perfectly by simulations, differently from the first model, where numerical simulations greatly overestimate the elastic region; this is due to the higher rigidity given by the assembly of negative stiffness honeycomb modules thanks to 3d printed inserts, bolt and nut connections, which resemble better the uniformity of mechanical properties used in the modeling.

In fig 3.14 are shown the consequent buckling events during the compression of the model. Despite the four separate negative stiffness phenomenon shown in the previous graph, at first the beams to not buckle all on the same row, as predicted by numerical simulations, but symmetrically two on the second row and two on the third row; the buckling sequence of the beam is of random nature, different for each prototype and each compression and it depends by several factors, such as the inclination of the loading and small imperfections in the single NS modules. The regularity of the behaviour is reestablished with the full compression of the first two rows of beams and the snap-through of the third row is well distributed on all 4 modules.

(a) Stage I - Compression start

(b) Stage II - First Snap-through event

(c) Stage III - Second Snap-Through event

(d) Stage IV - Third Snap-Through event

(e) Stage V - Full densification

(f) Stage VI - Firs Snap-back event

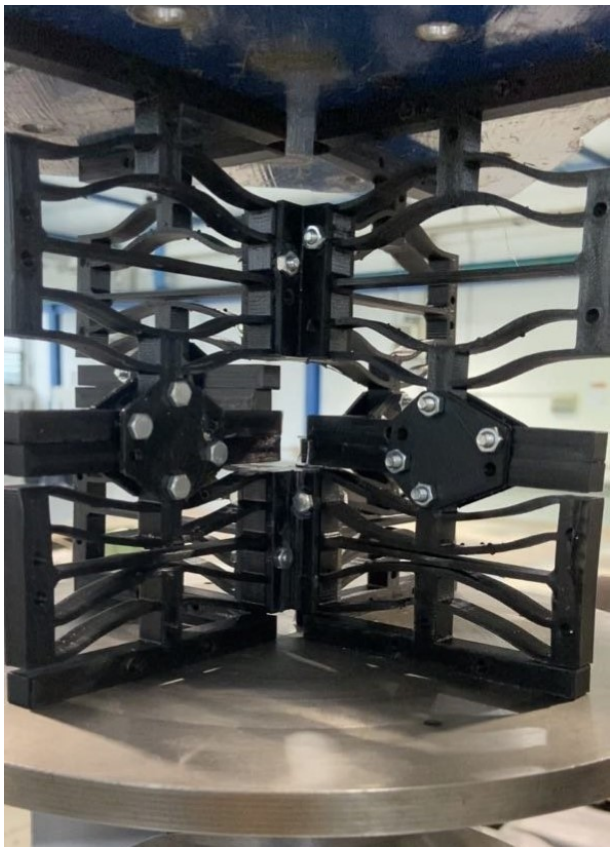

(g) Stage VII - Second Snap-back event

(h) Stage VIII - Third Snap-back event

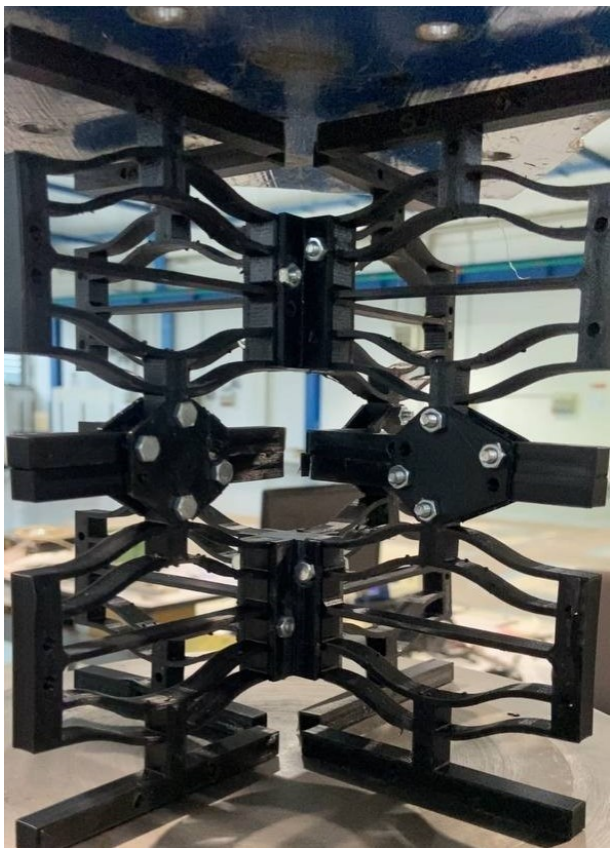

(i) Stage IX - Full recovery

Figure 3.14: Deformation stages of second model during static compression

3.2.2 Dynamic Compression

The prototype of the second model is subjected to two consecutive collisions with a mass of 32.5 kg, which is the minimum available for the testing equipment, falling the first time from 65 mm and the second one from 80 mm.

The test proved that the concept of Negative stiffness behaviour as recoverable energy absorber is effective also in dynamic compressions. The prototype was able to withstand two tests, with comparable acceleration history (as can be seen in fig. 3.15), without critical damage and recovering by itself the deformation.

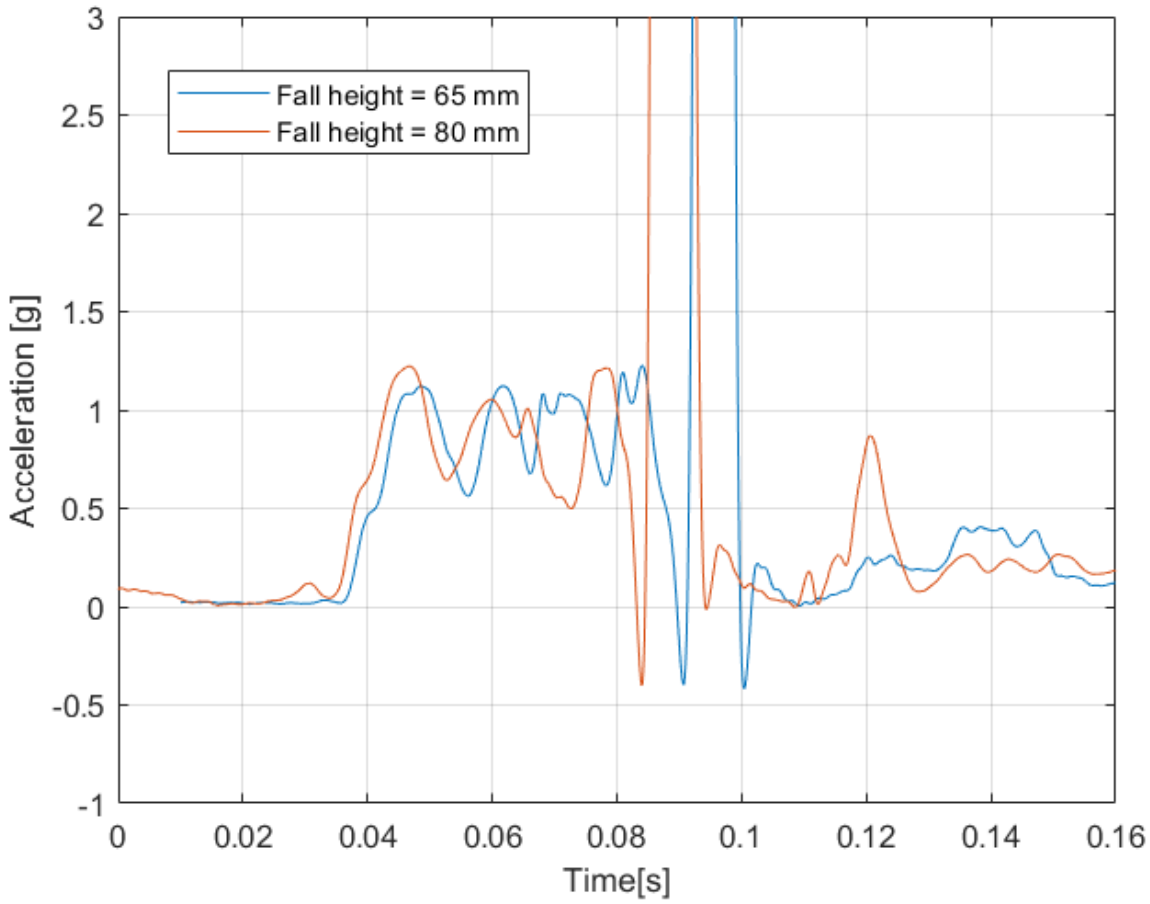

Figure 3.15: Acceleration data of dynamic compression tests conducted on Second iteration model, applied filter: SAE CF 180

In fact, in the acceleration data measured on the impacting mass, showed in fig 3.15 four peaks corresponding to the snap-through phenomena are clearly visible at an almost constant threshold of 1 g. However, the absorber is not able to absorb completely the energy of the impact with a residual peak acceleration of 43 g after full compression of the model. Moreover, increasing the range of measure of the acccelerometer is possible to see a recoil phase after the full compression peak: briefly some of the negative stiffness beam snap back and transfer the energy to the mass which bounces several times until stopping above the absorber fully compressed

In this case, the simulation data do not resemble accurately the response of the real system, with a much lower acceleration threshold registered, as visible in fig. 3.16. This discrepancy is probably due to the fact that the material data used in the simulation have been retrieved from tensile tests at low speed ($5\frac{mm}{min}$), while the loading condition of dynamic compression is faster. In fact, as already shown in the previous paragraph, the simulations on static compression tests, instead, resulted more accurate with respect to experimental data.

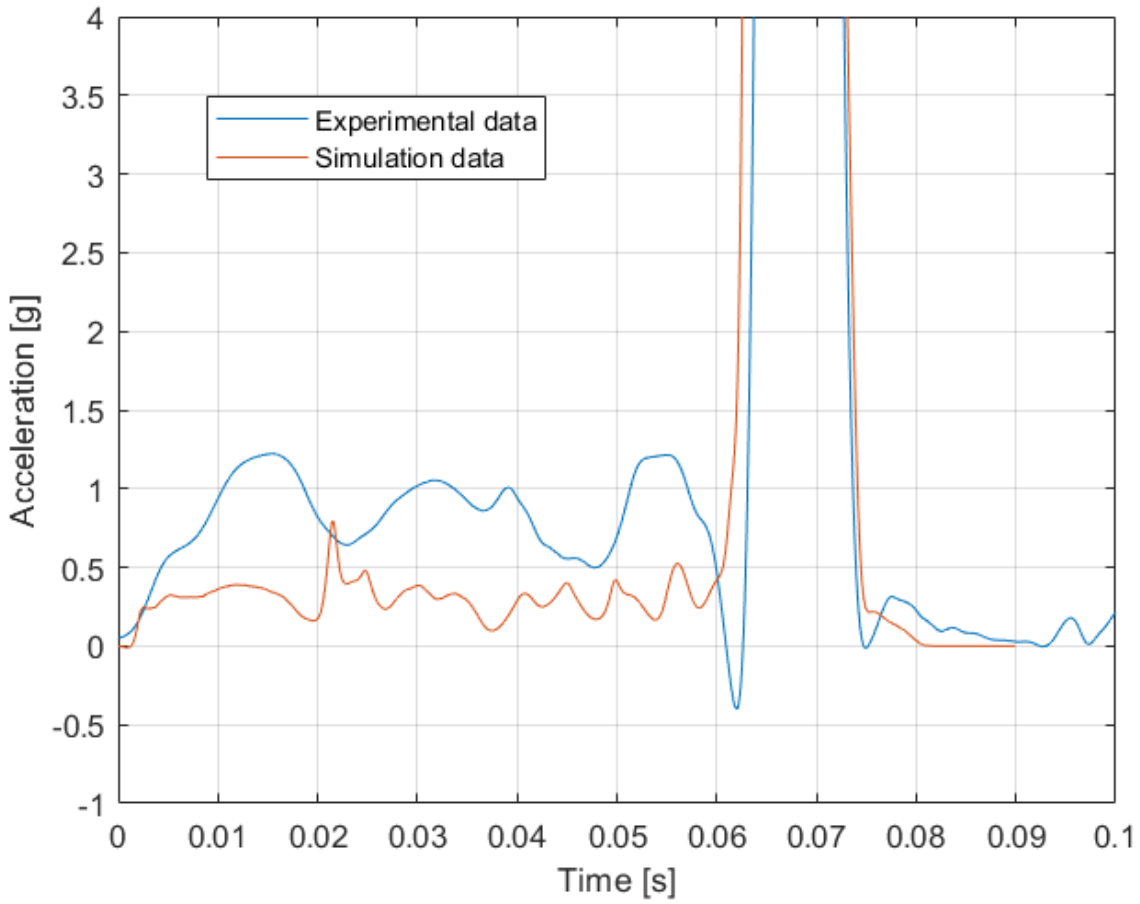

Figure 3.16: Comparison between numerical and experimental data of falling from 80 mm

However, The most interesting aspect about this test is the recovery of the deformation, which was much slower with respect to the static compression rest. As it can be seen from fig 3.22 (a-e), just after the mass is lifted after the collision the absorber is fully compressed, and in 60 seconds the deformation was fully recovered with the slow snap-back of the curved beams, one after the other.

Regarding the crashworthiness of the device, this behaviour results much more safe with respect to an immediate elastic response, because it avoid that the impacting body bouncing back could endanger the surrounding environment.

This has been achieved surely thanks to the increasing of the bistability ratio with respect to the bidimensional models of chap. 3.1, which contributes to increase the duration and the magnitude of the negative stiffness phenomena and favour a bistable behaviour

Moreover, the recovery behaviour indicates a component of viscous damping in the response of the honeycomb, which could be caused by the specific characteristics of manufacturing method and materials. In fact, it has been already observed in literature the importance of viscous effects in defining the mechanical response of polymers, due to their characteristic structure of long, covalently-bonded chains of high molecular weight atoms [33]; polymeric materials like nylon are characterized by a property called *Anelasticity*, where viscous and elastic forces are coupled, which brings to a delay in the recovery of the deformation after load is applied [35].

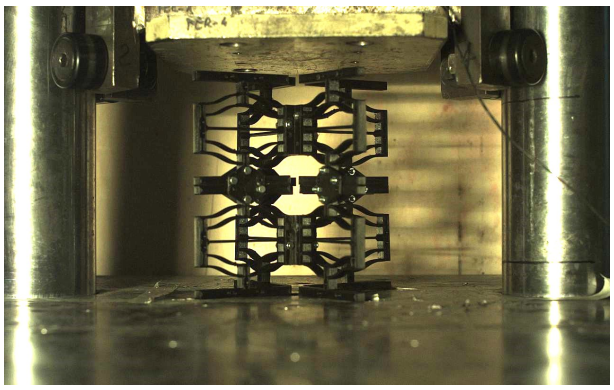

(a) Stage I - First contact with the mass, beginning of compression

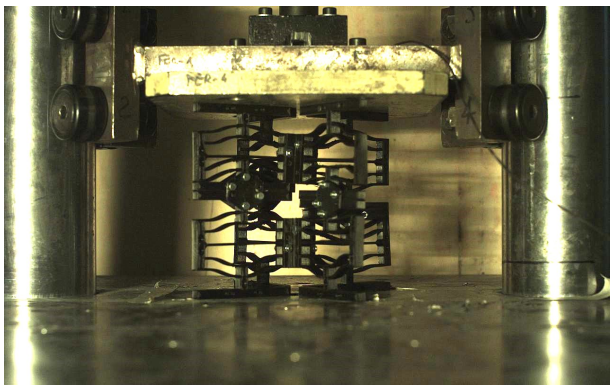

(b) Stage II - First snap-through event

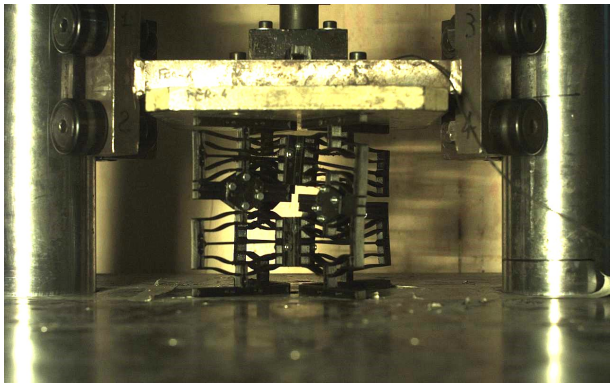

(c) Stage III - Second snap-through event

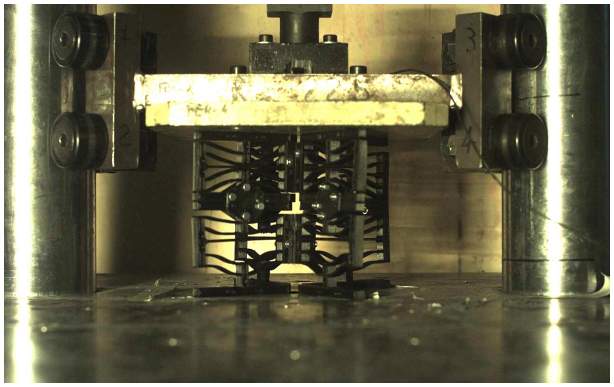

(d) Stage IV - Third snap-through event

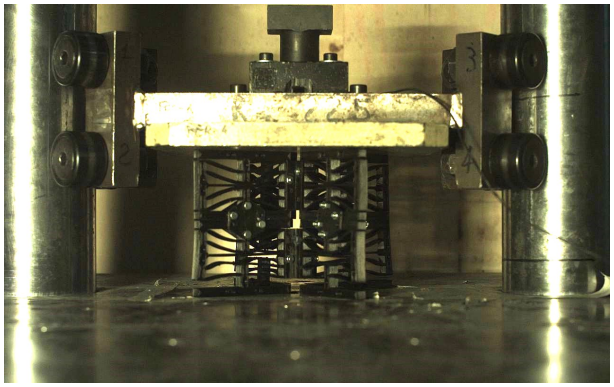

(e) Stage V - Full compression

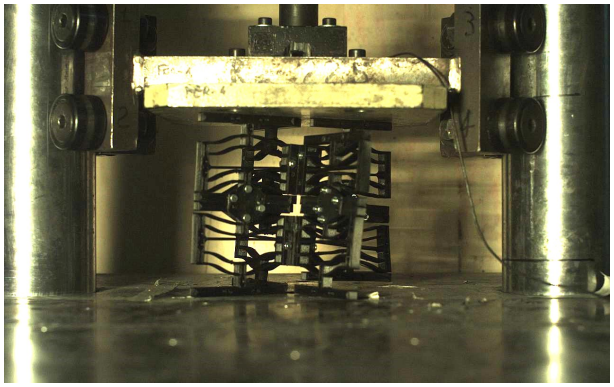

(f) Stage VI - Recoil after full compression

Figure 3.19: Deformation stages of the second model during dynamic compression

(a) Mass unloading

(b) First snap-back event , 17 seconds after mass unloading

(c) Second snap-back event, 24 seconds after mass unloading

(d) Third snap-back event, 55 seconds after mass unloading

(e) Full recovery, 60 seconds after mass unloading

Figure 3.22: Deformation stages of second model during recovery after dynamic compression

3.3 Third Iteration Model

The prototype of the third iteration model was evaluated with two dynamic compression tests with a mass of 32.5 Kg falling from 605 mm, without showing apparent sign of catastrophic failure.

In fig. 3.27 are shown the consequent buckling of the curved beams during the first dynamic compression. The four negative stiffness phenomenon are clearly distinguishable also in the acceleration plot in fig.3.23 ,the first one with an intensity of 14 g and the following at a threshold of 11 g, about 10 times greater than the data of the second iteration

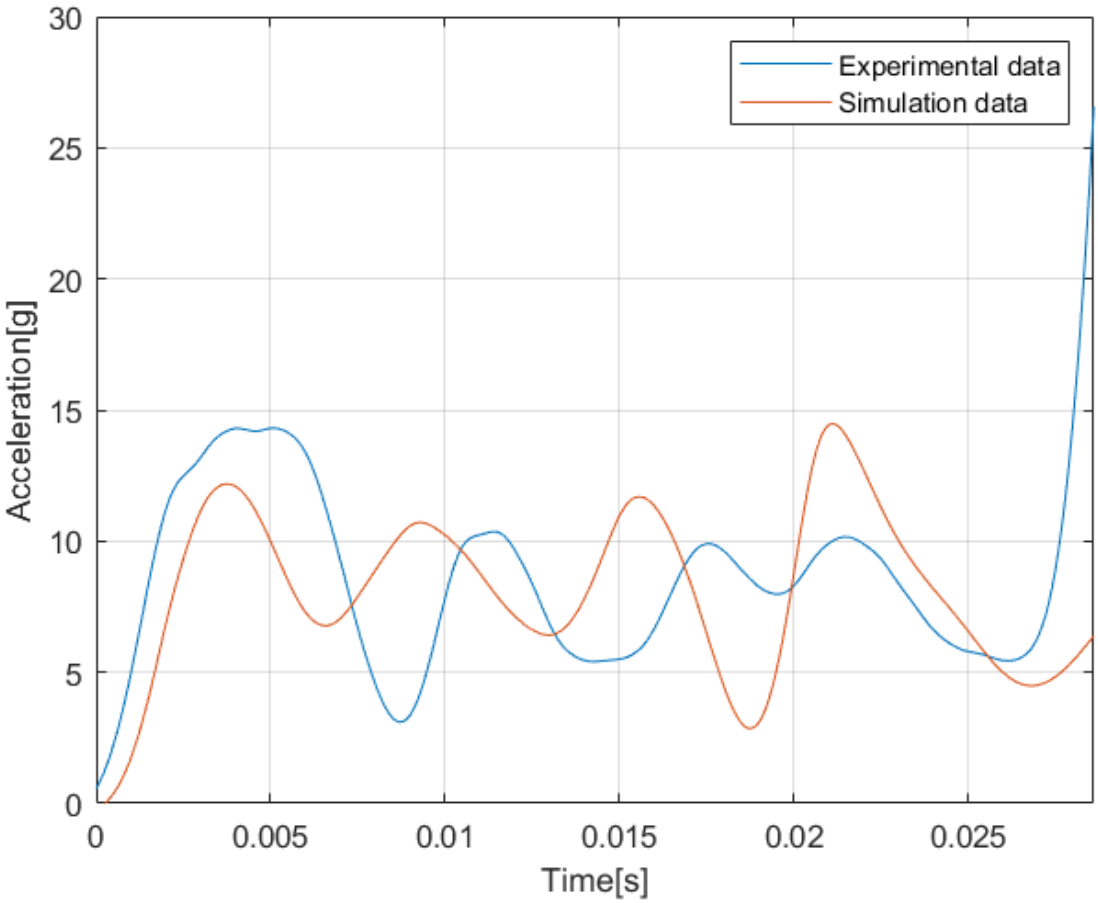

Figure 3.23: Comparison of numerical and experimental acceleration data of the first test performed on the third iteration model

The measured performance parameters during the experiment are summarized in tab. 3.3.

A substantial increase is noticed in terms of both Peak Force and amount of Energy absorbed with respect to the second iteration model, due to the choice of a more performing material.

However, unfortunately the gain in performance is not linearly proportional to the Young Modulus. The elastic modulus of Steel is 312 times larger than the one of Nylon 3D printed used for this thesis work; however, as already discussed in chap. 2.1.1 and 2.5.3 the increase of characteristic length of the cell, caused by a much lower value of yield deformation, affects negatively the Peak Force; in fact the increase of performance is only 34.6 times the value for the second iteration nylon prototype.

The value of energy absorbed is even more penalized with respect to the increased properties of the material since the height of the cells is decreased and also the stroke of the absorber.

However, the third iteration model in steel succeeded in creating a more efficient energy absorber despite the increased weight of the device, with respect to the nylon 3d printed counterpart.

Model	Material	Peak Force[N]	Energy absorbed[J]	Mass [Kg]	Specific Energy [$\frac{J}{Kg}$]
Modular L80	Nylon PA 6/66	130	7.56	0.367	43.6
Steel L130	Steel AISI 304	4500	170	2.63	64.6
		+3462%	+2149%	+617%	+ 48%

Table 3.3: Comparison of performance parameters of second and third iteration models

In fig. 3.23 is also showed the comparison with the data from numerical simulations. While in the 3D printed second iteration model, it was registered a significant difference with experimental data in dynamic compressions, due to the peculiar behaviour of the material, in this case the simulations results are quite accurate. In fact, the magnitude of the peaks associated to *snap-through* phenomena and negative stiffness (highlighted in sequence in fig. 3.27 (a-e)) is approximated with high precision: the scatter between the average value of local maximum and minimum points in experiments (8,34 g) and simulations (8,71g) is of 4 %.

The paths of the two loading curves start to diverge after the fourth local minimum, where the loading curve of the real absorber is more steeper with respect to the simulation, even though the change of slope happens at the same displacement coordinate.

It is highlighted that, as a result of the violent collision, none of the beams were fractured. In some cases the paired honeycomb modules had slightly different deformation shapes, however, as shown from slow motion video (from which pictures 3.27 (a-e) are extrapolated) differently from the 3D printed part, the *snap-through* buckling behaviours are much more regular, involving all the beams of the same layer simultaneously, showing a higher repeatability and homogeneity in the production method by laser cutting with respect to 3D printing by FDM.

As already expected in chap. 2.5.3, at the end of compression event the absorber remained in the deformed configuration. This phenomenon is mainly due to the inevitable onset of plastic deformation, due to the higher maximum deformation value ϵ_m with respect to the yield strain (ϵ_y). The numerical simulations show a maximum value of effective plastic strain of 5.9%. However, also the high bistability ratio could have favoured this phenomenon: despite having a value of Q lower than the Second iteration model, the higher stiffness and homogeneity of the metal resemble more accurately the bistable behaviour that such curved beams should have following the analytical computations of chap 2.1.1. The procedure was conducted on the same machine used for tensile tests of Nylon specimens and static compression of the first two iteration models, reported in chap. 2.4, thanks to a custom-made clamping apparatus: the four perpendicular sides of the modules were connected to thick metal plates on the top and on the base thanks to L-shaped beams, to avoid bending, while two T-shaped beam allowed to attach to the clamps of the testing machine, commonly used for tensile testing.

As can be seen in fig. 3.27 the recovery of the deformation was not symmetric, even if the four negative stiffness peaks are clearly visible in fig.3.23 ; this detail could be due to some random minor damage occurred during the compression.

All cells were successfully brought back to the initial configuration, as showed by the four negative stiffness peaks clearly visible in fig. 3.30 (a-e), which are also reported in literature by

Tan et al. [18], who performed loading-unloading static compression cycles on a steel negative stiffness honeycomb

However, the deformation was not completely recovered, with a reduction in the stroke of the absorber of 9 mm (15% of the design one). In fact, the traction was carried on until warping effects were noticed on the central horizontal beams of some cells to avoid excessive stress, probably due to the non asymmetric shape recovery reported hereinabove.

After the recovery a second dynamic compression test was performed, with the same mass falling from the same height of the first experiment. The comparison of the two experimental data is reported in fig. 3.24

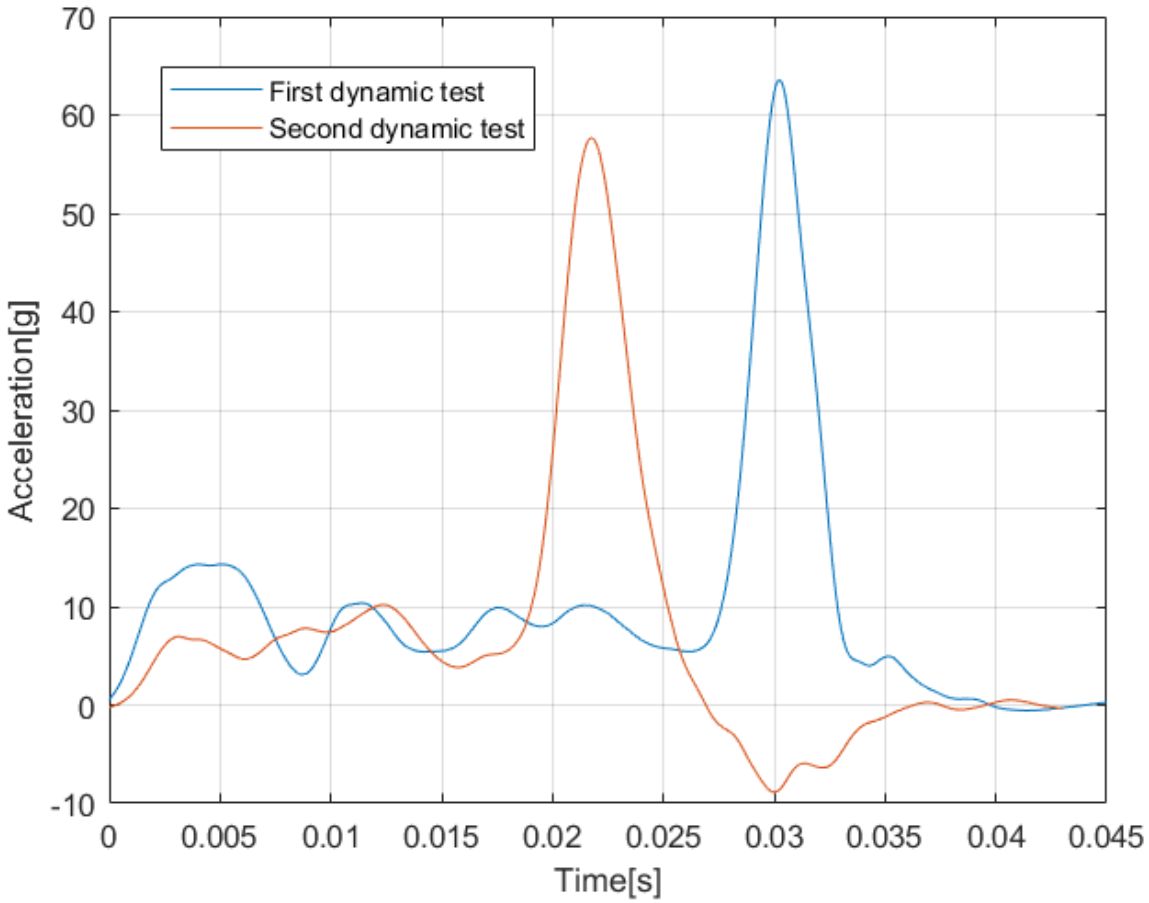

Figure 3.24: Comparison between acceleration data of the two dynamic compression test. Applied Filter: SAE CF 180

In table3.4 is observed a slight decrease in the performance of the model between the two tests, caused by the possible minor damage of some honeycomb cells and by the reduction of the stroke. However, it is highlighted in fig. 3.31 that also after the second dynamic compression test no fracture failure were noticed, showing the possibility of further reusability.

	Average Force [N]	Energy absorbed [J]
First compression test	2656	170
Second compression test	2172	126.3
	-18 %	-35 %

Table 3.4: Comparison between performance parameters of first and second dynamic compression tests performed on the same third iteration model

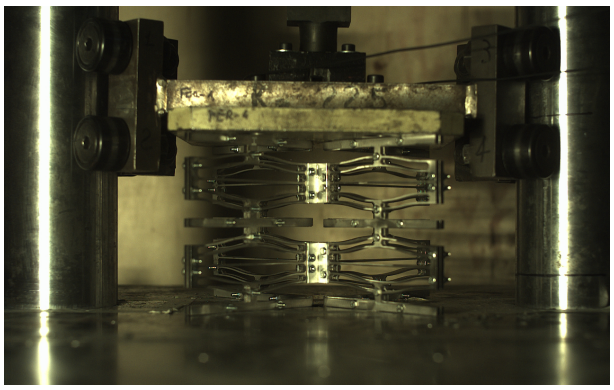

(a) Stage I - First contact with the mass, beginning of compression

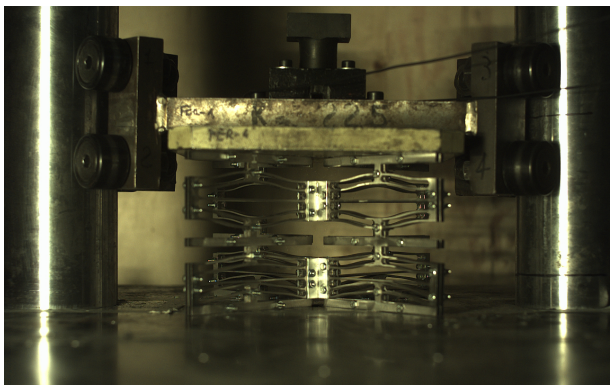

(b) Stage II - First snap-through event

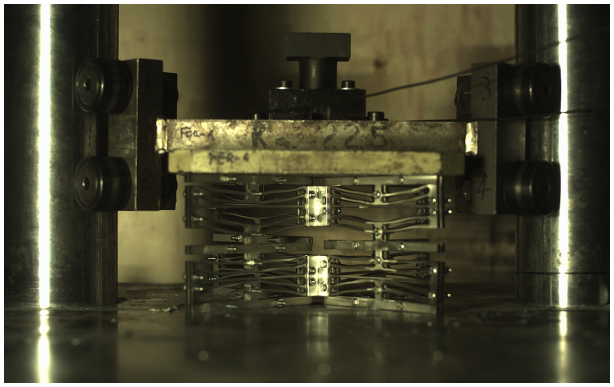

(c) Stage III - Second snap-through event

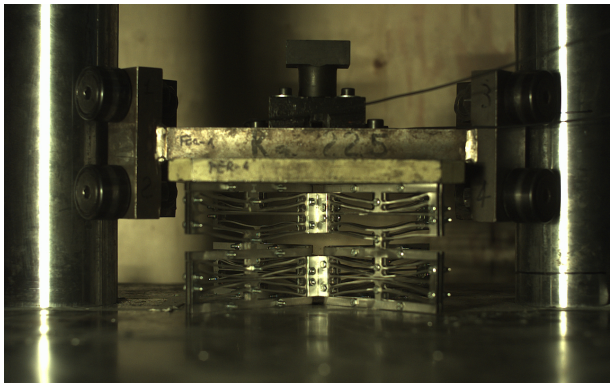

(d) Stage IV - Third snap-through event

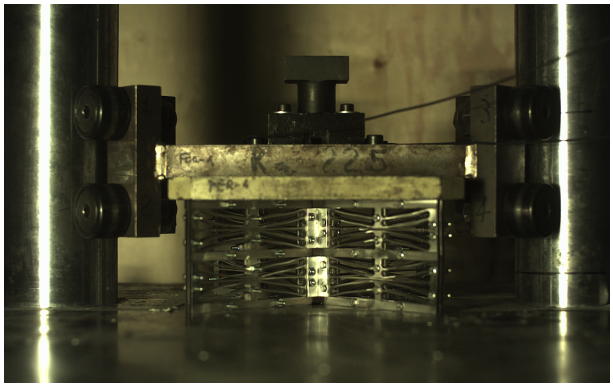

(e) Stage V - Full compression

Figure 3.27: Deformation stages of the third iteration model during dynamic compression

(a) Stage I - Initial compressed state

(b) Stage II - First snap-back event

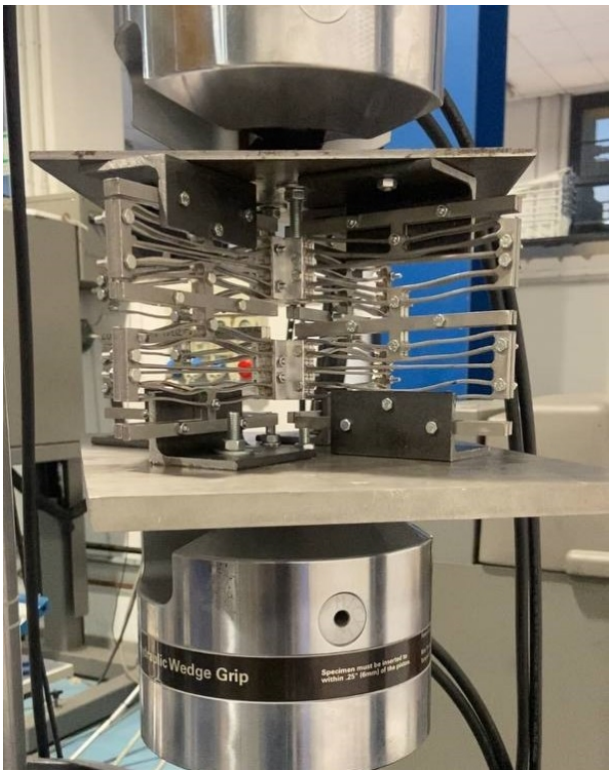

(c) Stage III - Second Snap-back event

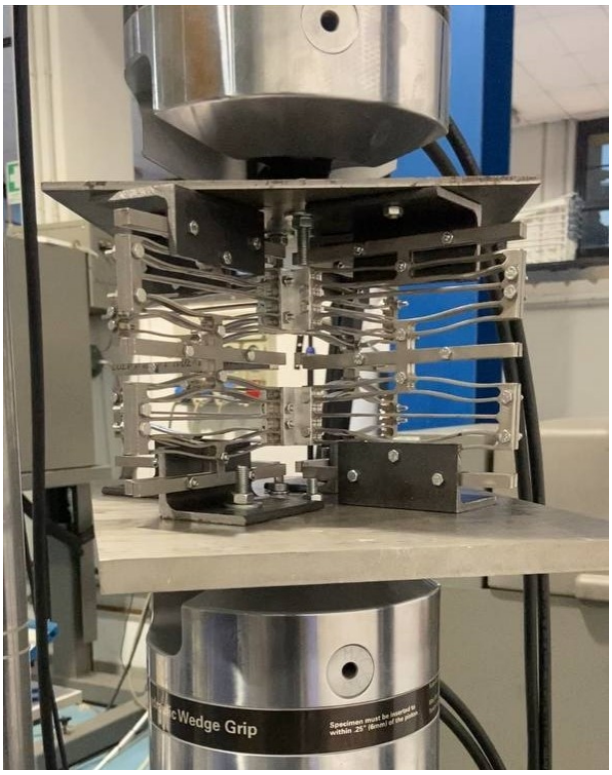

(d) Stage IV - Third Snap-back event

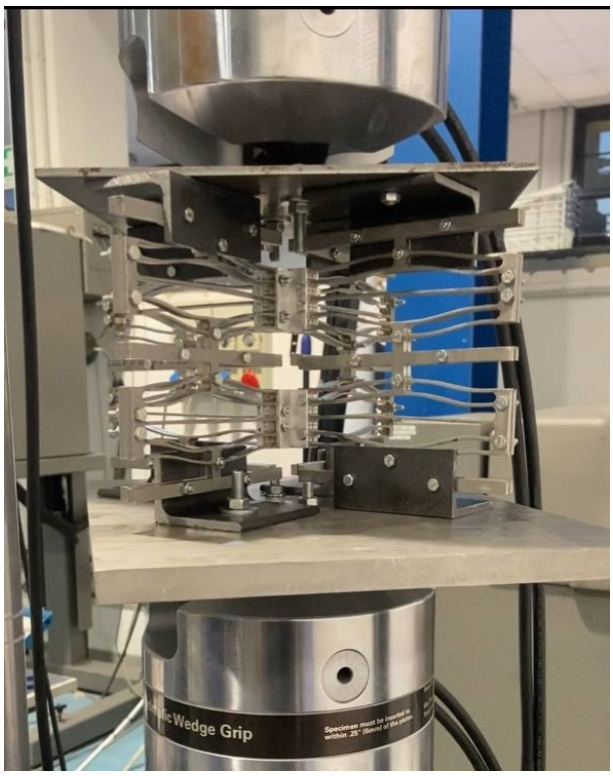

(e) Stage V - Full recovery

Figure 3.30: Deformation stages during traction-assisted recovery after the first compression event

Figure 3.31: Third iteration model after the second dynamic compression test

Chapter 4

Discussion

This thesis work satisfies the aim of the study, stated in chap 1.5, in creating an effective and functional reusable crash absorber exploiting the concept of Negative Stiffness Honeycomb.

In fact, the second and third iteration models showed a reliable behaviour during compression and were tested successfully in a dynamic collision environment, with a controlled recovery of the deformation (in the Nylon 3D printed case autonomously, while in the steel case it was assisted) which contributes to increasing the safety of the device in crash events.

Moreover, the modular feature makes the manufacturing and assembly easy and immediate, with the potentiality to increase performance adding more and more modules in series or in parallel.

The mechanical response observed during the static compression test of the second iteration model, reported in fig. 3.9 showed an oscillatory behaviour both in the loading and unloading phase, at almost constant force threshold, very similar to previous literature studies conducted by *Debau et al.* [9] and *Correa et al.* [22], also reported in the document in fig. 1.14.Moreover it was proved that the intensity of this negative stiffness behaviour was due to the increase bistability ratio, as stated by *Correa et al.* [22] and *Ren et al.* [36].

The resemblance with the work of *Debau et al.* is particularly important because it was one of the first and few researches that tested Negative Stiffness honeycomb in dynamic crashes and inspired the aim of this thesis work. With respect to the design proposed in that paper, showed also in Introduction in fig. 1.15, the main differences of the prototype presented in this thesis work, was the three dimensional layout. This change constitutes an improvement in the reliability and functionality of the absorber, since it avoids the occurrence of out-of-plane instability caused by the small transversal width of the specimen, registered also by the First iteration model, visible in fig. 2.26.

The small thickness of Negative stiffness honeycomb cells was limited by manufacturing constraints both for the prototype in Additive manufacturing and in metal. In fact, as already explained, Nylon 3D printed parts by FDM suffer from warping caused by the generation of internal stresses during printing, and the phenomenon is affected by printing time and thickness of the specimen, while the laser cutting in metals generates excessive level of heat during the manufacturing of thicker parts, with the possibility of having unacceptable defects.

Debau et al. decided to solve the problem using more powerful, but also expensive, manufacturing technologies like additive manufacturing with SLS (Selective Laser Sintering) or Waterjet cutting 1.14. Instead, we thought that the option to interlock bidimensional modules in a three-dimensional design was an efficient and effective way to obtain a more stable design. The idea was inspired by the work of *Tan et al.* [18], with one key improvement : instead of being held together by a brazing process, the metal Negative Stiffness honeycomb modules were

assembled using central cross inserts with bolt and nut connections, making much easier and affordable the assembling, and without further altering thermically the properties of the metal in such critical spots for the energy absorbing mechanism.

Furthermore, the metal prototype was tested also in dynamic crash event, reaching the highest level of Peak force and Energy absorption among Negative stiffness honeycomb crash absorbing devices previously researched in literature, summarized for comparison in table 4.1 (where NSH is used as abbreviation of Negative Stiffness Honeycomb). The increase in absolute performance using high performance material goes to the expense of an increase in mass of the absorber, passing from 0.367 Kg of the Nylon Second Iteration Model prototype to 2.63 Kg of the Steel Third Iteration Model. As a result the specific energy of the absorbers is overcome by the work of *Chen et al.* [37], who recently used T-800 carbon fiber as base material, exploiting its low thickness of the lamina and low density; however, both their Peak Force and Energy absorbed are significantly lower with respect to the prototypes experimented in this thesis work due to the use of parallel and series configuration of multiple Negative Stiffness Honeycomb cells. Moreover, even if carbon fiber is a promising material for its properties, its low range of deformation could cause delaminations and fractures in this type of applications, as already noticed by the same authors in some specimens even during the first compression event.

Published models	Peak Force [N]	Energy absorbed[J]	Specific Energy[$\frac{J}{Kg}$]	Test performed
Gradient NSH [38]	20 to 100	1.9	20.26	Static compression
Carbon fiber reinforced NS metamaterial [37]	320	5.62	690	Static and Dynamic compression
Bidimensional NSH in Nylon by SLS [9]	208	4.88	[Not reported]	Static and Dynamic compression
Bidimensional NSH in Aluminum by waterjet [9]	434	4.4	[Not reported]	Static and Dynamic compression
Lattice multi-stable meta structures [39]	45	4	[Not reported]	Static and Dynamic compression
Inelastic instability NS [18]	900 to 1200	28.8	[Not reported]	Static compression
Modular L80	130	7.56	43.6	Static and Dynamic compression
Steel L130	4500	170	64.6	Dynamic compression

Table 4.1: Comparison between Negative Stiffness Honeycomb performance parameters in literature

One limitation of the three-dimensional modular design is the low specific energy per unit of volume. In fact, while the energy absorption is proportional to the transversal depth of Negative Stiffness Honeycomb plates, the volume occupied by the prototypes is determined by the length of the cells, which is a significantly higher dimension. However, the solution creates a much lighter absorber compared a bidimensional honeycomb of the same size.

One of the most interesting results observed in our experiments was the slow recovery of deformation of the Nylon 3D printed second iteration model after unloading in dynamic compression test. This behaviour has not been reported by any other author regarding negative stiffness honeycomb absorbers during crash, which either remain fully compressed after the collision, exhibiting a truly bistable behaviour, and need an opposite traction force to reestablish the original shape, like in the work of *Zhang et al.* [39], or recover instantly the initial configuration upon release of impact load, as experimented by *Debau et al.*. The result was

achieved thanks to a combination of material effect, which shows peculiar visco-elastic properties, and an high value of bistability ratio, which allows for a more pronounced negative stiffness behaviour.

Unfortunately, the numerical simulations were not able to capture this behaviour and, in general, also in static compression, were not accurate on Force measures in the unloading phase, due to the highly non linear nature of the material response under cyclic loading, as pointed out by *Appelsved et al.* [32].

An other limitation of this thesis work is the lack of repeatability studies on the prototypes by testing more copies of the same model to investigate the dispersion of the data.

4.1 Further Developments

This thesis work has proven successfully the potentiality of Negative Stiffness honeycomb as reusable crash absorbing devices. However, the following further developments could increase even more the performance and functionality of this technology:

- The design phase could be further explored with the possibility of performing structural optimizations with FEM simulations on negative stiffness honeycomb of different characteristic dimensions, to overcome the limits that analytical formulas of *Qiu et al.* [20] showed in approximating the behaviour of curved beams with the one of the entire cell, as explained in 2.2.1, and also revealed by the results of the second itertion model

- The process of recovery of deformation, in the case of absorbers exploiting elasto-plastic deformation, could be automatized by the use of hydraulic actuators placed at the four empty corners of the absorber.

- The empty space not exploited in three-dimensional interlocking configuration could also be replaced with conventional absorbers like metal tubes, creating an hybrid crash absorber with higher performance, and the possibility of partially recovering the functionality with the Negative stiffness honeycomb element.

- Finally, as suggested by previous literature studies [40], the Negative Stiffness honeycomb could be used at the microscopic level to create a lattice structure with enhanced energy-absorbing and shape-recovery properties

Chapter 5

Conclusions

In conclusion, this thesis work provided evidence for the potential use of Negative Stiffness Honeycomb as an effective reusable crash absorber.

From the original concept the functionality of the device in dynamic crash tests was improved with a modular three-dimensional configuration, made in Nylon 3D printed by FDM and in Laser-cut Steel, which led to a more powerful and safe crash absorber, with simpler and cheaper manufacturing and assembly process.

If confirmed in further larger studies, this thesis work could represent a relevant advancement in the field of crashworthiness. In fact, negative stiffness honeycomb could become a viable alternative in those contexts where conventional crash absorbers are not convenient for practical applications involving repeated impacts or when substitution of the device is made complex by environmental and economic factors, with the final result of reducing cost, time and work associated to the replacement of the deformed safety device after the collision.

Chapter 6

Appendix

6.1 Appendix A - Material properties used in simulations

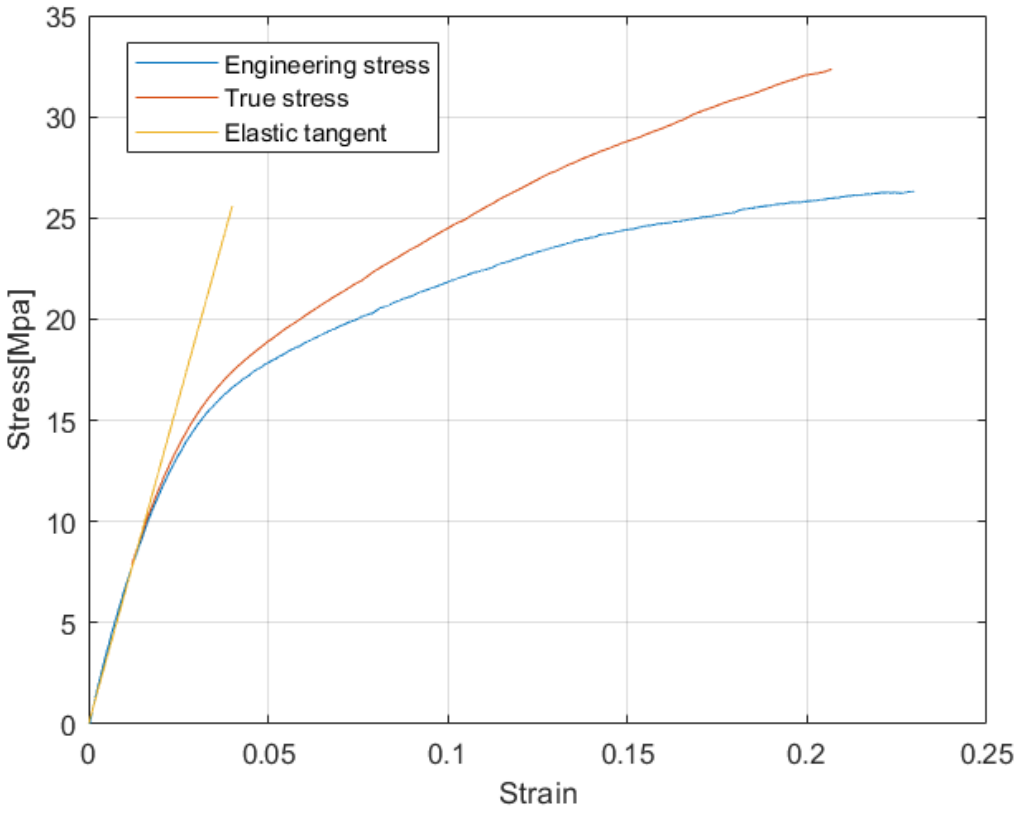

Figure 6.1: Force-displacement curve of Novamid ID1030 by FDM during tensile tests

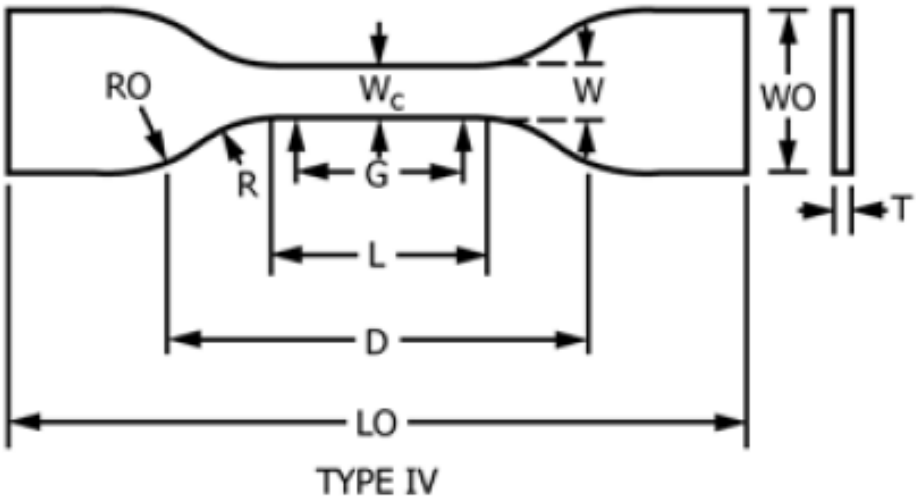

Figure 6.2: Tensile test specimen following regulation ASTM D638-14 standard type IV [28]

W - Width of narrow section [mm]	6
L - Length of narrow section [mm]	33
WO - Width overall, min. [mm]	19
LO - Length Overall, min [mm]	115
G - Gage length [mm]	25
D - Distance between grips[mm]	65
R - Radius of fillet [mm]	14
RO - Outer Radius [mm]	25
T - Thickness, max [mm]	4

Table 6.1: Measures of dogbone specimens used in the tensile tests on 3D printed materials, referred to dimensions in fig. 6.2 [28]

6.2 Appendix B - 3D Printing parameters

Printing parameter	setup
Layer Height [mm]	0.2
Initial Layer Height [mm]	0.3
Line width [mm]	0.4
Wall line count	5
Z seam alignment	Random
Top layers	10
Bottom layers	10
Infill density [%]	30
Infill pattern	lines
Printing temperature [$°C$]	270
Build plate temperature [$°C$]	85
Print speed [$\frac{mm}{s}$]	50
Infill speed [$\frac{mm}{s}$]	60
Retraction distance [mm]	8
Retraction speed [$\frac{mm}{s}$]	25
Fan speed [%]	0

Table 6.2: Summary of printing parameters used in the production of prototypes by 3D printing

Bibliography and References

[1] World Health Organization. *Road Traffic Injuries*. 2022. URL: https://www.who.int/news-room/fact-sheets/detail/road-traffic-injuries.

[2] *John Paul Stapp*. URL: https://en.wikipedia.org/wiki/John_Stapp.

[3] *Aircraft crash survival design guide*. Simula INC, 1980.

[4] Dennis F. Shanahan. "Human tolerance and crash survivability". In: *RTO HFM Lecture Series on "Pathological Aspects and Associated Biodynamics in Aircraft Accident Investigation"* (2004).

[5] Jorge A. C. Ambrosio. *Crashworthiness: Energy Management and Occupant Protection*. Springer Wien New York, 2001.

[6] Wlodzimierz Abramowicz. "Dynamic axial crushing of cyrcular tubes". In: *International Journal of Impact Engineering* (1984).

[7] A. pugsley. "The crumpling of tubular structures under impact conditions". In: *Symposium of the use of Aluminium in Railway Rolling Stock* (1960).

[8] Marco Anghileri. *Passive Safety Notes for Engineering students*. 2020.

[9] David A. Debau. "Impact behavior of negative stiffness honeycomb materials". In: *Journal of Materials Research* (2017).

[10] Lorna J. Gibson. *Cellular solids*. Cambridge Solid State Science Series, 1997, p. 94.

[11] Carolyn C. Seepersad. "Mechanical design of negative stiffness honeycomb materials". In: *Integrating materials and manufacturing innovation* (2015).

[12] Althea M. Hayes. *Mechanics of Linear cellular alloys*. Mech Mater, 2004.

[13] Tomasz Wierzbicki. "Crushing analysis of metal honeycombs". In: *International Journal of Impact Engineering* (1983).

[14] Stelios Kyriakides Scoott D. Papka. "In-plane compressive response and crushing of honeycomb". In: *Journal of the Mechanics and Physics of Solids* (1994).

[15] M. Bodaghi. "Reversible energy absorbing meta-sandwiches by FDM 4D printing". In: *International journal of Mechanical Sciences* (2020).

[16] Seoyoung Heo. "Weakening-induced snap instability as a novel reusable force protection mechanism". In: *International journal of mechanical sciences* (2021).

[17] Carolyn Conner Seepersad. "Negative Stiffness Honeycomb Material". In: *United States Patent Application Pubblication* (2016).

[18] Xiaojun Tan. "Reusable metamaterial via inelastic instability for energy absorption". In: *International journal of mechanical sciences* (2018).

[19] Navid Mehreganian. "Structural Mechanics of negative stiffness honeycomb metamaterials". In: *Journal of Applied Mechanics* (2021).

[20] Jin Qiu. "A Curved-Beam Bistable Mechanism". In: *Journal of Microelectromechanical systems* (2004).

[21] Timothy D. Klatt. "Selective laser sintering of Negative stiffness mesostructures for recoverable, nearly-ideal shock isolation". In: *ResearchGate* (2013).

[22] Dixon M. Correa. "Negative stiffness honeycombs for recoverable shock isolation". In: *Rapid prototyping journal* (2015).

[23] Crisfield M. A. *Non-Linear Finite Element Analysis of Solids and Structures*. John Wiley Sons, 2000, p. 138.

[24] John O. Hallquist. *LS-Dyna theory manual*. 2006.

[25] Ted Belytschko. "Hourglass control in linear and nonlinear problems". In: *Computer methods in applied mechanics and engineering* (1984).

[26] Bridget O'Neal. *FDM 3D Printing: Effects of Typical Parameters on Functional Parts*. 2020. URL: https://3dprint.com/267642/fdm-3d-printing-effects-of-typical-parameters-on-functional-parts/.

[27] Ahmed Elkaseer. *Experiment-based process modeling and optimization for high-quality and resource-efficient FFF 3D printing*. 2020.

[28] ASTM international. "Designation D38-14: Standard test method for tensile property of plastics". In: (2015).

[29] Martina Scapin. "Numerical Simulations of components produced bu Fused deposition 3d printing". In: *materials* (2021).

[30] Miroslav Radovanovic. "Experimental Investigations Of CO2 Laser Cut Quality: A Review". In: *Nonconventional technologies review* (2011).

[31] www.difference.minaprem.com. *Difference Between Weld Metal and Heat Affected Zone (HAZ)*. 2022. URL: http://www.difference.minaprem.com/joining/difference-between-weld-metal-and-heat-affected-zone-haz/.

[32] Peter Appelsved. "Investigation of Mechanical Properties of Thermoplastics with implementations of LS-Dyna Materials Models". In: *Degree project in Solid Mechanics, KTH engineering sciences* (2012).

[33] Serban Dan-Andrei. "Viscelastic and viscoplastic materials, Chapter 9: Viscoplastic behaviour of polyamides". In: (2016).

[34] Fazeel Khan. "Loading History effects on the Creep and Relaxation behaviour of thermoplastics". In: *Journals of Engineering Materials and Technology* (2006).

[35] Gert Strobl. *The physics of polymers: Concepts for understanding their structures and behaviour*. Springer, 2007.

[36] Chenhui Ren. "Mechanical performance of multidirectional buckling-based negative stiffness metamaterials: an analytical and numerical study". In: *Materials* (2018), p. 5.

[37] Shuai Chen. "Contionuous carbon fiber reinforced composite negative stiffness mechanical metamaterial for recoverable energy absorption". In: *Composite Structures* (2022).

[38] Shuai Chen. "A novel gradient negative stiffness honeycomb for recoverable energy absorption". In: *Composites* (2021).

[39] Yong Zhang. "A Novel Design of Multi-stable Metastructures for Energy Dissipation". In: *Materials Design* (2021).

[40] Tobias Frenzel. "Tailored Buckling Microlattices as Reusable Light-Weight Shock Absorbers". In: *Advanced materials* (2016).